Charles University

Faculty of Mathematics and Physics

DOCTORAL THESIS

2020 **Pavel Pleskunov**

FACULTY
OF MATHEMATICS
AND PHYSICS
Charles University

DOCTORAL THESIS

MSc. Pavel Pleskunov

Multicomponent plasma polymers with spatially controlled properties

Department of Macromolecular Physics

Supervisor of the doctoral thesis: Prof. Ing. Andrey Shukurov, PhD

Study programme: Physics
Specialization: F4 – Biophysics, Chemical and Macromolecular Physics

Prague 2020

I declare that I carried out this doctoral thesis independently, and only with the cited sources, literature and other professional sources.

I understand that my work relates to the rights and obligations under the Act No. 121/2000 Coll., the Copyright Act, as amended, in particular the fact that the Charles University has the right to conclude a license agreement on the use of this work as a school work pursuant to Section 60 paragraph 1 of the Copyright Act.

In …… date ……. signature

Acknowledgements

First of all, I would like to express my sincere appreciation to my supervisor and mentor, Prof. Andrey Shukurov, who inspired and convincingly guided me by sharing fascinating scientific ideas and invaluable practical advice. Without the knowledge and the skills he has imparted to me, completion of the current work would not have been possible. I am deeply indebted to him for his friendship and support during the past years as well.

I am very grateful to all the members of the Department of Macromolecular Physics: Prof. Hynek Biederman, the head of the Group of Plasma Polymers, and Assoc. Prof. Danka Slavínská for sharing their knowledge in fruitful discussions; Assoc. Prof. Ondřej Kylián, the head of the Department, for the assistance with measurements and useful advice on many other aspects of experimental work; Dr. Jan Hanuš, Dr. Jaroslav Kousal, Dr. Pavel Solař and Dr. Anna Kuzminova for their help with experimental activities, lab duties and excellent working atmosphere. For the help in the acquirement of the technical expertise and skillset, I would like to thank Dr. Ivan Gordeev from the Institute of Physics, Academy of Sciences of the Czech Republic and Dr. Artem Shelemin from the University of Montreal with whom I had the great pleasure to work with. I also wish to thank Assoc. Prof. Ivan Krakovský for assistance with GPC measurements.

I also wish to thank my colleagues and good friends Dr. Daniil Nikitin, Dr. Mykhailo Vaidulych, Ing. Suren Ali-Ogly, MSc. Momme Thomsen, MSc. Tereza Košutová, MSc. Zdeněk Krtouš, MSc. Radka Štefaníková, MSc. Hana Libenská, MSc. Natalya Khomiakova and MSc. Renata Tafiichuk for positive feedback, willingness to help and inexhaustible enthusiasm which made up such pleasant working hours.

I would also like to extend my gratitude to Dr. Ivan Khalakhan and Dr. Peter Kuš from the Department of Surface and Plasma Science, Charles University for assistance with FC-AFM and SEM measurements.

I would like to thank Assoc. Prof. Zdeňka Kolská from the J. E. Purkyne University in the Czech Republic for zeta-potential measurements.

I very much appreciate Prof. Andreas Schonhals and MSc. Marcel Gawek from Bundesanstalt fur Materialforschung und – prüfung in Berlin for the organization and taking care of SHS measurements.

I would like to recognize the effort that I received from Prof. Harumi Sato, Chihiro Funaki, Tatsuro Nasu and Tomoki Nagahama from Graduate School of Human Development and Environment, Kobe University. I am thankful for their willingness to carry out the THz-Raman measurements.

Many thanks to Dr. Miriam Unger and Dr. Anirban Roy from Bruker Nano Surfaces Division, Santa Barbara, USA for the assistance with AFM-IR measurements.

Especially helpful to me during writing the thesis was Ing. Joery Korobejnik, BSc from Xensor Integration BV who provided glorious optical microscope images of the integrated chips for SHS and the license to use them. Without this contribution, the work would not be so complete.

I wish to acknowledge the support and profound beliefs in my abilities from my parents. Moreover, I am extremely grateful to my charming wife Ksenia who always stayed beside and provided me with encouragement, patience and love that kept me going. She also contributed to this work by sharing her insights and extensive experience in graphical design and by performing 3D modelling. Last, but not least, I am thankful to my old mates: Victoria, who played a decisive role in my personal choices and beliefs when the road was tough, and Sergey for the countless wise advice and constructive criticism.

Title: Multicomponent plasma polymers with spatially controlled properties

Author: MSc. Pavel Pleskunov

Department / Institute: Department of Macromolecular Physics/Charles University

Supervisor of the doctoral thesis: Prof. Ing. Andrey Shukurov, PhD, Department of Macromolecular Physics / Charles University

Abstract: Mixing of two (or more) polymers often leads to phase separation and to the formation of nanoscale architecture, which can be highly attractive in various applications including controllable drug delivery, fabrication of separation and solid electrolyte membranes, gas storage, etc. Different wet-chemistry techniques already exist to produce nanophase-separated polymers; however, capturing the resultant polymeric structure in a predictable manner remains a challenging task. In this thesis, a low-temperature plasma-based strategy is investigated for the production of multicomponent thin films of plasma polymers with spatially discriminated nanoscale domains. Gas aggregation cluster source is used for the fabrication of nanoparticles of plasma polymerized acrylic acid, whereas Plasma-Assisted Vapor Phase Deposition is used for the deposition of thin films of poly(ethylene oxide) plasma polymer. Embedding of nanoparticles into matrices of thermodynamically incompatible plasma polymer as well as sequential deposition of two immiscible plasma polymers are also studied. Parameters of deposition are investigated to ensure the phase separation at the nanoscale. Fundamental mechanisms of the nanopattern formation are highlighted. The relationship between nano architecture and functionality (chemical composition, crosslink density, shape, and size distribution of nanodomains, swelling phenomena, selective adsorption of biomolecules) is analyzed.

Keywords: plasma polymerization, nanophase separation, plasma polymer nanoparticles, gas aggregation cluster source, nanostructure, glassy dynamics, functionalization, spatially-controlled biomolecule attachment

Název práce: Multikomponentní plazmové polymery s prostorově řízenými vlastnostmi

Author: Mgr. Pavel Pleskunov

Katedra/Ústav: Katedra Makromolekulární Fyziky/Univerzita Karlova

Vedoucí doktorské práce: Prof. Ing. Andrey Shukurov, PhD

Abstrakt: Směšování dvou či více polymerů často vede k jejich fázové separaci a ke vzniku nanostruktur, které jsou atraktivní pro využití v různých aplikacích včetně řízeného podávání léčiv, přípravy separačních membrán, membrán s pevným elektrolytem, skladování plynů atd. Ačkoliv již byly vyvinuty nejrůznější metody přípravy nanofázově separovaných polymerů, které jsou založeny na "mokré" chemii, řízení a předpověditelné ovlivňování jejich finální struktury doposud představuje obtížný vědecký problém. V předkládané disertační práci je zkoumána možnost přípravy vícesložkových tenkých vrstev plazmových polymerů s prostorově odlišitelnými nanodoménami pomocí metod založených na využití nízkoteplotního plazmatu. Nanočástice plazmových polymerů jsou připravovány pomocí plynových agregačních zdrojů, zatímco matrice plazmových polymerů (plazmově polymerizovaný polyetylénoxid) jsou nanášeny v podobě tenkých vrstev pomocí plazmatem podporované depozici z plynné fáze. Je zkoumáno zabudovávání nanočástic do termodynamicky nekompatibilního plazmového polymeru i ko-depozice dvou nemísitelných plazmových polymerů. Depoziční parametry jsou studovány především s ohledem na vznik fázové separace na nanoúrovni a pochopení tohoto jevu. Je studován vztah mezi nanoarchitekturou připravovaných vrstev a jejich funkčními vlastnostmi (chemické složení, stupeň zasíťování, tvar a distribuce nanodomén, bobtnací jevy).

Klíčová slova: polymerizace v plazmatu, nanofázova separace, nanočástice plazmových polymerů, plynový agregační zdroj nanočástic, nanostruktura, segmentová dynamika, funkcionalizace, prostorově řízené vázání biomolekul

Contents

Aims of the Doctoral Thesis

The thesis is primarily focused on the development of the advanced plasma-based methods, engineering of novel nano-structured and multicomponent plasma polymers, and the study of the mechanisms of their self-structuring, including changes in chemical and physical properties, interfacial phenomena, swelling behavior and bio-interaction. For the successful realization of this aim, the following objectives have been devised:

1. The synthesis and characterization of carboxyl-functionalized plasma polymer nanoparticles with tailor-made architecture and chemical composition by gas aggregation. The study of the mechanisms responsible for nanoparticle formation and growth.
2. The development of the approach to the synthesis of multicomponent and nanophase-separated thin films of plasma polymers by combining the gas aggregation spatially decoupled from the plasma-assisted vapor phase deposition technique and following characterization of the resulting materials, including testing against the spatially-resolved biomolecule attachment.
3. The investigation of the impact of plasma polymer spatial confinement and segmental dynamics on the resulting thin film morphologies and nano-architectures.

1. Introduction

Preface

The International Union of Pure and Applied Chemistry (IUPAC) defines the term "polymer" as "a substance composed of macromolecules" where the "macromolecule" refers to "a molecule of high relative molecular mass, the structure of which essentially comprises the multiple repetition of units derived, actually or conceptually, from molecules of low relative molecular mass" according to the standards developing organization headquartered in Research Triangle Park, North Carolina, USA [1].

So what polymers exactly are? Generally, polymers are large molecules consisting of several repeating molecules of smaller size bound together. Typically, the number of these repetitive structural units in polymer falls into 10^2-10^4. There are two types of polymers: the ones that occur naturally, such as rubber, polysaccharides (i.e., cellulose), proteins and nucleic acids, and the man-made entities among which the most common ones include polyethylene (PE), polypropylene (PP), nylon and polytetrafluoroethylene (Teflon^{TM}).

Although the polymer usage in miscellaneous applications is as old as mankind, the history of polymer science dates back to the 1920s. More specifically, its beginning points to a series of key findings: a concept of long-chain molecules consisting of atoms covalently linked one to another, conclusively proven by Staudinger; understanding the flexibility of certain polymers and the role of entropy in the elasticity of rubber brought by Kuhn; and most of the physical properties of polymers subsequently explained by Flory.

Since the 1920s, polymer science has moved on at a dramatic rate. Significant technological advances were made in the synthesis and the applications of polymeric materials during the last century. To date, polymers are perhaps the most ubiquitous and abundantly employed materials in everyday life. This ubiquity of polymers is due to the huge diversity of their chemical compositions and architectures.

The applications of polymeric materials range from biomedicine, where polymers are used for bone/tissue engineering, drug delivery systems, medical equipment such as needles or containers for intravenous delivery of medications; to civil construction materials including insulators, pipes, entirely all adhesives and

sealants; and to electronics manufacturing as, for example, photoresists in micro- and nano- lithographic processes. Following the current trends, a novel class of smart polymers has been introduced. "Intelligent" polymers can respond to external stimuli and change their properties, such as shape or color, which gives them great potential to be used as artificial muscles or sensors.

Among the plethora of manufacturing strategies, a so-called "wet chemistry" group of methods has emerged as a traditional route of polymer synthesis. This group includes such methods as spin-coating or Langmuir-Blodgett technique as well as many others. In general, these methods are all about solvent-based chemical processing of matter, which is often can be considered as resource-intensive. Besides, it has limited monomer versatility (i.e., some monomers cannot be polymerized by chemical routes) and can cause an environmental deterioration due to the lack of cost-effective long-term recycling and storage strategies of chemicals.

The past decades have witnessed a growing interest of scientific and industrial communities towards simpler (since a smaller number of operations needed compared to conventional solution-based chemical methods), more versatile and also to more "green", environmentally-friendly, alternative routes of polymer synthesis and, especially, to vacuum-compatible technologies. The tremendous progress in the development of vacuum and plasma technologies has enabled a new pathway to engineer and, in particular, to synthesize a novel class of polymeric materials with unique properties. The word "plasma" in the title is meant to highlight that this work does not deal with conventional polymers per se. However, it will instead focus on this new pathway and on the materials (these are often referred to as "plasma polymers") that are created as a result of plasma, a low-temperature non-equilibrium electrical discharge, being operated in organic vapours.

In the following sections of Chapter 1, state-of-the-art of plasma polymerization will be discussed to provide the reader with a brief overview on plasma polymer history, plasma basics, plasma chemistry, kinetic models of plasma polymerization and polymer growth, functionalization and technical implementations with a focus on gas aggregation – a feasible technique at hand with broad capabilities.

1.1. Plasma polymerization: state-of-the-art

A historical background

The phenomenon of coatings being formed on surfaces, for instance, metal electrodes in DC systems, exposed to electrical discharge operating in the presence of organic vapours, has been known presumably since the end of the 18th century (see the work [2] and the references therein). For decades, these deposits were considered as undesired byproducts and, consequently, their properties and formation mechanisms were receiving almost no attention. There is a limited amount of reports on plasma polymers published within the 1930s and 1950s, although more deliberate and methodological studies on plasma polymers began in the 1950s, manifesting growing concerns among the scientific community. In the mid-twentieth century, for the first time, plasma polymerization was utilized in the manufacturing of dielectric layers to be used in batteries [3].

To convey an interrelation between the use of an electrical discharge operated in organic vapors and the formation of solid deposits from gaseous precursors of low molecular masses, the term “plasma polymer” was introduced in the 1960s [4–6]. By the time being, the interest in plasma polymers was motivated by the possibility to use different organic monomers, including those which do not polymerize by conventional chemical routes. The only requirement for potential candidates was either to be volatile or to be translatable into the gas phase. A new kind of polymers with advanced properties was anticipated.

It was soon realized that plasma polymers have very little in common with their conventional counterparts because of the inherently different, random structure where regularly repeating monomeric units can hardly be expected. This complexity and some features of plasma polymer structure will be discussed in detail in the next paragraph, yet for the moment, the focus is going to be kept on the consequences of the lack of predictable structure.

In the real-world applications, it hampered the extensive usage of plasma polymers, though a multitude of potential applications has been proposed. For instance, such deposits were studied as possible candidates for the manufacturing of dielectric thin films to be used in microelectronics [7]. The choice of hydrocarbon, halocarbon and organosilicon precursors in these studies reflects the requirement of

the compatibility with technological processes used in semiconductor manufacturing. The legacy of the semiconductor industry had predetermined the research focus on SiH_4-based plasmas [8–11], which subsequently shifted towards hydrocarbon [12–14] and CF- plasmas [15–19]. By that time, the formation of micro- and nano-sized particulates dispersed in the gas phase was observed [8,20–22]. Initially, this phenomenon was regarded as something that should be avoided. Though later, these observations provided a solid basis for the development of the research field, often called "complex plasmas" or "dusty plasmas," which is focused on studying the interactions between particles and plasma [9,23,24].

The complexity of plasma polymer structure

The properties of polymeric material are governed by its topological structure of networks of interconnected molecules (will be referred to as polymer networks henceforth) along with the chemical composition. Typically, networks of different structures will also have a different composition and vice versa. Although specific polymers may exhibit long-range order [25], most of them are semi-crystalline or amorphous. To stress out the key difference between conventional and plasma polymer structure, their topologies are compared. Herein, an elegant approach to describe polymer network topology used in the work of Gu [26] will be adopted.

For the sake of simplicity, the topology of a conventional polymer (Figure 1a) networks can be represented by two components: a strand, which is merely another name for polymeric chains (denoted as lines), and a junction that can be regarded as connecting point (denoted as dots). The polymer network topology spans over at least three different scales: < 1 nm, 1–10 nm, 10–100 nm.

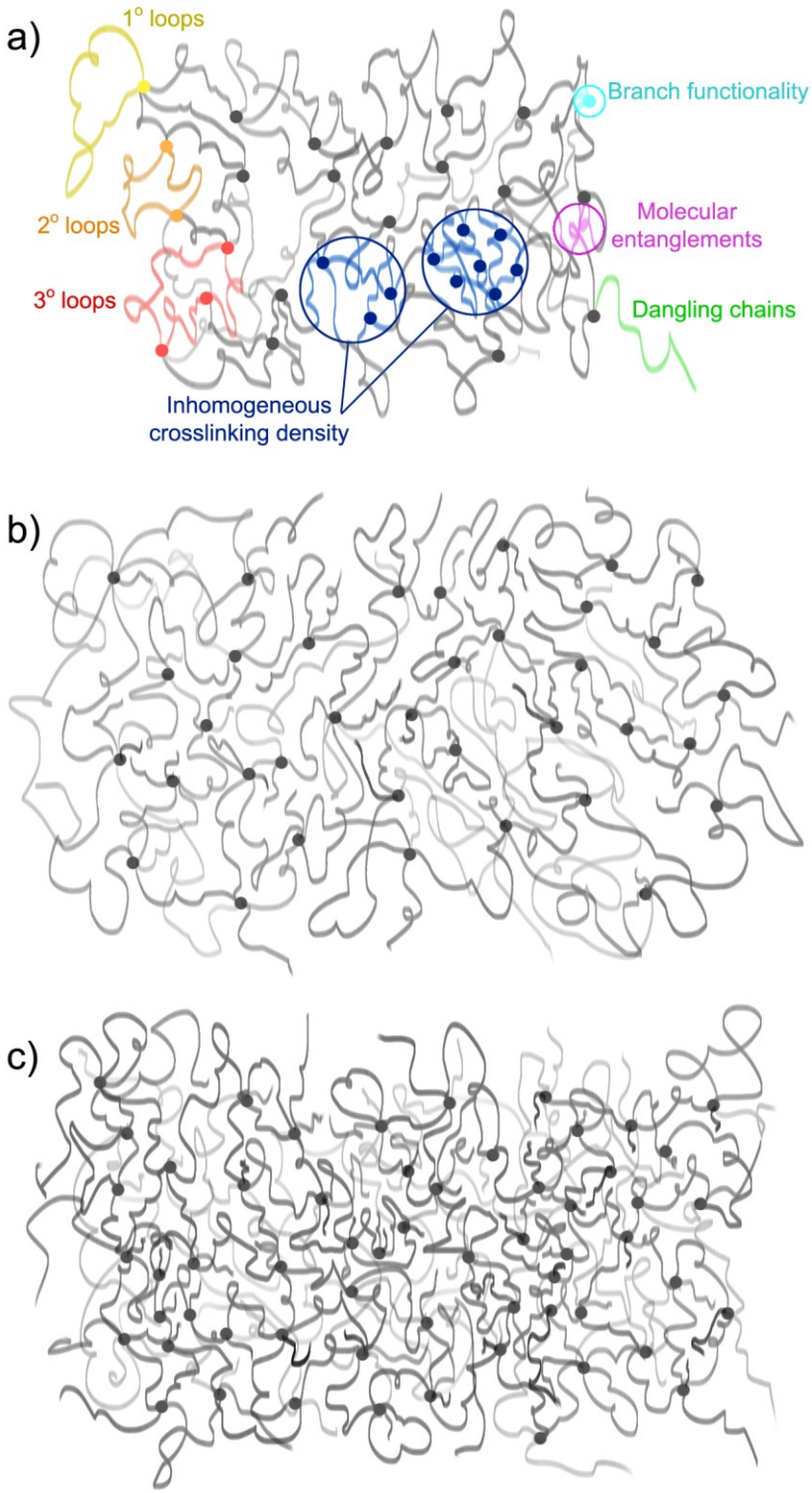

Figure 1. Hypothetical structure of a) conventional polymer, b) a transitional entity - plasma polymer having a relatively low degree of cross-linking (high retention of monomeric structure) and c) plasma polymer with a high degree of cross-linking (low retention of monomeric structure units).

At the length scale of 10-100 nm (marked with blue color), the inhomogeneity in the local distribution of crosslinking junctions is the dominant topological feature. It results from fluctuations in the concentration of monomeric units during the polymerization process and the formation of the network [27]. A more in-depth outlook of network inhomogeneity can be found elsewhere [28,29].

The next scale range on the line is from 1 to 10 nm, where mainly macromolecular-level structures contribute to polymer network topology. These structures can be formed by one or multiple strands and include unreacted functionalities, such as dangling chains (marked with green color), molecular entanglements (marked with magenta color), and loops of various order. The loop order corresponds to the number of strands in the loop: a primary loop (1° loop, marked with yellow color), a secondary loop (2° loop, marked with orange color), and a ternary loop (3° loop, marked with red color).

Finally, below 1 nm polymer networks comprise molecular-level structures that extend to about ten chemical bonds or fewer. The properties here are highly dependent on the chemical composition of the network precursors. Nevertheless, there is at least one critical topological feature that falls into this length scale: a branch functionality (marked with cyan color), which describes the maximum number of strands connected to a network junction.

Upon the transition from conventional to plasma polymers, the topology dramatically changes. Figure 1b and 1c demonstrate hypothetical structures of plasma polymers with a low and high degree of cross-linking, respectively. The topology turns into more chaotic with minimal contribution from regularly repeating units. The polymeric chains are highly branched and randomly terminated. Such a “disordered” structure is logically stemmed from the deposition processes under non-equilibrium plasma conditions that will be discussed in more detail across the following three paragraphs.

Plasma

The plasma is a matter beyond its gaseous state where atoms are stripped of at least one electron in their outer shells so that what remains are positive ions in a sea of free electrons. In reality, though, the system is more complex and contains not only

electrons, cations and anions but also neutral particles such as atoms and/or molecules both in their ground and excited states.

The term “non-thermal” refers to the classification of plasmas based on the relative temperatures of the species therein [6,30]. In general, in non-thermal (non-equilibrium) plasma electrons are predominant charge carriers. Their temperature could reach several eV (~10^4 K), while minor ions or neutrals remain at nearly ambient temperature (~300 K). The degree of plasma ionization is low and, in most cases, corresponds to the situation: 1 charge carrier per 10^6 neutrals. Upon interaction with the electric field, electrons are able to gain kinetic energy much faster than ions, and quantitatively this can be expressed via the factor of $\sqrt{m_i/m_e}$, where m_i and m_e are the mass of an ion and an electron, respectively.

A low-pressure glow discharge is the most common example of non-thermal plasma. In its simplest implementation, two metal electrodes are placed into a vacuum chamber filled with inert gas. When the potential is applied between those electrodes, the charge carriers are generated via the avalanche-like gas ionization process. The minimal voltage required to ignite a self-sustained discharge is known as the breakdown voltage. In practice, it depends on the gas pressure inside the chamber as well as the interelectrode distance. The relation between these parameters is described by a Paschen's law:

$$V_{br} = \frac{B(pd)}{C + \ln(pd)} \tag{1}$$

where p is pressure, d – interelectrode distance, B and C are constants defined experimentally [31].

The non-thermal plasma is often characterized as a quasi-neutral medium, meaning that plasma tends to be overall electrically neutral, though the neutrality can be violated at smaller length and time scales [5].

To date, there is a wealth of other technical implementations with various reactor geometries, types of discharges, etc. A more detailed discussion will follow, yet for the moment, it is sufficient to distinguish between two primary types of discharges based on how external power is supplied to it. Depending on the power supply, the plasma can be driven either by direct current (DC) or alternating current (in most cases radio-frequency, denoted as RF here and further in the text).

In the case of DC, the electric field accelerates electrons towards the anode, while positively charged ions are dragged by the field in the opposite direction. The

cathode is bombarded with ions and the atoms on the cathode surface are supplied with an excess of energy, causing them to escape. Thus, the cathode material is sputtered. If the cathode is covered with a non-conductive material, the positive charge accumulates on its surface, preventing the emission of secondary electrons from the cathode and disrupting the discharge operation [5].

On the contrary, the RF-driven discharges are characterized by the alternating potential on the electrodes with specific frequency ranging from hundreds of kHz to tens of MHz. High frequency makes "heavy" ions almost immobile because they are unable to quickly respond to the high oscillation rate of the electric field, whereas electrons continue to oscillate. During the oscillation half-cycle, the electron current exceeds that of ions (Figure 2a); the discharge itself is retained through the electron-impact ionization. Thus, the key difference between DC and RF-driven discharge is that the latter is independent of the processes at the electrodes. Here, the electrodes can be covered by any material, including insulators.

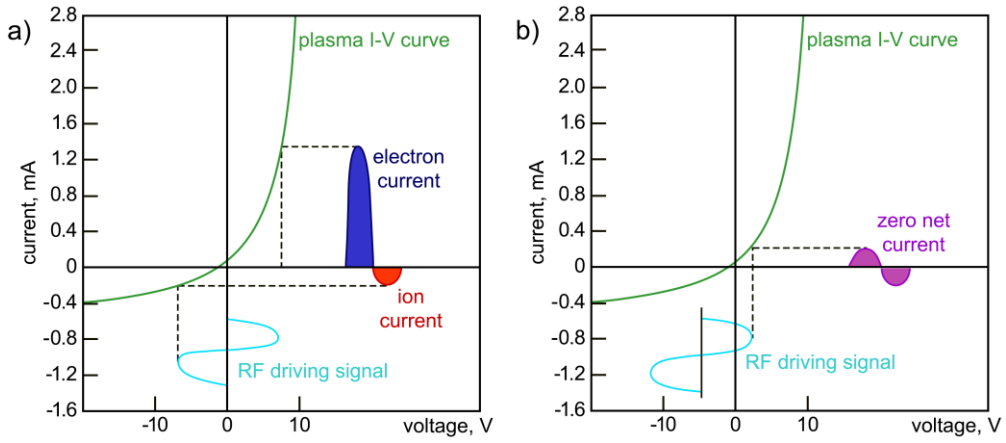

Figure 2. a) I-V curve of the RF-driven discharge and dependence of electron/ion currents on RF driving signal; b) Formation of the negative self-bias on a capacitively coupled electrode in an RF discharge (adapted from [32]).

In practice, one of the electrodes is capacitively coupled (e.g., connected via a series capacitor or the impedance matching box) to the power supply, which results in the formation of pulsing negative potential on the electrode. The net current becomes set to zero because the negative self-bias repels mobile electrons and draws the ions, thus balancing their currents (Figure 2b). Once this happens, the electrode behaves as a cathode (target) in DC discharges where ion-bombardment sputters away atoms for

subsequent deposition. In capacitively coupled RF discharges, the voltage drop near the cathode defines the intensity of the ion bombardment. Usually, the chamber walls serve as a large area anode (grounded), while the cathode remains relatively small to provide the highest voltage drop near the cathode (RF-driven) and to avoid contamination from the sputtering of the anode.

Basic plasma chemistry considerations

In general, chemical reactions that proceed under plasma conditions are very complex and nonspecific. For convenience, the description of these processes is compartmentalized to several following parts, dealing with the basics of plasma chemistry, plasma polymerization, polymer aggregation, and growth kinetics. This part provides the reader with foundations of plasma chemistry, describing the processes responsible for the formation of radicals as primary building blocks for plasma polymerization.

When reactive precursors are added to the gas phase, the complexity of the plasma increases significantly as many extra chemical and physical processes come into play. For example, fragmentation of the precursor molecules results in the formation of a variety of radicals that are smaller than the precursor, while charging processes result in a wide variety of species which range between very small (from a single proton) and very large (protonated oligomers).

In chemical terms, an atom, molecule, or ion that has unpaired valence electrons or an open electron shell fits the description of a radical. The radicals are highly chemically reactive towards other substances, or even towards themselves: their molecules will often spontaneously dimerize or polymerize if they come in contact with each other. Free radicals may also take part in plasma polymerization reactions.

Under plasma conditions, energetic electrons can induce many processes that would otherwise be very improbable at low temperatures, such as dissociation and ionization of precursor molecules (Figure 3a). Such reactions are a primary source of free radical and ions. Given that the ionization threshold of organic molecules (~9-13 eV) is considerably higher than the energy of chemical bonds (~3-5 eV), the concentration of free radicals in plasma is generally up to 10^5 times greater than that of ions. Thus, the electron-impact dissociation events require less energy than direct

ionization events, in which only electrons in the high energy tail of the electron energy distribution participate (Figure 3b).

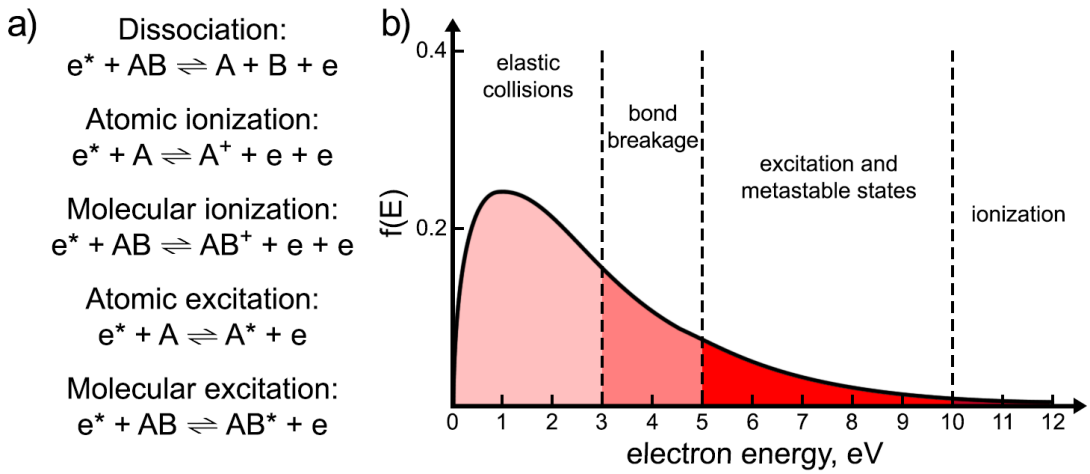

Figure 3. a) Pathways of radical formation and basic reactions taking place in plasma; b) electron energy distribution function typically observed in low-pressure non-thermal plasma.

Kinetic models of plasma polymerization

To describe the interactions between precursor molecules and plasma, multiple polymerization models were developed. Among the first attempts, Williams and Hayes [7] proposed a model where plasma polymer growth proceeds via two subsequent stages. In the early stage, polymer film grows via reactions between monomer molecules adsorbed to the substrate surface and activated intermediate species resulted from the adsorbed molecules being bombarded with incoming positive ions. In the next stage, when the first layers of plasma polymer are deposited, polymer surface molecules become activated as well to contribute to the propagation of the polymerization reaction.

Denaro et al. [20,33,34] suggested that energetic electrons bombarding the polymer film covering the electrodes are primarily responsible for the initiation of the polymerization reaction, resulting in the formation of surface free radicals that react with the adsorbed monomer molecules. Westwood proposed a similar model with the exception that initiation relied on the activation by bombarding positive ions [35].

Later on, Poll et al. [36] developed a model based on the processes on the surfaces adjacent to the discharge region, e.g., adsorption, desorption, and polymerization. The model considered the processes of the formation of new compounds by the transformation of the monomer under the influence of the discharge. For more details, please, see Reference [5].

Lam et al. [37] developed a concept of free radical plasma polymerization including the following steps: (1) formation of radicals via activation of precursor molecules by electron impact (initiation); (2) attachment of radicals to intact monomer molecules, which involves opening of unsaturated carbon bonds and results in an increase of the molar mass (propagation); (3) termination of chains through radical recombination as in the conventional polymerization. Four mechanisms were examined considering the above mentioned three steps taking place either in the gas phase or on the surface. Comparing the theory and experiment, the following model was recognized as the most plausible: the initiation phase proceeds in the gas phase while the propagation and the termination phases take place mostly on adjacent surfaces (Figure 4a). Quite a similar model for plasma polymerization of unsaturated hydrocarbons in an RF discharge was proposed by Tibbitt et al. [38].

Yasuda and Hsu [39] introduced a competitive ablation and polymerization mechanism (CAP) as the further development of plasma polymerization theory (Figure 4b). In general, a precursor passing through the plasma region is turned into the complex mixture of intact molecules, excited or ionized fragments and neutral gaseous byproducts that do not participate in plasma polymerization. The model took into consideration chemical reactions between the intact monomer molecules and free radicals (plasma-induced polymerization) and between polymer-forming intermediates (plasma-state polymerization). The CAP also includes the processes of ablation induced by positive ion bombardment. Ablation releases gaseous byproducts which either become reactivated and, therefore, can participate in the polymerization, or are pumped out from the reaction zone. If the rate of the ablation exceeds that of the polymerization, the polymer film growth is mitigated.

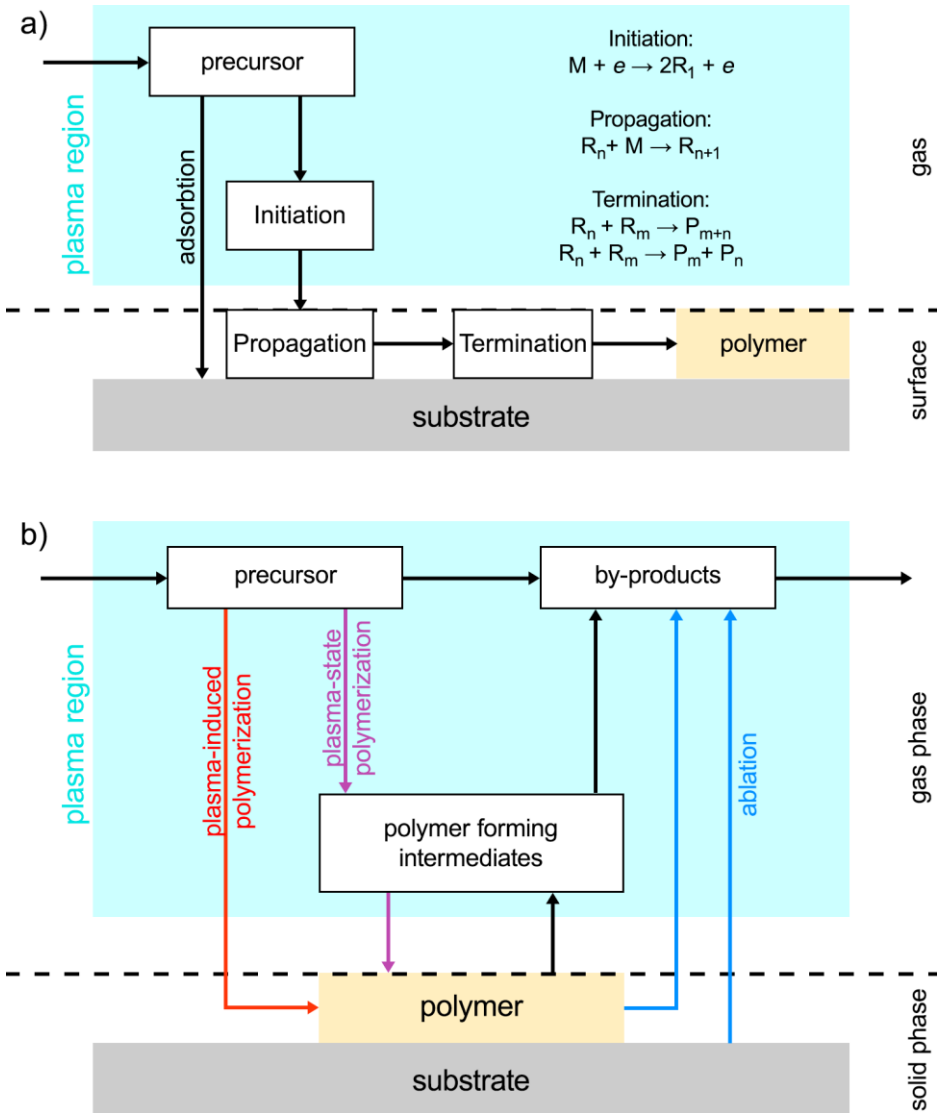

Figure 4. Schemes of a) free radical plasma polymerization model elaborated by Lam and b) competitive ablation and polymerization model developed by Yasuda and Hsu.

In the CAP model, Yasuda suggested a more complex rapid step-growth mechanism of plasma polymerization (Figure 5). The main idea behind it is the existence of two cycles and cross-cycle reactions that can contribute to plasma polymer growth. Here, the first cycle is similar to the previously described free radical polymerization mechanism and involves the reactions of monofunctional radical species either with intact monomer molecules or with each other. In addition, the second cycle represents interactions between bifunctional species (i.e., the monomer species containing cationic as well as radical propagating centers or bi-radicals). These

bifunctional entities enable the propagation of the polymeric chain in multiple directions simultaneously.

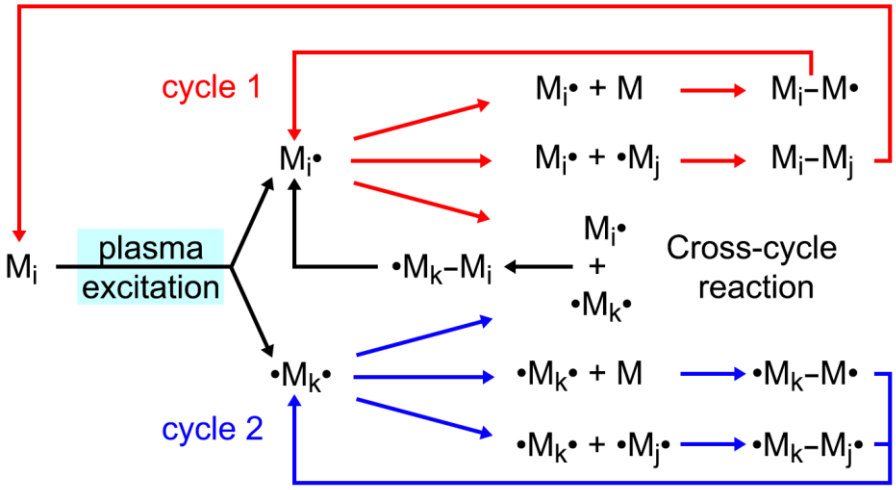

Figure 5. The rapid step-growth polymerization mechanism concept developed by Yasuda (adapted from [5]).

Later, d'Agostino suggested an activated growth model of plasma polymerization of fluorocarbons [40]. This model took into account contributions from electron and ion bombardment of the surface and interrelated these parameters with the plasma polymer growth and its properties. The energetic electrons and ions are considered responsible for precursor molecules desorption from the substrate as well as for sputtering and cross-linking in the growing film. Thus, the control over the energy of incoming species is a key to the tailoring of the resulting film properties. Ions are "soft-landed" under the low power conditions, which are often used to functionalize a surface. This means that the degree of etching and rearrangement of atoms on the surface is low. On the other hand, at higher powers, etching and ion bombardment may become an issue for the growth of the film with the required functionality.

Finally, R. Short and J. Bradley highlighted the important role of negative and positive ions in low-pressure plasmas [41–43]. They suggested extending ions influence to the gas phase, while previous models were more focused on the surface. For example, in the case of acrylic acid plasma, a large amount of ion-neutral chemistry takes place within the bulk plasma. Unlike the neutral species, the deteriorative influence of positive ionic species can be controlled via the application

of the bias potential, which may dramatically reduce the fragmentation of the precursor molecules. Besides, changing the ion energy within the sheath can influence the reaction preferable pathways because the cross-sections for the different kinds of ion-neutral collisions are found to be energy-dependent.

Equilibrium thin film growth modes

The growth of thin films on solid supports was approached theoretically early in the 20th century. The experimental observations of the film formation on the crystal surface pointed towards three primary growth modes: (1) island (or Volmer-Weber), (2) layer (or Frank-van der Merwe), and (3) Stranski-Krastanov, which are illustrated schematically in Figure 6. The models consider only energetic aspects of the interaction between the adatoms and the surface, and do not take into account any kinetics.

If the atoms or molecules of the deposited material are more strongly bound to each other (by a cohesive force) than they are to the substrate (by an adhesive force), the island (3D) or Volmer-Weber mode dominates (Figure 6a). Mostly, it occurs when the small stable clusters nucleate on the substrate and then grow in all dimensions. The growth of these clusters leads to the formation of rough films on the substrate.

In the opposite case, where the atoms are more strongly bound to the substrate than to each other, Frank-Van der Merwe mode or layer-by-layer growth is dominant (Figure 6b). Herein, adatoms attach preferentially to surface sites resulting in atomically smooth, continuous planar sheets. The layer-by-layer growth is two dimensional, and a new layer begins to grow once the underlayer is formed. The first complete monolayer is then covered with a second layer where atoms are less tightly bound to the substrate.

The Stranski-Krastanov (layer and island) growth mechanism (Figure 6c) is an intermediate combination of the aforementioned modes. It is characterized by both 2D layer and 3D island growth, and after forming one or more monolayers, subsequent layer growth becomes unfavorable, and island formation is triggered. The transition from the layer-by-layer to island growth is not yet completely understood, but, in general, any factor introducing a disturbance in a monotonic decrease in characteristic binding energy for layer growth may be the cause: for example, the misfit between the

film and the substrate due to the different lattice parameters of materials. When a thin film is grown on a thick substrate, the misfit strain at the interface will eventually trigger the transition. Initially, the film grows in layer-by-layer mode and some amounts of strain energy become accumulated in the deposited layers. At a specific critical thickness, the strain induces a transition in the island growth mode. Thus, it becomes energetically favorable to nucleate islands and further growth occurs by the island growth mechanism. The critical thickness depends on the lattice mismatch between the film and the substrate, where the critical thickness is reversibly proportional to the amount of the mismatch. The in-depth review of thin film growth modes and peculiarities of interrelation between plasma parameters and thin film properties can be found in the [44] and the references therein.

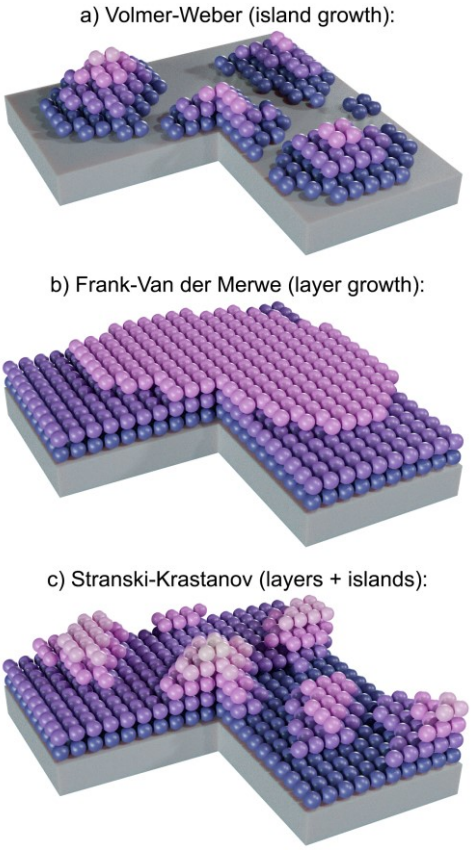

Figure 6. Historically first three primary modes by which thin films grow at a crystal surface.

Non-equilibrium kinetics models of thin film growth

Many real deposition processes proceed under conditions that are far from equilibrium. Over the past decades, a wealth of various kinetic models were developed. There are two primary groups all the existing models can be divided into: discrete and continuous models.

Discrete models are more favorable from a modeling perspective because they are relatively simple to create and can yield quite realistic predictions within a short timescale. These models evolve the system under a set of simple rules. These rules are stochastic, leading to the requirement that average values must be taken to obtain results comparable to experiments.

On the other hand, the foundation of continuous models lies in solving a differential equation to find the variation with time of the interface height $h(x, t)$ at any position x, where x belongs to a d-dimensional substrate. The primary advantage of continuous growth models is the ability to choose as many specific functions (terms) describing certain changes as necessary. It makes models of this type more versatile, yet also increasing their complexity.

In terms of this thesis, the following three discrete models will be discussed: Diffusion Limited Aggregation (DLA), Attachment Limited Aggregation (ALA) and Cluster-Cluster Aggregation (CCA) that are relevant for the growth of PE fractals and dendrites on PEO.

In 1981, Witten and Sander [45] developed the Diffusion Limited Aggregation (DLA) model (Figure 7a) to describe an irreversible aggregation of diffusing particles (atoms, molecules, etc.). Being one of the first fractal growth models, it has a very simple growth ruleset, yet it can be used to model various real-world processes and to perform the quantitative study in terms of fractal dimension. First, a lattice where the deposition process is simulated becomes initialized. This lattice usually has either two or three dimensions and a characteristic size of 1000 lattice points per one dimension. The DLA simulates the growth of only one cluster at a time that begins with an immobile seed placed on the lattice plane at the origin of coordinates. At each simulation step, a new particle is added to a random position far away and is allowed to diffuse freely. If the particle touches the seed, it is immobilized instantly and becomes part of the cluster, and a new simulation step begins, where similar walkers will be launched one-by-one. The critical requirement is to keep the number of

particles undergoing Brownian motion extremely low so that only the diffusive nature of the system is present. This model typically yields islands having an irregular shape of randomly branched fractals that can occur in nature. The examples are the aggregation of dust particles, the growth of fractals in the solution of electrolytes, the injection of a liquid into a more viscous one, or dielectric breakdown in an insulator.

In some instances, the DLA model yields non-relevant predictions because it does not take into account processes at the rim of growing fractal. There might exist multiple unfavorable configurations for atom/molecule incorporation, resulting in an effective attachment barrier at the island edge and, therefore, in an integral attachment probability being smaller than unity. Kandel [46] and Venables with Brune [47] considered a more realistic scenario, where the incorporation of the approaching monomers molecules at the island rim is hindered by an activation barrier. This scenario laid in a foundation of the Attachment Limited Aggregation (ALA) model (Figure 7b). For example, such fractal rim barriers can exist in surfactant mediated growth, where the island edge atoms first have to be removed in order to attach further approaching atoms [48]. Another case was considered in the Reference [49], where the attachment probability depends on the relative orientation between the approaching molecules and the molecule alignment at the edge of the island. The overall number of captured molecules for a particular island depends on both the diffusion barrier and the attachment barrier. Venables and Brune [47] have shown that if the attachment barrier is negligible compared to the diffusion barrier, the nucleation and growth are diffusion-limited. For the reverse situation, they both are attachment-limited.

In the case of Plasma-Enhanced Chemical Vapor Deposition (PECVD), the vaporized molecular fragments are typically randomly oriented. However, by close analogy with both DLA and ALA, one can assume that the nucleation and aggregation will be in the DLA regime at a sufficiently low deposition rate while the mechanism shift to ALA is expected for high deposition rate. Besides, Winkler et al. showed that the surface roughness, and therefore the diffusion probability on the surface, plays an essential role in the nucleation and aggregation mode. For instance, the nucleation process can shift from attachment-limited to diffusion-limited by an increase of surface roughness [50].

Neither DLA nor ALA models do account for multiple-body kinetic phenomena. In reality, the atoms or molecules do not wait for one another to adhere to a cluster, but they diffuse simultaneously and, hence, can suffer from collisions with

each other. In addition, the growing fractal should not necessarily be immobile, and it can move either. To describe the growth of fractal in real time, a Cluster-Cluster Aggregation (CCA) model had been developed by Meakin [51] and Jullien [52] independently (Figure 7c). The simplest implementation includes several particles (typically circular with a specified radius) being launched from randomly chosen positions at the lattice surface to perform Brownian motion. Upon a collision, two particles adhere to one another to form a cluster, which then continues to diffuse. In more realistic implementations of this model, the diffusion constant is no longer constant and becomes dependent on the cluster size. What differs CCA models from two previous is its ability to generate completely anisotropic shapes while having no anisotropy being added to the set of growth rules.

More details about the growth models and the practical implementations can be found elsewhere [53].

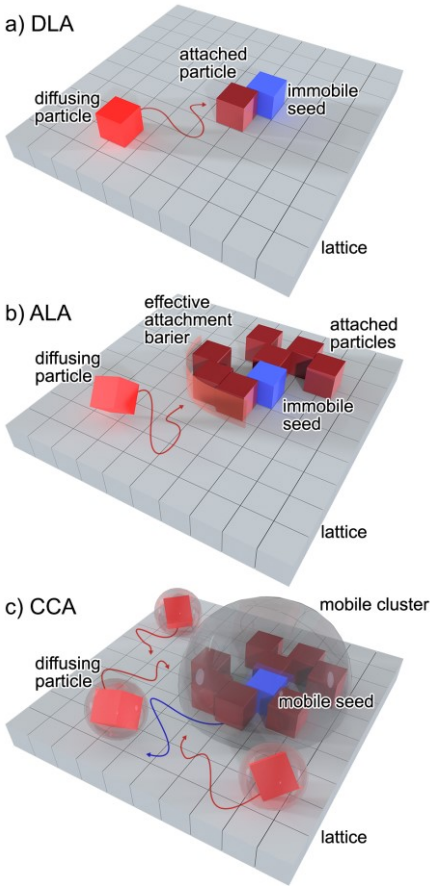

Figure 7. Schematic representation of a) Diffusion-Limited Aggregation, b) Attachment-Limited Aggregation and c) Cluster-Cluster Aggregations models.

Phase transition and segmental dynamics phenomena in polymer thin films

The growth of polymer film is frequently accompanied by phase transitions. These phase transitions in general, and segmental dynamics phenomenon in particular, are of paramount importance because polymer engineering heavily relies on the manipulation of segmental dynamics by chemical and/or compositional means in an attempt to target particular technological or industrial requirements.

The segmental dynamics in amorphous polymer film is represented by a glass transition phenomenon. According to the IUPAC, a glass transition is defined as "a second-order transition in which supercooled melt yields, on cooling, a glassy structure" [54]. In other words, it is the reversible transition from a molten or rubber-like state into a stiff and brittle glassy state.

For convenience, the glass transformation region is typically represented by a single value, denoted as the "glass transition temperature" (or more simply - T_g) [55]. In reality, though, assigning a characteristic T_g to a particular system quite often becomes a problematic task because T_g depends on a timescale involved in the molecular segments' rearrangement. Nevertheless, the glass-transition temperature has become recognized as one of the most important amorphous polymer properties, directly relating to multiple other thermophysical and rheological properties, processing parameters, and fields of potential application [56].

The location of the glass transition region can be tuned by changing the polymer film composition, degree of the chain-to-chain interactions, and amount of free volume, while the structural heterogeneities at the nanometer scale determine how broad that region is. In experimental practice, two general cases can be distinguished: single-phase and phase-separated systems. The first case can be represented, for example, by a copolymer with randomly alternating blocks along the backbone chain or by a pair of miscible polymers. Here, a single and rather broad glass transition is observed. On the other hand, the glass transition of phase-separated system, such as block copolymers, polymeric blends or plasma polymer cross-linked networks, demonstrates an elevated level of complexity given by multiple peaks or components of various broadness and position. The notions, derivations of common theoretical models of the glass transition and challenges in the interpretation of fundamental

phenomenological aspects of the glass transition are discussed in great detail in the [57] and the references therein.

In many cases, the relaxation of macromolecules proceeds under far-from-equilibrium conditions, making kinetics responsible for the resulting morphology of thin polymer films. The proximity of a rigid substrate can significantly confine the configurational entropy of macromolecular chains. The timescale at which the surface diffusion and/or molecular relaxation occur governs the morphology of deposited coating. To date, the formation of a broad diversity of kinetically-controlled patterns in polymer films has been extensively studied. These patterns are classified into two main types of compact and fractal islands. In addition, each type is subdivided into dendrite (exhibiting orientational symmetry) and seaweed (randomly ramified) islands [58]. In Section 3.3.4, the influence of nanoconfinement and glassy dynamics described previously on such pattern formation will be discussed.

Technical implementations

Typically, plasma polymerization occurs under low-pressure non-thermal discharge conditions, though recently, atmospheric plasma gained popularity as well. Over the past decades, many different deposition techniques have been developed and implemented in the laboratory environment and specific industrial sectors. All existing deposition systems arrangements are divided on the basis of electrode configuration they utilize: a) systems with internal electrodes (DC-driven plasma only), b) systems with external electrodes (AC or RF-driven plasma), and c) electrodeless systems (MW-driven discharges).

Among the first group, the two most popular arrangements are reactors with symmetric parallel-plate electrodes (Figure 8a) and systems with asymmetric electrode configuration (Figure 8b). In practice, the symmetric arrangement has a pair of metal electrodes run by an AC or RF power supply. The interelectrode separation, in this case, is the smallest and falls into the range of several centimeters. The pressure of the gas mixture (inert gas, such as Ar, with the addition of monomer vapors) is usually kept within units to tens Pa. More advantageous asymmetric geometry is broadly employed for the sputtering of polymeric targets. Here, a circuit of permanent magnets is installed inside the excitation electrode to be used as a planar magnetron. The magnetron is RF capacitively coupled (alternatively, it can be run by DC power

supply) and isolated from the grounded chamber, which serves as the second electrode. The substrate holder can be either grounded, under a floating potential, or biased.

The second commonly employed geometry is a tubular reactor made of glass or silica and wrapped by either a pair of outer-ring excitation electrodes (Figure 8c) or an excitation coil (Figure 8d). This configuration is usually powered by RF and enables the capacitive coupling of the energy into the discharge. Since the electrodes as potential sources of impurities are removed from the chamber, the contamination of the growing film is highly unlikely and, therefore, it is not surprising that these reactors are often classified as electrodeless. The definition is not entirely correct because DC negative self-bias appears on the inner walls near the outer electrode (e.g., coil) as a result of capacitive coupling. The substrate holder can be placed in the afterglow or entirely outside of the plasma zone (as shown in Figure 8d) to avoid excessive ion bombardment and UV irradiation of the growing polymer film, significantly increasing the retention of the original monomer structure.

The truly electrodeless reactors utilize microwave power for plasma polymerization. The schematic representation of the simplest microwave reactor geometry is shown in Figure 8e. Microwave-powered deposition systems are comprised of a silica cylinder chamber (or tube) located inside (or passing through) the resonant cavity coupled to a microwave power supply (2.45 GHz). Here, the cavity plays a role of the excitation electrode. Plasma is ignited inside the chamber within, and substrates are positioned downstream.

A rather unique and relatively new plasma polymerization system is illustrated in Figure 8f. This deposition method employs bulk polymer precursor thermal decomposition assisted by RF-driven plasma. Upon the decomposition process, oligomer molecules are released into the vapor phase in the form of a beam passing through the plasma zone to generate the radicals. These reactive species then react with each other with the formation of a plasma polymer. This method was applied for the deposition of plasma poly(ethylene oxide) (PEO) thin films in the current study. For more details, please, refer to Section 2.1.2 and 2.1.3.

Real-world use cases of the deposition systems are meticulously described in the [5,59,60] and the references therein.

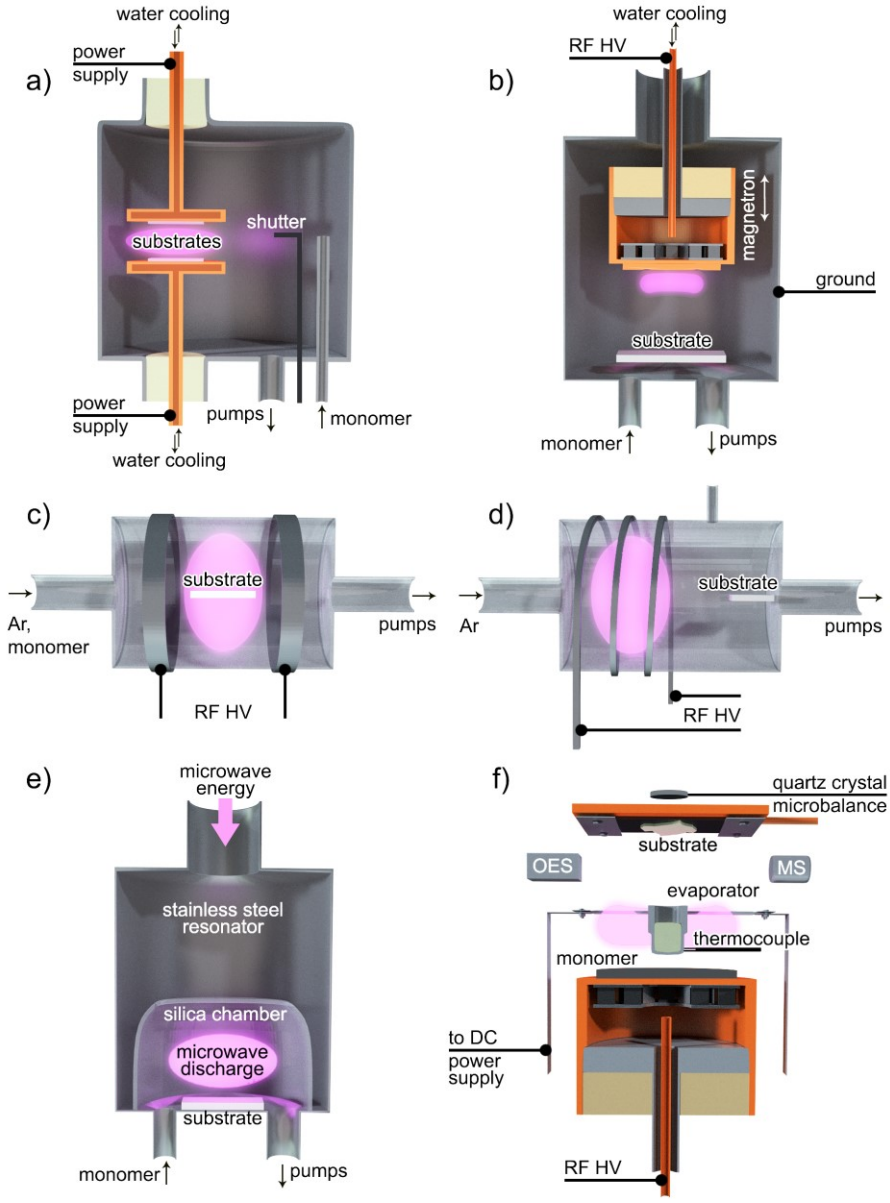

Figure 8. Schematic representation of different deposition systems.

Challenges and applications perspectives

A diverse variety of applications for plasma polymers becomes accessible via tailoring their properties by proper choice of the production techniques and operational conditions. In particular, tailoring resulting properties of plasma polymers refers not only to a coating morphology and physical properties, but also to its chemical composition. It is known that organic precursors bearing specific functional groups can be polymerized by plasma to deposit thin films with these functionalities retained in the final structure. In this part, one can find a brief overview of potential applications

of functionalized and nanostructured acrylic acid (AA) and PEO based plasma polymers, which became a motivation for the research presented in this thesis.

Over the past years, immobilization of biomolecules in a controlled way has emerged as a hot topic in biomedicine and surface science. Being beneficial for the development of artificial implants regardless of material [61] or novel drug/gene delivery systems with pH behavioral programming, it also contributes to a better understanding of the biomolecule/surface interactions the biocatalysis and biosensing rely on. This research is more aimed at the concept of masquerading surfaces by functionalization with biomolecules from living tissues that might be extremely useful in avoiding foreign body reactions and integration the device into the host. At the molecular level, it can be viewed as guidance of the cells adhesion by surface-attached bioresponsive agents, such as proteins, via the interactions of these proteins with cell integrin receptors. The protein attachment to the substrate can be controlled by adjustments in the surface chemistry and morphology. Moreover, electrostatic and/or chemical interactions can govern protein adhesion if specific chemical groups are present on that surface.

Plasma polymerization of acrylic acid has become a pathway to the synthesis of thin films enriched with the carboxyl groups [41,43,62]. The AA-based plasma polymers were studied for their ability to bind biomolecules [63–65] and as supports for the cultivation of cells, [66] including cancer [67] and stem cells [68]. In practice, the adjustments in characteristics of the resultant plasma polymer can be made by merely a variation of macroscopic parameters, such as power delivered to the plasma, and the precursor flow rate. On the other hand, the main challenge which remains is the low stability of plasma polymerized acrylic acid thin films in aqueous media, often becoming a limiting factor for biomedical applications [69,70]. If deposited under improper plasma conditions, thin films of polyacrylic acid dissolve quickly, leading to acidification of the immediate surroundings, which has detrimental effects on cells and tissues, similar to what is observed during infection [71,72].

Targeting the synthesis of thin films with variable elemental composition, the mixing of acrylic acid with different monomers was investigated as well [73–78]. Hydro- and fluorocarbon, amine-containing, and other moieties can be embedded into deposited films employing plasma co-deposition. This method allows the production of coatings with the unconventional chemistry that is readily tunable via the ratio of the supplied precursors. In structural terms, the plasma co-polymers are characterized

by a high degree of homogeneity. Simply put, molecular fragments of the two precursors recombine with the formation of a plasma polymer matrix, randomly blended at the molecular level. The versatility of plasma-based methods enables the preparation of plasma co-polymers with variable surface chemistry, which can be beneficial for the organization of the immobilized proteins in a predetermined manner and affecting signaling between the surface and the approaching cells [79].

Typically, in the plasma polymerization community, microscale patterning is realized via a step-by-step deposition of different films using a mask [80,81]. Our group demonstrated that plasma co-polymers with nanoscale phase separation can be prepared using plasma-assisted vapor phase deposition [82]. In this thesis, the compartmentalization approach to decouple polymerization processes involves the incorporation of functionalized plasma polymer NPs as ready-made entities into a matrix of another polymer.

To date, there are limited studies of the gas-phase formation of NPs enriched with specific functional groups. For example, nitrogenated NPs were synthesized either by RF sputtering of nylon target or by plasma polymerization of volatile hydrocarbons with N_2 admixture [60,83]. Additionally, it was shown recently that C:H:N NPs produced using the plasma operated in the gas mixture of acetylene, Ar and N_2 have great potential as linker-free nanocarriers with good permeability through the cell membrane while maintaining almost negligible cytotoxicity [84].

1.2. Gas aggregation as a pathway to synthesis of functionalized bi-component plasma polymers

A significant number of different plasma polymerization techniques have been suggested within the last few decades. In the vast majority of non-thermal plasma-based methods, thin films are grown on the solid supports, generally placed inside the processing chamber, where the polymerization occurs. Here, the nucleation and the growth of the film depend either on the supply of radicals and monomer atoms/molecules from the gas phase or on the diffusion over the solid/vacuum interface. As a consequence, in the case of bi-component plasma polymer composites, potential barriers are lifted in precise control over the resulting coating structure and,

hence, its properties. Besides, it is more complicated and resource-intense to deposit NPs using the all-in-one type of reactors per se.

To overcome these barriers, a step-by-step approach involving deposition from several sources at different conditions is commonly employed. In the current work, a compartmentalization approach, where the synthesis of NPs is spatially and temporarily decoupled from the incorporation into a growing thin film, is used. For this purpose, plasma-assisted vapor phase deposition of thin films was combined with a gas aggregation of NPs.

The gas aggregation is a rather old technique that became broadly employed in the synthesis of metal NPs. The pioneering work by Pfund [85] triggered the development of several experimental approaches through the following decades. Numerous advantages of such a physical synthesis route were recognized quickly. Compared to a family of "wet chemistry", it enables greater control over the morphology and characteristics of the NPs, while maintaining low levels of material consumption and hazardous releases, thus, not contributing to the environmental deterioration. Although, it should be noted that gas aggregation technical implementations may sometimes require expensive and, to some extent, sophisticated toolset.

Though being diverse at first glance, all gas aggregation-based techniques share a common feature: atoms should be transferred into the gas phase, and then the conditions of supersaturation should be created to trigger the spontaneous nucleation and the NP formation. Many different types of gas aggregation cluster sources (GAS) were suggested with the main difference of how the material is supplied into the gas phase. One of the most popular GAS systems involves magnetron sputtering [86]. In this approach, the magnetron is utilized to supply the material, typically metal, from the target into the gas phase. In general, processes of atomic condensation are described by five stages, as illustrated in Figure 9.

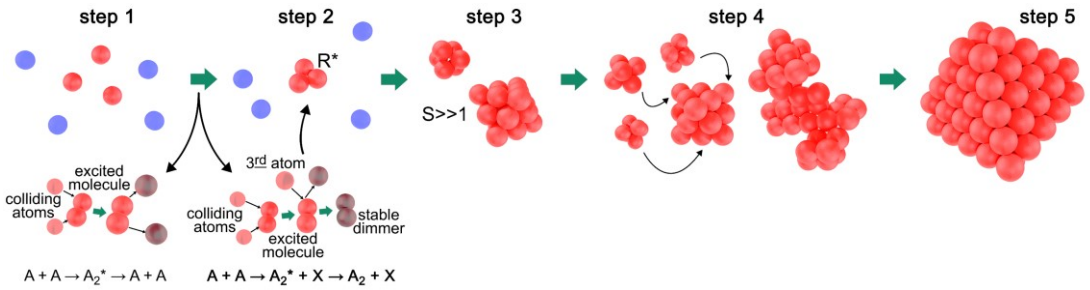

Figure 9. Schematic step-by-step representation of the mechanism of metal nanoparticle formation in GAS.

First, sputtered atoms escape from the target with hyperthermal energy and are forced to thermalize upon the interaction with the atoms of the cold inert gas (Figure 9, step 1), resulting in the spontaneous nucleation (Figure 9, step 2). Stable dimers act as critical seeds for further condensation of new sputtered atoms (Figure 9, step 3). At the initial stages, the NP growth proceeds via the attachment of incoming single atoms to the cluster; however, it becomes accompanied by the coagulation and coalescence processes (Figure 9, step 4). Finally, the rearrangement of the inner structure of the nanoparticle occurs (Figure 9, step 5). The inert gas flow is typically created by the pressure difference between the aggregation chamber and another vacuum chamber to drag the NPs from the aggregation zone into that chamber, where they can be collected on substrates. More information on NPs formation and growth mechanisms can be found elsewhere [87–89].

The feasibility of the GAS systems for the production of single-metal [90] alloyed [91] and heterostructured [92] NPs have been explicitly demonstrated. The versatility of the GAS systems extends even further, allowing one to produce plasma polymer NPs.

The formation of plasma polymer nanoparticles is complex by its nature and can involve many specific mechanisms that are strongly linked to the plasma operational conditions such as gas mixture composition, overall pressure, the power delivered to the plasma. However, for the sake of simplicity, three primary stages can be distinguished in the NP formation process as schematically shown in Figure 10 (for the case of C_2H_2): nucleation (step 1), coagulation (step 2) and surface growth (step 3). The NPs are created only at elevated pressure, typically tens of Pa, which can be explained by a higher collision rate.

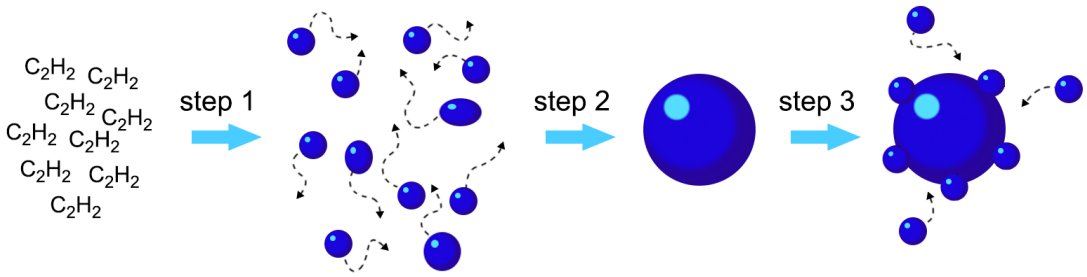

Figure 10. Reaction scheme illustrating the steps leading to the formation of nanoparticles in plasmas.

It should be noted that only limited attention has been paid to the possibility of the technological use of plasma polymerized NPs. Nowadays, the situation is changing because the deposition of nanoparticles with controlled morphology offers an opportunity for preparing functionalized and nanostructured coatings [41,59,60,93].

2. Experimental

The current chapter aims to provide the reader with an overview and essential details of experimental and analytical techniques/equipment used throughout the study.

Most of the experimental work related to the preparation and characterization of the samples was carried out at the facilities of the Department of Macromolecular Physics, Charles University, Czech Republic. The study of segmental mobility of plasma polymerized AA NPs was done at Federal Institute for Materials Research and Testing (Bundesanstalt für Materialforschung und –prüfung), Berlin, Germany. The THz-Raman vibrational molecular spectroscopy results were obtained on ppAA NPs within frames of mutual collaboration with the Graduate School of Human Development and Environment, Kobe University, Japan. Finally, AFM-infrared nanospectroscopy measurements of ppPE islands on ppPEO film were performed at Bruker Nano lab, Santa Barbara, USA (a private agreement).

The chapter is organized as follows. Foremost, Section 2.1 outlines key operational parameters and construction features of nonthermal plasma-based deposition instruments as a Gas Aggregation Cluster Source and Plasma-Assisted Vapor Phase Deposition used to render the samples. Then, analytical methods and diagnostic equipment applied for in-depth sample characterization, materials, and analytical protocols are described within Section 2.2.

2.1. Plasma-based deposition methods

2.1.1. Gas Aggregation Cluster Source (GAS)

A gas aggregation technique having its principles explained in Section 1.2 was brought forward to synthesize ppAA NPs. For this purpose, a gas aggregation cluster source (GAS) was adapted and mounted vertically onto a separate PAVD deposition chamber (see 2.1.2 for more details). Both rotary and diffusion pumps were employed in the system to pump it down to base pressure of approximately 10^{-4} Pa.

The GAS (schematically depicted in Figure 11) consisted of a water-cooled stainless-steel cylinder vacuum chamber for plasma polymerization. The chamber was coupled with a conical lid and an orifice (Ø 1.2 mm) made of the same material. The

process of the GAS adaptation involved the replacement of conventional planar magnetron (Ø 2 inches) by a stainless steel electrode of the identical configuration.

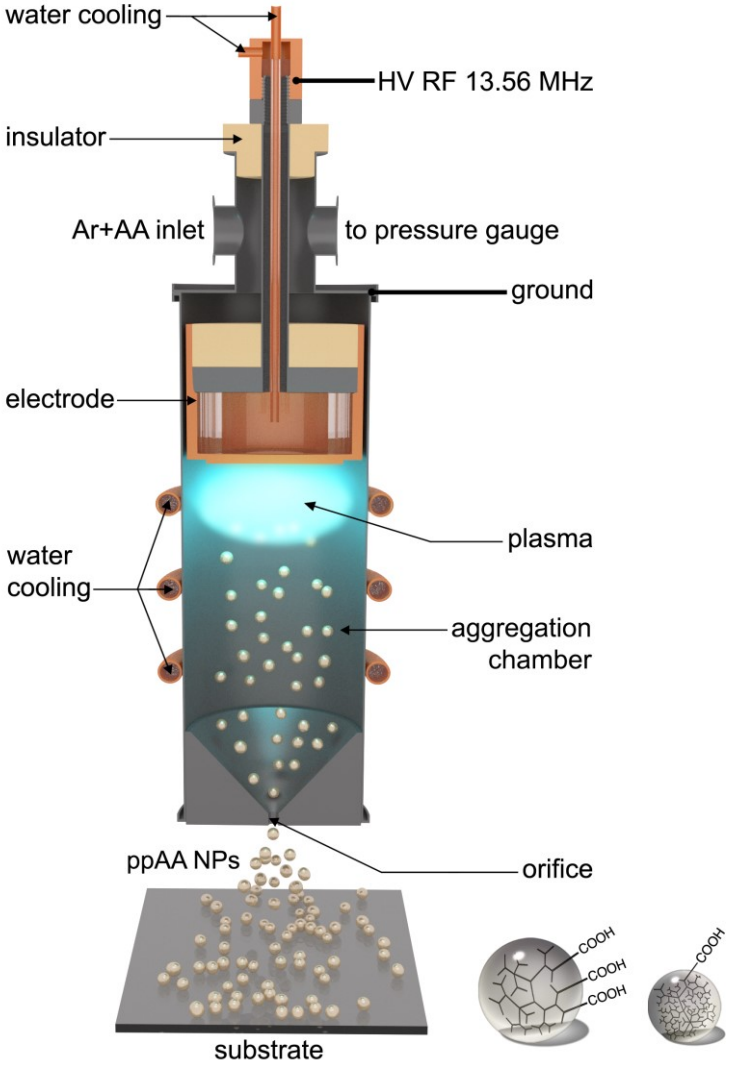

Figure 11. Principal scheme of the gas aggregation cluster source. The substrate is placed in a separate vacuum chamber, which is not shown here for simplicity.

A gas mixture of Ar playing the role of the buffer gas and vapors of monomer (AA) as a material source for plasma polymerization was used in the majority of the experiments having the constant Ar/AA ratio 30/70, unless it is specifically stated otherwise. To deliver the working gas mixture to the polymerization chamber, a combined gas feed system (GFS) was constructed. The buffer gas flow rate was adjusted by an automatic flow controller (MFC, MKS Instruments), while the flow rate of the monomer contained in a flask was controlled using a kelraz-sealed needle valve (Swagelok) installed in the GFS. After the system was evacuated, 11 sccm of Ar

and ~ 4.7 sccm of AA were introduced into the polymerization chamber to create 100 Pa overall pressure inside the GAS.

An RF power supply (Cesar Dressler, Advanced Energy Industries, Inc., 13.56 MHz) was operated both in continuous wave (CW) and pulsed mode to maintain the plasma. When operating in pulsed mode, two important discharge parameters should be taken into account. First, a duty cycle, typically used to describe the fraction of the pulse period when the plasma is on:

$$Duty\ Cycle = \frac{t_{on}}{(t_{on} + t_{off})} \quad (2)$$

where t_{on} and t_{off} correspond to the duration of the periods when the discharge is on and off, respectively. The second crucial parameter is known as the average power, delivered to the plasma, and can be calculated as follows:

$$P_{av} = P_{peak} \cdot Duty\ Cycle \quad (3)$$

here, P_{peak} refers to the plasma power achieved throughout the t_{on} period.

Once formed, the NPs are dragged by the Ar flow through the orifice to the separate deposition chamber. The NPs usually form a beam directed towards the substrate-holder placed at the axis of the orifice. More details regarding the silicon wafers and the liquid monomer used throughout the study can be found in section 2.2.5 of this chapter.

2.1.2. Plasma-Assisted Vapor Phase Deposition (PAVD)

Thin films of plasma polymerized PE and PEO were prepared by Plasma-Assisted Vapor Phase Deposition (PAVD) in a separate stainless steel vacuum chamber. The chamber was rigged with an electrically heated pair of crucibles, containing poly(ethylene oxide) and poly(ethylene) as polymer precursors, and an RF planar magnetron (Ø 3.18 inches) with a graphite target. Both crucibles were axially aligned with the magnetron located 4 cm below them. The scheme of the setup is depicted in Figure 12.

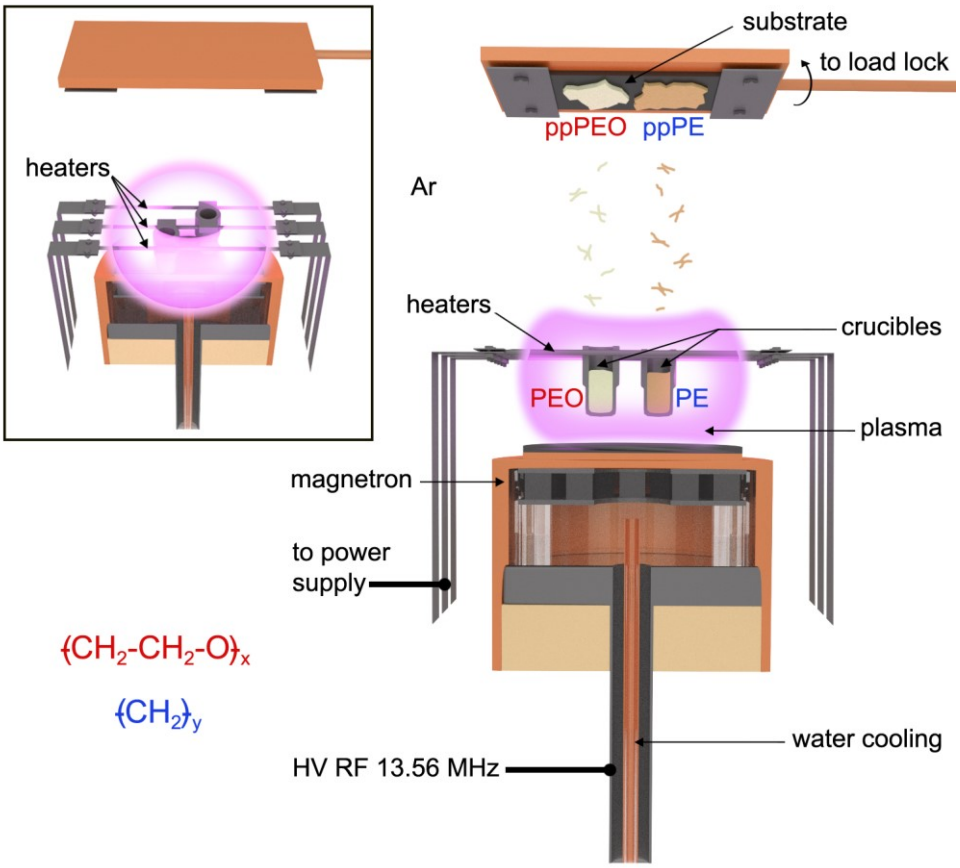

Figure 12. Principal scheme of the PAVD setup.

The magnetron was utilized to ignite and maintain the nonthermal plasma in the vicinity of the pair of crucibles. The RF power supply (Dressler Caesar, Advanced Energy Industries, Inc., 13.56 MHz) was operated in the CW mode to deliver 5 W of power to the electrode via an automatic matching unit (MFJ-962D). To control the deposition rates of ppPE or ppPEO films, a moveable Quartz Crystal Microbalance (QCM) was mounted 10 cm above the crucibles. An additional automatic flow controller (MFC, MKS Instruments) was connected to the deposition chamber to control Ar flow rate independently from the GAS described in 2.1.1.

The system was pre-pumped to the base pressure with rotary and diffusion pumps. Then 5 sccm of Ar was fed to the PAVD chamber to maintain a constant pressure of 1 Pa. The Si substrates resided in a separate vacuum loadlock attached transversally to the deposition chamber to ensure that the substrates can be inserted in the working position and retracted back when required.

2.1.3. GAS/PAVD system deposition protocols

There were two main deposition protocols employed in the experimental work. The first protocol was applied to combine the GAS source and PAVD for the rendering of the ppAANPs/ppPEO nanocomposites. The plasma was switched on, and the crucible with PEO underwent heating to the working temperature of 280 °C, measured by the thermocouple. The system was left running for 15 minutes to reach a stable value of the ppPEO deposition rate (8 nm/min). The substrates were then introduced 10 cm above the crucible, and the deposition of the 50 nm ppPEO film was performed.

After the deposition, the substrates were extracted back to the loadlock and the synthesis of ppAA NPs by the GAS source was initiated. To ensure a constant coverage, the deposition rate of the ppAA NPs was tuned to be stable at 25 μm^{-2}min as was recalculated from SEM analysis of the preliminary test samples set. Afterwards, the specimens with the ppPEO layer were reintroduced into the deposition chamber so that the ppPEO film faced the NP beam. After the deposition of the NPs, the samples were moved back to the load-lock. Finally, the PAVD procedure was initiated again in order to form a 3-nm thick capping layer of ppPEO over the ppAA NPs similarly to how the bottom ppPEO layer was produced.

The second protocol was applied for the sequential deposition of ppPE nanoislands over ppPEO thin films. Here, the discharge was ignited using the magnetron after the PEO-containing crucible had been heated to maintain the constant deposition rate of 20 Hz/min as witnessed by the QCM frequency shift. Subsequently, the substrates were placed above the crucible with PEO precursor, and the deposition of the ppPEO film proceeded. The deposition time was varied within the range from 3 to 20 min to produce thinner or thicker PEO coatings. After the deposition, the substrates were extracted from the chamber, and the heaters of the crucible with PEO were switched off. Sufficient time was allocated to cool down the PEO crucible until a drop to zero in the QCM readings.

In order to grow ppPE islands on the ppPEO coating, the PAVD of PE precursor was brought into use. A completely identical procedure was carried out so that the deposition rate of ppPE was set to 20 Hz/min, the substrates were placed into the working position, the ppPE nano-island deposition was performed, and the samples were extracted from the deposition chamber via the load-lock.

2.2. Sample diagnostics methods

2.2.1. Microscopic techniques

Atomic Force Microscopy

Atomic Force Microscopy (AFM) was chosen as a primary analytical tool to study the morphology of the specimen due to its high surface sensitivity and three-dimensional nature of the AFM images. The latter implies that detailed information regarding the surface fine structure can be extracted and later on used to derive statistical parameters commonly employed in practice for the surface characterization. Moreover, a set of scaling exponents can be calculated based on the statistical data to reveal an overall behavior of the surface of interest over time.

The AFM belongs to the family of scanning probe microscopy (SPM) techniques and has its main operating principle based on the interaction between the tip and the surface with a plethora of forces involved (van der Waals force, mechanical contact force, capillary forces, etc.). This results in the bending of the flexible cantilever, serving as a base for the tip, which is monitored, recorded, and then processed in a specific way that depends on particular AFM operating mode. More details on these modes, as well as data processing methods, can be found in [94].

The measurements on the samples were performed using the atomic force microscope (Ntegra Prima, NT-MDT) in an amplitude modulation intermittent contact mode under an ambient atmosphere. Supersharp silicon probes (SHR150, Nano&More, spring constant k = 5 N/m, resonant frequency 150 kHz, tip radius better than 1 nm) were employed for the measurements with the resolution of 256 × 256 data points. The cantilevers were run at 70% of the free oscillation amplitude damped to mitigate the deformation caused by force from the AFM tip and to ensure a reliable tip/sample contact. Image post-processing was done by using the Image Analysis software (NT-MDT, build 3.5.0.9990), including the subtraction of first-order polynomials from the raw data to remove the surface tilt and the analysis of resulting images.

A box-counting method as implemented in the Fractal Analysis plugin of the ImageJ software (build 1.52p) was employed for the calculation of the fractal dimensions of the poly(ethylene) nano-islands. First of all, at least 30 standalone

islands were identified for either sample. Then, the fractal dimension was obtained for each island. Finally, the mean value with standard deviation was calculated based on the data from the previous step.

In addition to a routine of the AFM sampling, in situ monitoring of the samples while in contact with a liquid phase was implemented using an atomic force microscope equipped with a fluid cell described within the following sub-section.

Fluid Cell Atomic Force Microscopy

Application of a Fluid Cell Atomic Force Microscopy (FC-AFM) technique allowed to study the stability of ppAA NPs in water as well as the adsorption kinetics of the lysozyme (LSZ) molecules to the ppAANPs/ppPEO nanocomposite surface.

The sample was placed onto a specimen holder at the AFM (Multimode 8, Bruker) head, and then, an air-tight glass fluid cell with 8 mm diameter O-ring was put on top of the sample. For more detailed information about this setup, please, refer to [95]. The ScanAssist (PeakForce Tapping) AFM operation mode was applied to enable direct force control at low forces to protect the tip/sample from mutual damaging. Super sharp SCANASYST-FLUID+ silicon probes (Bruker) with a nominal tip radius of 2 nm and nominal spring constant k = 0.7 N/m with a resolution of 386×386 points were employed in the measurements.

Initial images were recorded at the ambient atmosphere to stabilize the position of the tip on the sample surface and narrow its drift. Then, the cell was filled either with deionized water (18.2 MΩ·cm at 25 °C), PBS solution without Lysozyme (LSZ) or the protein solution, and a series of images were acquired at identical locations. Processing and analysis of the obtained AFM images (the ppAA NPs diameter evaluation) were carried out using the Nanoscope and Gwyddion (build 2.54) software, respectively.

Both classical and fluid cell AFMs offer a nanoscale spatial resolution but lack of chemical information about the sample. In the following section 2.2.2 devoted to Spectroscopic technique, it will be demonstrated how AFM-infrared nanospectroscopy, a cutting-edge analytical method accommodating advantages of two parent instrumental techniques (infrared spectroscopy (IR) and SPM), can be

applied to characterize the chemical composition of the ppPE/ppPEO nanocomposites surface at the nanometer scale.

Scanning Electron Microscopy

In addition to the AFM, scanning electron microscopy (SEM) was employed for the analysis of the ppAA NPs shape and amount for the calculation of the NP size distribution, flux (i.e., the number of NPs deposited per unit area per time), and mass flux. Unlike the AFM operating with a physical tip or classical optical microscope (OM) illuminating the sample with visible light, scanning electron microscope utilizes an electron beam generated by an electron gun (for example, the one that is based on field electron emission) as the «probe» to study the topography of a sample. Electrons have a wavelength that is about 10^5 times shorter than that of the light, which results in a significant improvement of instrument resolution.

Two SEM instruments were employed (Charles University, Prague, Czech Republic): Tescan Mira III that uses an in-beam secondary electrons detector mounted in the objective lens and Jeol JSM-7200F equipped with a high brightness Schottky field-emission (T-FE) electron gun, an In-Lens SchottkyPlus^{TM} technology-based electron optics and hybrid objective lens. All the measurements were carried out either in the TTL (through-the-lens) or classical SEM mode with the acceleration voltage set to 5 kV. No additional metallization was applied towards the samples. The ImageJ software (build 1.52p) was used for the ppAA NPs size evaluation from the acquired SEM images.

2.2.2. Spectroscopic techniques

X-ray Photoelectron Spectroscopy

Elemental analysis of the ppAA NPs, PE and ppPEO matrices and plasma polymer composites was performed by the x-ray photoelectron spectroscopy (XPS). XPS is based upon the photoelectric effect, i. e. emission of the electrons during the light-matter interaction, yet availing itself of the soft X-rays with photon energies of up to 10 keV in the form of the monochromated beam to be used instead of the visible

light. In most solids, these photons have penetration depth confined to 1–10 μm. However, the escape depth of photoelectrons is confined to the top 10 nm as predetermined by the inelastic mean free path, which implies excellent surface sensitivity of XPS.

By interacting with the atoms localized at the subsurface level, irradiating photons cause tightly bound core level electrons or more weakly bound valence electrons (or molecular orbitals) with specific kinetic energies to escape into a vacuum. Such electrons are then filtered by the energy analyzer letting only electrons with specific energy, commonly referred to as a "pass" energy, to get through and reach the detector. Typically, hemispherical analyzer (HAS) configuration is implemented in a majority of modern instruments. The data provide a spectrum of the electron intensity (number of electrons reaching the detector) as a function of their energy.

The kinetic energy of photoelectrons is interrelated to the binding energy that is unique for each element, thus enabling identification of elements the specimen is composed of and, with the relative sensitivity factors applied, the determination of their relative atomic concentrations. Moreover, the development of magnetic lenses significantly enhancing photoelectron collection made it capable of elemental imaging/mapping (i.e., obtaining spatially resolved spectra) by taking advantage of fine focus crystal monochromators or electron-optical aperture [96].

The measurements were conducted employing two instruments at hand. The first is a custom-built XPS spectrometer available at the Department of Macromolecular Physics with Al Kα X-ray source (1486.6 eV, Specs, Berlin, Germany) and HSA (Phoibos 100, Specs). Wide spectra were recorded for binding energies within the range of 0 – 1100 eV having pass energy and energy step values set to 40 eV and 0.5 eV, respectively. High-resolution C 1s and O 1s spectra were acquired with 10 eV pass energy, 0.05 eV energy step, and 10 repetitions. In both cases, the dwell time was fixed to 100 ms. The second XPS instrument (AXIS Supra, Kratos Analytical, Manchester, UK) equipped with monochromated Al Kα X-ray source and HSA was accessed within frames of cooperation with the Institute of Physics, Academy of Sciences of Czech Republic. The analysis was performed on a deliberately chosen area of 700 × 300 μm^2 of the specimen. The pass energy was set to 80 eV during the acquisition of wide spectra, while high-resolution spectra were recorded with 10 eV of the pass energy. Other parameters (energy step, dwell time)

were set to have similar values to the ones described above to be able to compare obtained data.

Acquired spectra were then referenced to the peak at 285.0 eV associated with the aliphatic carbon species. Primarily, for the chemical analysis of polymeric entities, a linear background was chosen during the fitting of high-resolution C 1s signal, unless specifically stated otherwise. The data post-processing and quantitative analysis were conducted in Casa XPS (Casa Software, Ltd.) and ESCApe (Kratos Analytical, Ltd.) software. Usage of the Gaussian-Lorentzian (70/30) algorithm yielded the best peak fits and, therefore, was applied in general to all the spectra quantification.

Fourier-Transform Infrared Spectroscopy

Fourier-Transform Infrared Spectroscopy (FTIR) is an advantageous analytical technique to study molecular bonds related to specific functional groups. FTIR relies on the selective absorption of electromagnetic radiation by molecules with the following vibration of specific sets of chemical bonds within the molecule. FTIR spectrometer irradiates a specimen with mid-IR and measures the ratio between the intensities of the incident and reflected light. The most common realization of FTIR instruments takes advantage of the Michelson interferometer, which ensures simultaneous measurements across all wavelength, and Fast Fourier Transformation (FFT) mathematical algorithm [97] to convert the resulting interferogram into a classical spectrum of intensity versus a wavenumber.

Each molecule may have several distinct modes to be activated by IR radiation due to its structural features; thus, it produces a so-called unique fingerprint, which can be used for the molecule identification if a data library is available. Otherwise, FTIR provides complementary information and is used in conjunction with other techniques.

A spectrometer (Bruker Equinox 55) was operated in a reflectance-absorbance mode to perform the measurements. The specimens were deposited onto Si wafers precoated with a thin layer of gold. The primary region of interest for organic samples is located within 4000 – 400 cm^{-1}. For each measurement, 400 scans with a spectral resolution set to 4 cm^{-1} were recorded. The spectra were afterwards processed using the OPUS (BRUKER Optics) software.

Atomic Force Microscopy-based Infrared Spectroscopy

A cutting-edge Atomic Force Microscope Infrared Spectroscopy (AFM-IR) [98] was employed to obtain images showing the distribution of chemical species across the sample at the nanoscale level. It combines the chemical analysis capabilities of IR spectroscopy with AFM spatial resolution that exceeds the conventional diffraction limit.

In its current form, AFM-IR couples pulsed IR tunable laser to a region of a specimen in the proximity of an atomic force microscope probe tip (Figure 13) and monitors the response of the latter with a four-quadrat detector. The absorption of IR photons results in rapid heating of the local region and, hence, to its almost instantaneous thermal expansion. The expansion creates a transient force impulse which induces the cantilever into oscillatory motion. In most cases, the oscillation amplitude of the AFM cantilever is directly proportional to the amount of IR light absorbed, and this, in turn, is directly proportional to the absorption coefficient. Therefore, it is possible to obtain IR absorption spectra from that signal by measuring the cantilever response amplitude as a function of the laser wavelength (or wavenumber).

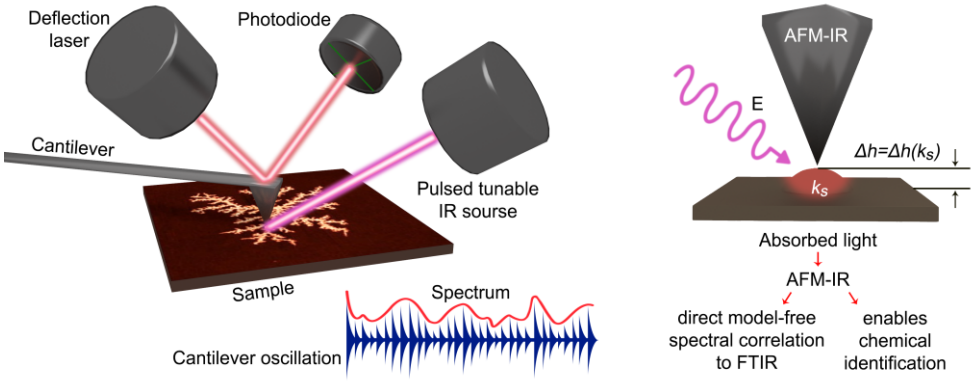

Figure 13. The scheme of AFM-IR operation principle.

Pulse duration and repetition rate are adjusted via the proper choice of the laser. For example, a Nd:YAG-based Optical Parametric Oscillator can produce pulses of a low repetition rate (~ 1 kHz), which causes a transient decaying oscillation of the cantilever (e.g., a ring-down). On the contrary, photothermal AFM-IR with tunable quantum cascade based laser (QCL) is able to synchronize (modulate) pulse repetition

rate to match the cantilever resonance frequency, leading to continuous excitation of the cantilever and, therefore, to sensitivity improvements.

There are two common approaches in AFM-IR measurements. In the first, the oscillation amplitude of the cantilever is measured as a function of incoming radiation wavelength. The second approach is based on measuring the oscillation amplitude of the cantilever as a function of the sample position and is employed for chemical imaging. Typically, either the peak-to-peak oscillation amplitude of the cantilever or the oscillation amplitude at any specific oscillatory mode (eigenmode) of the cantilever is measured.

The cantilever oscillates over multiple eigenmodes because of the short time of the force applied to it. These eigenmodes of the AFM cantilever, when operated in contact mode, correspond to contact resonances. The contact resonance frequency is extracted using FFT and can provide information about the mechanical properties (for instance, stiffness) of the sample. It is also worth pointing out that other properties of the sample related to material such as thermal expansion coefficient, heat capacity, density, and Young's modulus are of no effect on the AFM-IR signal and remain constant at a specific point the measurements are conducted on.

A commercially available nanoIR2-FS system (Bruker Nano Surfaces Division) equipped with a QCL laser to cover the mid-IR spectral region (1850 - 950 cm^{-1}) was used for the analysis of the local chemical composition of the PE nano-islands on PEO. All the measurements were performed in the AFM intermittent contact mode with testing the cantilever response against either IR light wavenumber or the position. Multiple IR spectra were recorded with constant 2 cm^{-1} spectral resolution, smoothed using the Savitzky-Golay algorithm with 3-side points, and then averaged.

THz-Raman Spectroscopy

Many physical phenomena such as vibrational and rotational transitions in molecules, collective vibrational and torsional modes in condensed matter, low-energy excitation, and carrier dynamics in electronic materials fall within THz region (0.1 – 20 THz) of the electromagnetic spectrum and, thus, can be probed with it. With a set of mirrors, THz radiation is collimated and focused onto the specimen; then it is recollimated again with a focus towards the detector. When the radiation passes

through the sample, it becomes attenuated and delayed as determined by the sample permittivity.

Conventional THz spectroscopy, commonly referred to as THz time-domain spectroscopy (THz-TDS), uses Fourier transformation (FT) to extract information about the sample permittivity from the time-domain sample and reference waveforms. This coherent detection in the time domain is advantageous because it allows for the measurement of the temporal evolution of the electrical field, not only its intensity. FT enables direct measurement of the contribution of the amplitude and the phase of the spectral components to the signal. They are used to determine the absorption coefficient and the refractive index of the sample without Kramers-Kronig analysis. A more detailed overview of the THz spectroscopy-branch methods can be found at [99].

Relatively new THz-Raman spectroscopy (also known as low-frequency Raman, ultra-low-frequency Raman, or Rayleigh-wing spectroscopy) is a complementary technique to THz-TDS to study the interactions in materials driven by low-frequencies, in particular, cooperative segmental mobility vibrational modes such as rotation of intermolecular segments in polymers.

Raman spectroscopy itself is very similar to IR spectroscopy (and to THz-TDS) as these techniques measure a series of absorption bands of vibrational/rotational transitions at different frequencies. The THz-Raman (THz-RS) spectral region covers both Stokes and anti-Stokes signals from approximately 5 cm^{-1} to 200 cm^{-1} carrying structural information about molecule or crystal lattice. This region also reveals a new "structural fingerprint" which is complementary to the traditional chemical Raman fingerprint, therefore allowing to analyze both molecular structure and chemical composition simultaneously. A Raman spectrometer measures the shifts in the frequency of the inelastically-scattered radiation from a single reference frequency of the source. These shifts correspond to the inter- and intra-molecular vibrations as well as material phonon modes [100].

THz-Raman spectra of plasma polymerized poly(acrylic acid) nanoparticles deposited onto intrinsic Si substrates were recorded using Ondax SureBlock XLF series THz-RS system equipped with excitation laser tuned to 830 nm. A 180° back-scattering geometry was implemented, and the spectra were obtained within a wavenumber range of 1590 - 20 cm^{-1}, resolution of 3.5 cm^{-1}, and 20 scan repetitions. The raw data were then smoothed by a Savitzky-Golay algorithm. For all the samples, the spectra were acquired for several different temperatures ranging from room

temperature to 150 °C with a step of 10 °C. The temperature of the sample on Si substrate was controlled by a temperature controller unit (T95-HS, Linkam Scientific Instruments Ltd., UK). Before each measurement, the sample was maintained at a given temperature for 5 min to allow for thermal equilibration.

Specific Heat Spectroscopy

Specific Heat Spectroscopy (SHS) in the configuration of Differential AC-chip Calorimetry was brought into use to study the glass transition phenomena in ppAA NPs. Calorimetry is extremely useful when it comes to studying the thermophysical properties, in particular, molecular mobility-related effects such as glass transition temperature, enthalpy relaxation, etc. Generally, two approaches are employed in calorimetric investigations: scan at variable/constant rate of temperature change and periodic temperature oscillations. The latter refers to calorimetry with alternating current temperature modulation (AC-calorimetry). In the AC-calorimetry, oscillatory heat flux is applied to a specimen, and its heat capacity is determined afterwards from the consequent sample temperature oscillations. A demand for further extension of AC-calorimetry capabilities towards the measurements on ultra-thin films led to the development of integrated calorimetric sensors (ICS, shown on Figure 14) and the establishment of a differential approach i.e. simultaneous measurements on two pairs of sensors (reference/reference and reference/specimen) to exclude the heat losses associated with the sensors themselves.

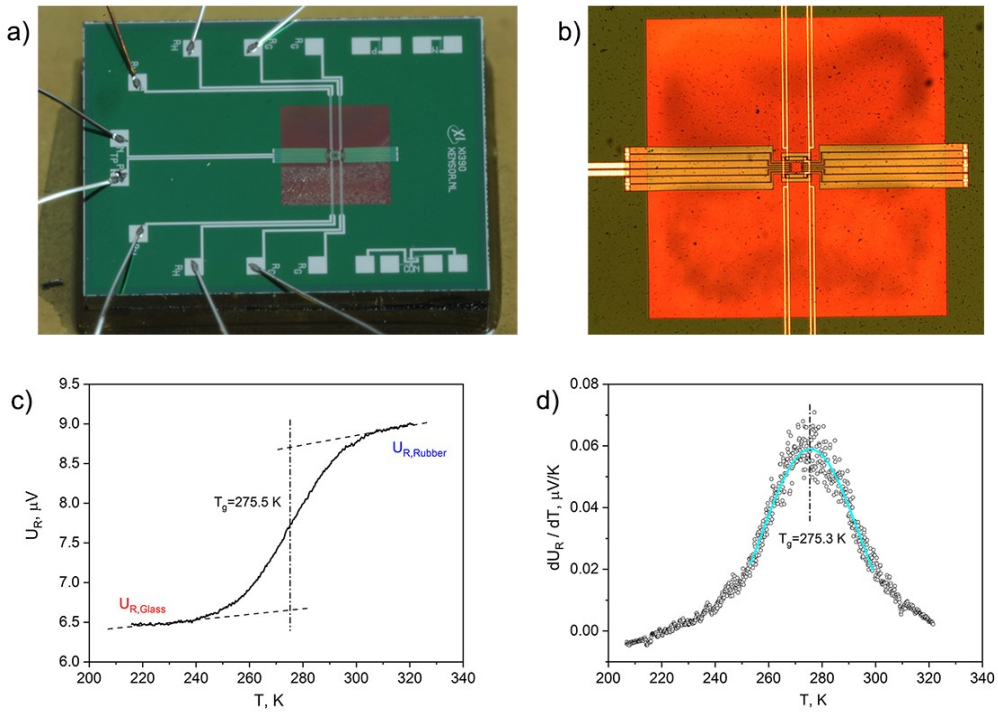

Figure 14. Photos of a) the sensor XEN 39390 chip and b) close up of the chip center (reproduced with permission of Xensor Integration BV [101]); c) real part and d) the first derivative of the real part of the complex differential voltage versus temperature of a thin ppPEO film deposited with RF power input of 30 W. The measuring frequency was 320 Hz. The solid line in part (d) corresponds to a fit of a Gaussian to the data (adapted from [102]).

In common realization, the specimen is deposited over the ICS in such a way that only a limited area is heated (point heat source). Both reference and sample-containing sensors are then installed into a thermostat. The heaters are driven by an alternating current of frequency $\omega/2$ produced by a generator integrated in a lock-in amplifier. Passing AC causes oscillations of heat power of frequency ω (angular frequency), which in turn invokes local temperature oscillations of the specimen. They are detected by a chip thermopile as the complex differential voltages (ΔU) between sample/reference and reference/reference sensor pairs.

The ΔU consists of a real (differential voltage U_R) and imaginary (phase shift Φ) components and is considered as a measure of the material complex heat capacity C_S. For thin films approximation, C_S can be expressed by the formula:

$$C_S = \frac{i\omega \bar{C}^2 (\Delta U - \Delta U_0)}{SP_0} \qquad (4)$$

where $\omega = 2\pi f$ (here, f is a frequency) and $i = (-1)^{1/2} \cdot \bar{C} \equiv C_0 + G/(i\omega)$. Here, ΔU is the complex differential thermopile signal from an empty (reference) sensor and the sample; ΔU_0 represents complex differential voltage measured across two empty reference sensors; S is related to a thermopile sensitivity; P_0 is a heating power applied to the sample. The term $\bar{C}$ introduces the heat capacity of the empty sensor and includes two terms: C_0, which is a sensor heat capacity, and $G/(i\omega)$ that takes into account heat losses through the surrounding atmosphere.

The temperature dependence of U_R is represented by a stepwise function (Figure 9c) having its value at half of the step-height defined as the dynamic glass transition temperature. The T_g can also be determined by locating the maximum of the imaginary part of ΔU function with respect to the temperature. Typically, a first derivative of the U_R function is taken to obtain a function with the maximum that can be fitted by a Gaussian curve afterwards. The dynamic T_g corresponds to the position of the function maximum. More details regarding the technical implementation and the adopted approach to the T_g determination can be found in Reference [103] and Reference [104], respectively.

For all the experiments, commercially available ICSs (XEN 39390, Xensor Integration, NI) equipped with an array of thermopiles and heaters protected by a 1 μm-thick SiO_2 layer were used as measurement cells. Monolayers of the ppAA NPs were deposited over the entire ICS area. Upon considerations of plasma polymer thermal stability originating from our preliminary experiments with ppPEO thin films, the maximal temperature was set to 300 K, which is found causing no eminent deviations of calorimetric curves. The measurements were performed by scanning the temperature with a constant cooling/heating rate of 2.0 K/min and a fixed modulation frequency of 160 Hz of the temperature having a sinusoidal profile. The modulation amplitude was kept below 0.5 K (heating power is approximately 25 μW) to maintain a linear regime [103]. The calibration was performed according to the protocol described in Reference [102].

Spectroscopic Ellipsometry

Spectroscopic Ellipsometry (SE) is a non-destructive and very surface sensitive analytical technique that uses polarized light as a probe to study the optical properties of the specimen. In general, the ultraviolet/visible region of the electromagnetic

spectrum is a primary one for SE measurements, yet the optical range covered by SE extends towards the near-IR region as well.

A SE instrument transmits light from the source (typically a Xe/Hg-Xe arc lamp) through a polarizer to set its polarization state, then focuses this polarized light onto a sample. The light is reflected from the specimen towards another polarizer (commonly referred to as analyzer) and passes through it to reach the detector. The spectrometer detects a change of polarization state of light upon transmission or reflection from the sample.

The change of polarization for different wavelengths carries information about the sample, in particular, its optical constants, roughness, thickness, composition, and structure, etc. These quantities, however, cannot be obtained directly from the raw data and are extracted by comparison of experimentally measured data with the results of a model based on the structure the specimen is assumed to have. For a more detailed description of the SE measurements and modelling see [105].

In the current work, the capping layer of plasma polymerized poly(ethylene oxide) thickness was measured by ex-situ SE (Woollam M-2000DI) with a variable incidence angle (55 – 75º) and spectral range of 300 – 1,100 nm. The optical parameters were then fitted by a single-layer B-spline Kramers-Kronig consistent model using a CompleteEASE software (J.A. Woollam).

2.2.3. Electrochemistry

Streaming potential measurements

Electrokinetic potential (also known as zeta (ζ) potential) is an important parameter of solid-liquid interface routinely applied for characterization of the functionality of biomedical polymers, electrokinetic transport of particles in colloids or blood cells, and for the design of microfluidic devices [106].

Zeta (ζ) potential is established on the surface of any material when it is brought in contact with a liquid medium, and carries information about the net charge present at the interface. The process of ζ-potential formation refers to an interaction between functional groups on the sample surface and the surrounding medium, which contributes to the development of surface charge. The latter attracts the oppositely charged ions arranging them in a so-called electrochemical double layer (EDL).

The EDL consists of a stationary layer (ions within this area are completely immobilized by strong electrostatic interaction) and a diffusive one (here, ions are able to move across the layer) separated by a so-called shear plane. This plane defines which part of the EDL contributes to the material overall net charge; thus, the potential at the shear plane can be defined as the ζ-potential.

The streaming potential is one of the four measurement techniques used to study interfacial electrochemical phenomena. In terms of instrumental implementation, the streaming potential is measured on two samples transversally mounted on holders to form a capillary flow channel. The flow of the liquid (usually electrolytes, such as NaCl or KCl solutions) drags the ions from EDL away from their equilibrium positions, causing the charge separation that gives rise to a streaming current and streaming potential. The fundamental equation that relates the streaming potential and the streaming current to the ζ-potential is known as the Helmholtz-Smoluchowski equation [107].

Zeta potential measurements on nanophase separated plasma polymer composite coating based on ppAA NPs and ppPEO thin film were conducted using a SurPASS Instrument (Anton Paar, Austria). The samples were mounted inside a chemical cell with an adjustable gap and brought in contact with the electrolyte solution (1mM KCl water solution). For each measurement, a pair of samples were fixed on two transversal holders with a gap between them of 100 μm. Initially, the specimens were processed at a constant pH = 7. Then, they were titrated by 0.5M HCl water solution from pH = 7 to 2.5 and subsequently by 0.5M NaOH water solution from pH = 6.4 to 11.0. For each of the titrations, fresh pairs of the samples were installed and measured twice with a relative error of 5%.

2.2.4. Chromatographic methods

Gel permeation chromatography

Gel permeation chromatography (GPC) refers to a specific type of Size Exclusion Chromatography (SEC), yet the two terms are very similar and often used interchangeably as GPC is the most common type of SEC. The GPC can be described as an analytical technique that is used to characterize macromolecules, including

polymers and proteins, providing information about their molecular weight, intrinsic viscosity, and hydrodynamic radius. These traits often affect the physical properties of the material and/or the behavior of the particular compound and are of great interest.

A chromatography provides a foundation for the GPC and points to a set of techniques involving the separation of mixtures. Typically, chromatography involves passing a mixture carried by a mobile phase through a porous stationary phase, which separates constituents of the mixture based on differential partitioning between the mobile and stationary phases.

The separation process operates based on the diffusion (or permeation) of the analyte molecules in and out of the pores on the gel particles (often referred to as beads) representing the stationary phase. More specifically, a stagnant liquid present inside the pores of beads is employed in the GPC as the stationary phase, while a flowing solvent as the mobile phase. The latter can, therefore, flow between the particles and also in and out of the pores. The separation mechanism is based on the size of the polymer molecules present in the solution. Large molecular fragments spent the least amount of time inside the porous gel particles and usually are carried past by the mobile phase. The intermedia sized entities can diffuse into the larger, but not smaller pores in the beads as they pass by, thus, occupying some, but not all of the available volume at the stationary phase. The smallest molecular constituents can easily diffuse in and out of the pores and penetrate all the way in, and thus they require the most time to elute.

A typical instrument consists of a pump pushing the solvent through the system, an injection port to introduce the sample of interest into a column, the column where the stationary phase is located, one or several detectors to detect the components as they leave the column, and a PC to control the different parts of the instrument and calculate and display the results. The most common detectors used in the GPC are the following: a refractive index detector (RID), a photodiode array detector (UV-VIS), a light scattering detector (LSD) and a viscometer. Each of those can respond to the sample concentration (RID, UV-VIS), to the light absorption (UV-VIS), to the sample molecular weight (LSD) and the intrinsic viscosity (viscometer). In the current work, a classical RID was employed, so only its basics of operation will be covered.

The principle behind the RID is that light travels differently through different media. The refractive detector works by using a light source to project a beam of light through a flow cell composed of two separate volumes. A pure solvent is supplied by

the pump to one of them, while the other is filled with a mixture of the solvent and the sample. The light will then refract at the interface of these two volumes and become reflected by a mirror back towards a set of photodiodes. These are under different potentials. Depending on whether the sample refracts the light more or less than the solvent, the light will move onto a positive or negative diode, producing either a positive or negative signal. The amplitude of this signal corresponds (I_i, see Equation 5) to the concentration of the sample (C_i) as well as the material refractive index increment (dn/dc) that is used to correlate a refractive index response to the sample concentration. The dn/dc is a unique value for a given sample and mobile phase pairing.

$$I_i = \frac{K}{n_0} \cdot \frac{dn}{dc} \cdot C_i \tag{5}$$

Herein, K – instrument constant, dn/dc – refractive index increment, C – concentration (g/L), and n_0 – refractive index of a solvent.

In the result of the components being detected, the sample elution behavior is characterized and displayed as a chromatogram.

The PL-GPC 220 (Agilent, Inc.), an integrated GPC/SEC system equipped with a PL-220DRI refractive index detector, was employed to evaluate the molar mass distribution of PEO and PE. For this purpose, thick deposits of both materials were obtained. The PEO sample was dissolved in tetrahydrofuran and then analyzed at room temperature using a columns Labio, 600 × 7.5 mm gel column with the porosity of 500 Å (Polymer Laboratories). The PE specimen was dissolved at 160 °C in 1, 2, 4-trichlorobenzene mixed with 0.025 wt. % of a Santonox R antioxidant to prevent oxidative degradation. The measurements on PE were carried out at 160 °C as well, using columns 3 × PL gel 10 µm MIXED-B, 300 × 7.5 mm coupled with a guard column PL gel 10 µm MIXED-B, 50 × 7.5 mm.

2.2.5. Biomolecule adsorption tests

Lysozyme is an antimicrobial enzyme related to the innate immune system that acquires a positive charge when in contact with a biological media. In the current study, we exploited this phenomenon to ensure a spatially-resolved biomolecule attachment. To check the performance of ppAANPs/ppPEO nanocomposites, we employed the following protocol in the study. First, lysozyme (LSZ) was dissolved in

the phosphate-buffered saline (PBS) to obtain a concentration of 50 μg/ml. The nanocomposite samples deposited on Si wafers were submerged into the well-plates with 2 ml of LSZ/BSA solution. To remove physically adsorbed protein molecules, the samples were rinsed twice by de-ionized water after 20 min incubation period and were dried under the ambient air. The X-ray photoelectron spectroscopy analysis was performed to quantify the nitrogen concentration, which was considered to be an indicator of protein binding on the surface. *In situ* protein adhesion was studied by FC-AFM method allowing direct injection of LSZ/PBS solution into a fluid cell of the AFM under its operation.

2.2.6. Materials

Mechanically and chemically polished silicon wafers (OnSemi, ⟨100⟩, one-side polished, 1×1 cm, 525 μm thick) were used as substrates unless stated otherwise. Granular poly(ethylene oxide) (PEO, Sigma-Aldrich, M_n=2.5·10^3 g/mol) and poly(ethylene) (PE, Sigma-Aldrich, Inc., M_n=20·10^3 g/mol) and a liquid monomer Acrylic Acid (AA, Sigma-Aldrich, Inc., purity 99%) were used as primary precursors for the synthesis of ppPEO or ppPE coatings as well as ppAA NPs. Lysozyme (LSZ, Sigma-Aldrich, Inc.) and phosphate-buffered saline (PBS, Sigma-Aldrich, Inc.) were chosen for the nanocomposite biomolecule adhesion tests as a model protein and a biological medium, respectively.

3. Results and Discussion

3.1. Preparation of ppAA NPs using a gas aggregation cluster source

3.1.1. Ex situ characterization of ppAA NPs

For the synthesis of ppAA NPs to be used in bioresponsive plasma polymer nanocomposites, the GAS system was deployed in the configuration previously described in Section 2.1.1. At the early stages of experiments, the discharge was operated in continuous wave mode and at a constant average power of 40 W, yet with different partial pressures of the monomer. The ppAA NPs formed inside the polymerization chamber were then dragged out by the gas flow via the exiting orifice in the form of a beam to reach the Si substrates, where the particles were collected. Figure 15a shows the SEM images of the ppAA NPs prepared at different AA partial pressures. The SEM images were then used to calculate the NP mean size, flux (i.e., the number of NPs deposited per unit area per second), and the mass flux.

The mass flux j_m was estimated by calculating the volume of each NP observed within the field of view of the SEM images, followed by summing all the volumes and calculating the deposited mass per unit area per time with an assumption that the density of the plasma polymer is approximately equal to 1 g/cm^3 (a typical value for plasma polymers) [108,109]:

$$j_m = \frac{\rho \sum(\frac{\pi}{6})d^3}{A_{SEM}t} \quad (6)$$

Here, ρ is the density of the plasma polymer, d is the NP diameter, A_{SEM} is the area of the SEM view field, and t is the deposition time.

The ppAA NPs are characterized by spherical shape with no fine structure present, regardless of the monomer feed rate. On the other hand, the NP mean size, flux and mass flux were found to increase with the increase of the AA partial pressure (Figure 15b). The observed trend corresponds to a well-known concept of energy dose-driven plasma polymerization where power delivered to the plasma (also referred to as energy dose) is related to the flow rate (rate of supplying) of the fresh monomer molecules [2].

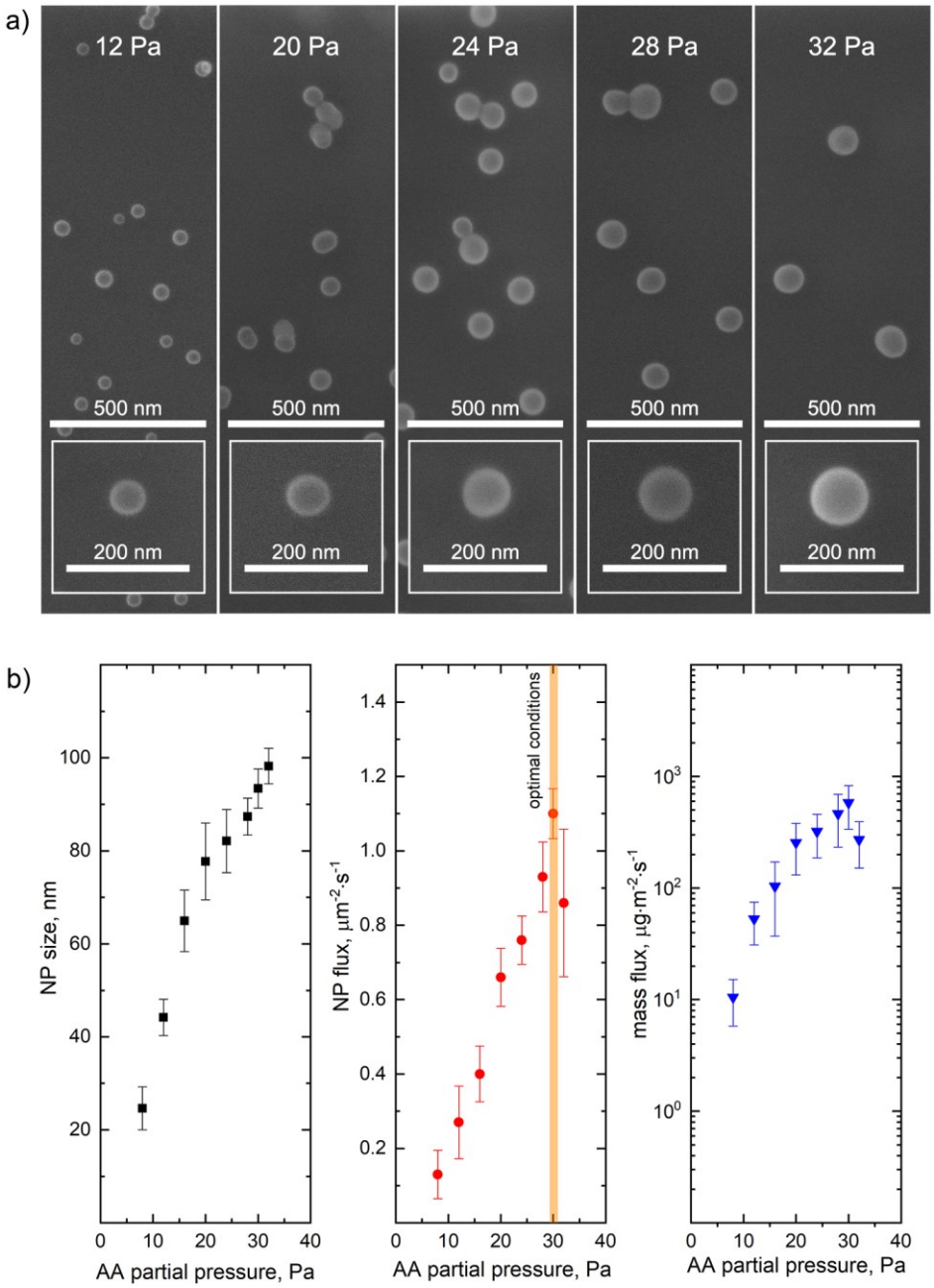

Figure 15. a) SEM images of the prepared NPs at different partial pressures of the AA and constant power of 40 W (CW mode), the overall pressure in polymerization chamber is 100 Pa and deposition time is 30 s; b) dependence of the NP size, flux and mass flux on the AA partial pressure.

Following this concept, under highly nonequilibrium conditions of the glow discharge, the electrons are primarily responsible for the power consumption. Being extremely mobile in comparison with Ar ions or neutral atoms, they are able to acquire high energy of a few eV, which is sufficient to cleave the chemical bonds in organic molecules and to produce radical species. The elevated pressure of tens to a hundred

Pa in the polymerization chamber forces radicals to recombine preferentially in the gas phase with the formation of nuclei. Once formed, the nuclei start to grow either by coagulation or by attachment of other radicals/intact monomer molecules (via the opening of the polymerizable vinyl bond) to become NPs.

At the lower monomer feed, the energy supplied per monomer molecule is high enough to cause its severe fragmentation, thus leading to a higher radical concentration (nucleation centers). This results in the growth of a larger number of NPs, yet with a small mean size. The high monomer supply, vice versa, makes the fragmentation process less effective, thus leading to the formation of a smaller number of NPs of larger mean size. A series of the reproducibility tests indicated that the monomer feed depends on the temperature fluctuations. When the monomer flow rate is set to minimal values, these thermal fluctuations may result in unstable monomer volatilization and, therefore, in oscillations of ppAA NPs deposition rate.

To decouple the plasma polymerization process from the undesired effect of ambient temperature fluctuations, an alternative approach to the realization of monomer-rich and monomer-deficient regimes was chosen via control of the discharge power. The optimal composition of the gas mixture was fixed at 30 Pa of AA and 70 Pa of Ar, and a number of the experiments were carried out using both continuous wave and pulsed mode. The pulsing parameters in the latter case were kept constant, the duty cycle was 50% and a pulse period was 50 μs (pulse repetition frequency PRF 20 kHz). Only the average power (P_{av}) delivered to the plasma was varied from 25 W to 80 W.

Figure 16 shows the high-resolution AFM images of the NPs prepared at different average power in the CW mode. To the detection limit of the AFM probe, the NP surface has a featureless, smooth morphology. This is consistent with many other types of plasma polymer NPs [18,60,110–113], although it should be noted that particular plasma polymer NPs were previously reported to have developed surface topography [24,83,114–120].

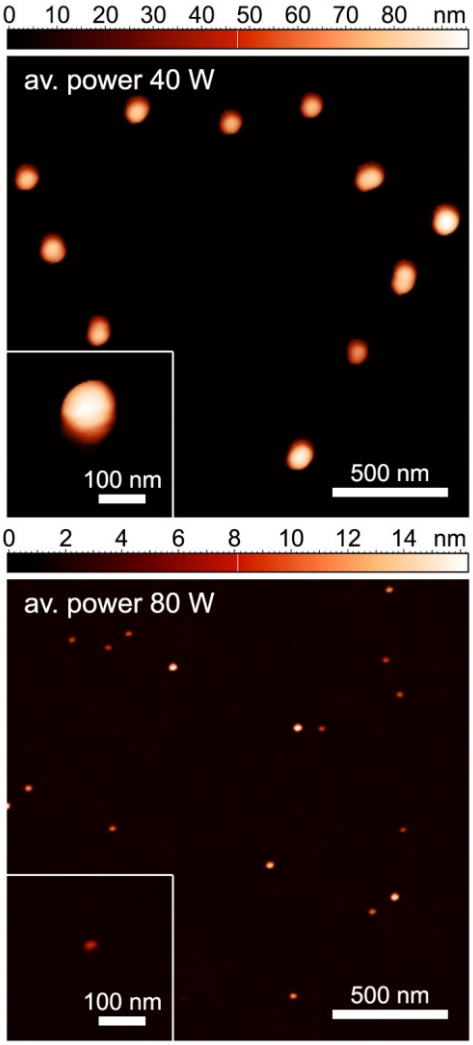

Figure 16. AFM images of ppAA NPs deposited at different average powers (40 W and 80 W) in the CW mode. The partial pressures of AA and Ar are 30 Pa and 70 Pa, respectively. The deposition time is 30 s.

The ppAA NPs were also a subject of the SEM analysis in order to study the peculiarities of the ppAA NP deposition (Figure 17). A decrease of the NP diameter with power and a corresponding increase in the NPs flux was distinctly observed for both the continuous wave and pulsed modes. Remarkably, when the plasma was operated in pulsed mode, the NP agglomeration was detected, while continuously run discharge produced only single NPs at similar conditions. This indicates that electrostatic interaction between the NPs may occur in the plasma. Apparently, more complex mechanisms are responsible for the plasma polymerization of AA under conditions of low-temperature non-equilibrium RF plasma. Both the agglomeration

phenomenon and hypothetical chemical mechanisms of ppAA NPs formation and growth will be discussed in detail within Section 3.1.2.

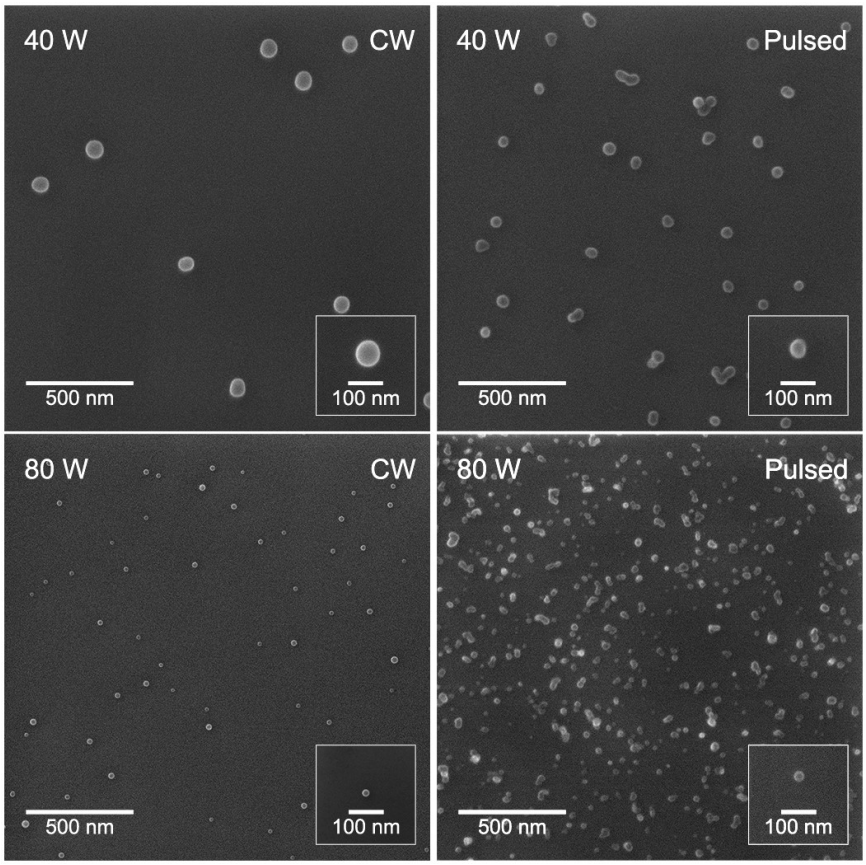

Figure 17. SEM images of ppAA NPs deposited at different average powers of 40 W and 80 W in CW and pulsed modes (duty cycle is 50% and the pulse period is 50 μs). The partial pressures of AA and Ar are 30 Pa and 70 Pa, respectively. The deposition time is 30 s.

Based on SEM observations, the size, flux and mass flux of ppAA NPs descent with a ramp of average power, yet this occurs to a different extent for the two discharge operation regimes in consideration. In the case of the CW mode, the NP mean size quickly changes from 94 nm to 15 nm, whereas in the pulsed mode, the mean size value difference at minimal and maximal powers is less profound (Figure 18). Overall, the energy dose concept holds valid for the variation of average power, which allows for fine-tuning of the NP size and flux with no contribution from the monomer feed rate fluctuations.

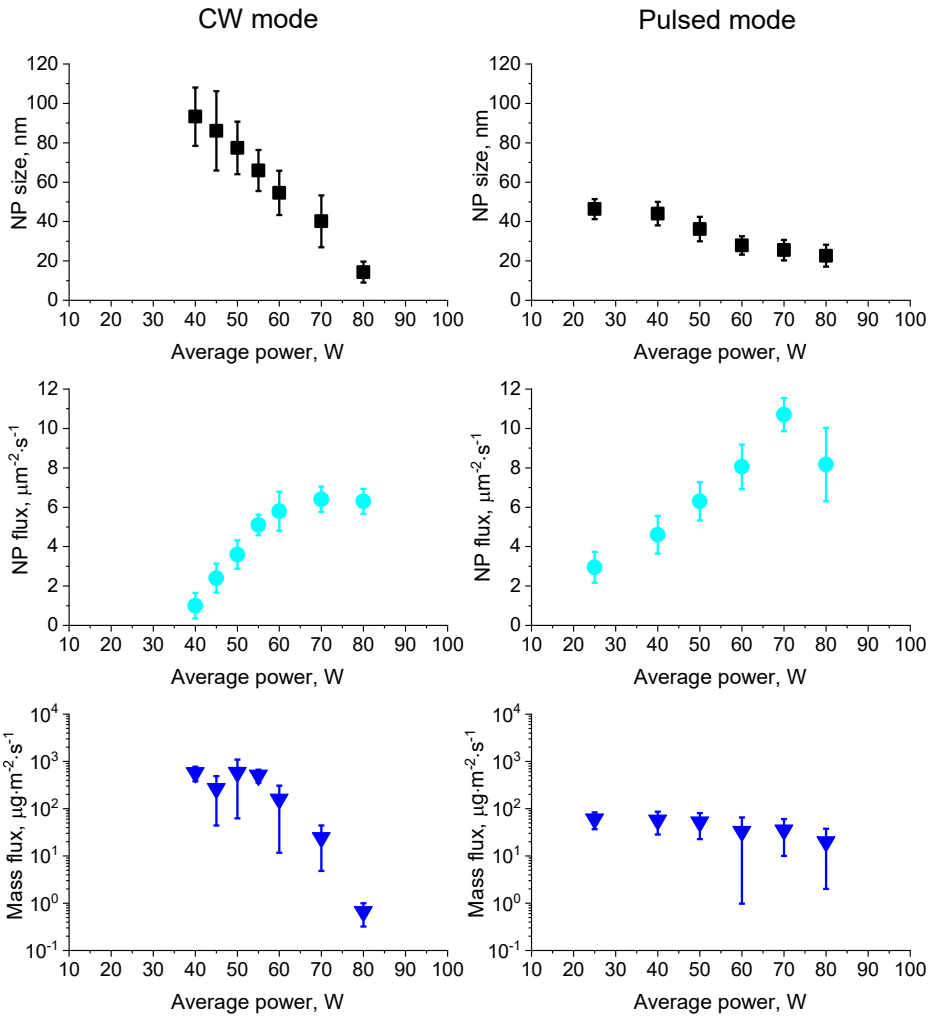

Figure 18. Dependence of the NP diameter, flux and mass flux on the average power in CW and pulsed modes (duty cycle is 50% and pulse period is 50 μs). The partial pressures of AA and Ar are 30 Pa and 70 Pa, respectively.

The ppAA NPs were also a subject of XPS analysis to get the insight into their chemical composition, in particular the presence of carboxyl entities required for biomolecule immobilization. The dependence of the NP elemental content on the average power was studied for both CW and pulsed modes. Table 1 summarizes the data on the elemental composition of ppAA NPs. In general, the overall retention of oxygen in ppAA NPs is worse when compared to conventional polyacrylic acid (40 at. %). Regardless of the mode, the content of oxygen in ppAA NPs reaches its maximum when the plasma is operated in the energy-deficient regime, then gradually decreases with increasing of average power.

Average power, W	CW mode		Pulsed mode	
	C, at. %	O, at. %	C, at. %	O, at. %
25	-	-	70	30
40	81	19	75	24
50	81	19	80	20
60	82	18	85	15
70	84	16	87	13
80	86	14	88	11

Table 1. Elemental content of the ppAA NPs, as witnessed by XPS.

The core level C 1s high-resolution XPS spectra (Figure 19) acquired on the ppAA NPs resemble those obtained for ppAA thin films [69,78,121,122]. Typically, the plasma polymer is represented by a hydrocarbon network (C-C/C-H bonds) bearing a multitude of chemical functionalities, which can be classified in terms of the XPS analysis into three groups of atomic carbon bound with oxygen with one, two, or three bonds. Thus, the C 1s photoelectron band in all the spectra can be deconvoluted into four components: a peak centered at 285.0±0.1 eV, which is usually associated with the C-C and C-H bonds; a peak located at 286.5±0.1 eV, corresponding to the C-OH and C-O-C functional groups; a peak at 288±0.1 eV, assigned to the C=O and O-C-O bonds; and a peak at 289.1±0.1 eV, which is commonly attributed either to the carboxyl or ester (-COOR) groups and combination thereof. In a recent study on ppAA thin films, the contribution of the acidic form has been distinguished from the esters by performing chemical derivatization [69]. The results confirmed that the contribution of the carboxyl groups corresponds to more than 90% of the component at 289.1±0.1 eV. Thus, it can be expected that this peak primarily originates from the carboxyl groups incorporated in the ppAA NPs.

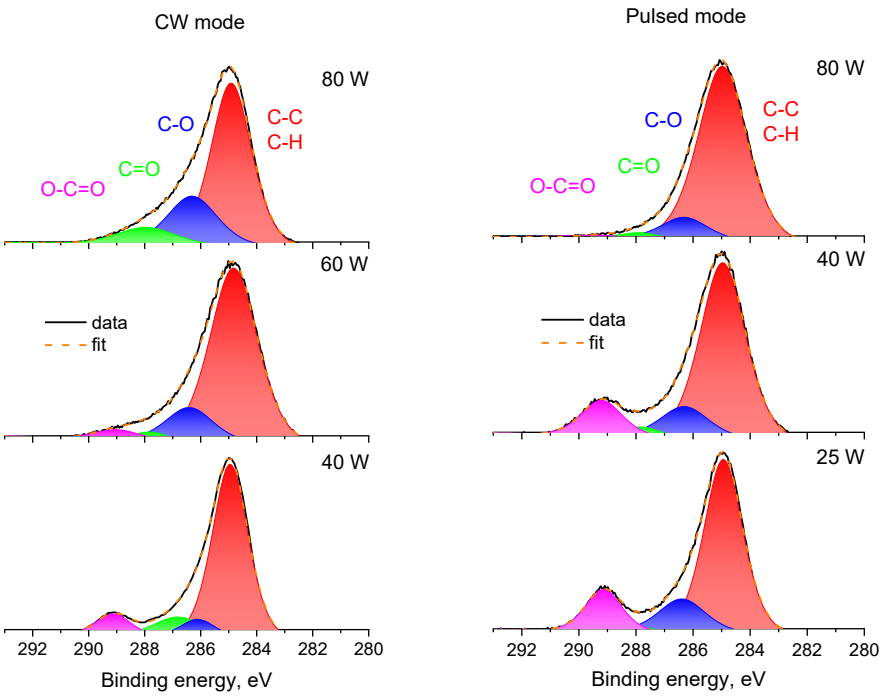

Figure 19. Core-level C 1s high resolution XPS spectra recorded on ppAA NPs deposited at different powers in CW and pulsed modes.

Figure 20 shows the changes of the O-C=O group concentration with average power. The retention of these groups at the constant level cannot be maintained as the P_{av} grows up because of the enhanced fragmentation of the precursor molecules. As a result, plasma polymer NPs are formed with a high degree of cross-linking in the polymer framework, in close analogy with the structure of plasma polymerized AA thin films [123–125]. Remarkably, the chemical composition of ppAA NPs stays comparable at the same average power values, regardless of the operation mode the NPs were prepared at. The maximal value of 16 at. % for the O-C=O groups was observed for the NPs polymerized at the lowest power, which suggests that only half of the concentration of carboxyls in conventional polyacrylic acid (33 at. % of C) becomes incorporated into the plasma polymer.

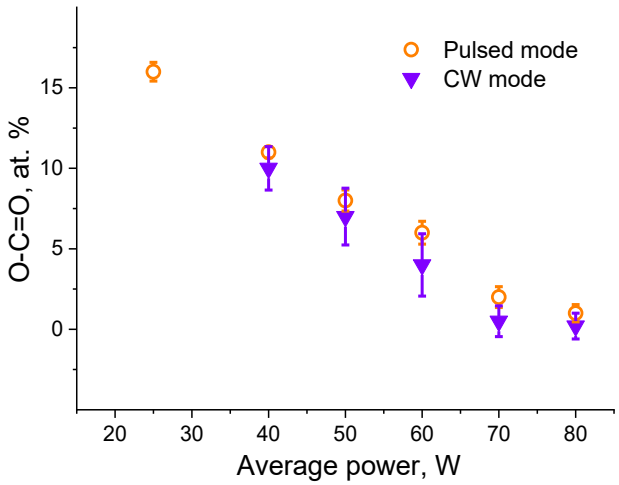

Figure 20. The dependence of the retention of the O-C=O functional groups on the average power.

In addition to XPS, the ppAA NPs deposited at different operational conditions were analyzed by FTIR (Figure 21). The NPs are characterized by the presence of the bands associated with the OH groups (2500-3500 cm^{-1}), hydrocarbons (2900-3000 cm^{-1}), the C=O-based species (1700 cm^{-1}), as well as the certain bands belonging to the aliphatic CH and C-O stretching vibrations coupled with O-H in-plane bending. The less intensive bands can be found at smaller wavenumbers in the spectra. This region is accessed via the THz-Raman spectroscopy in Section 3.1.3 as a part of the investigation of thermally-driven genesis of the NP structure. The assignments of the FTIR bands are summarized in Table 2.

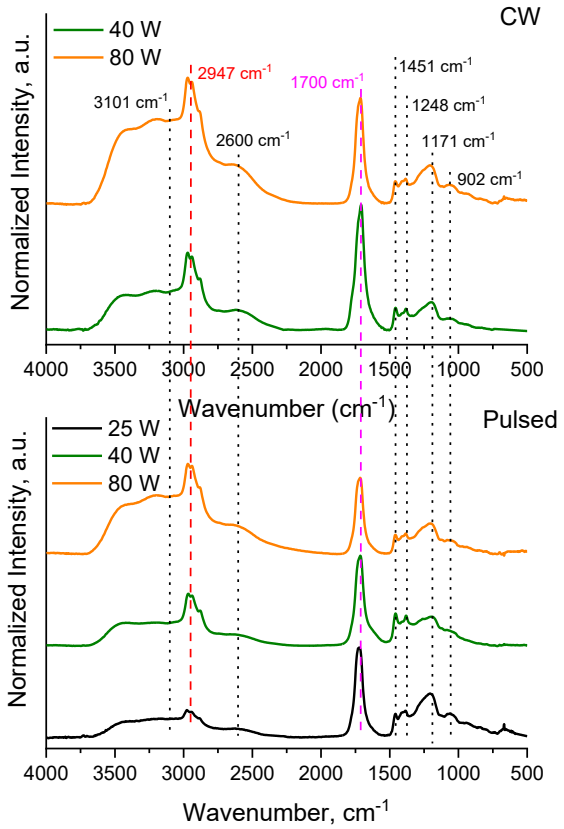

Figure 21. Normalized FTIR spectra for the ppAA NPs deposited at different powers in the CW and pulsed modes.

Wavenumber, cm^{-1}	Assignments [126–128]
3100 broad	O-H stretching
2947	CH_2 or CH stretching
1700-1730	C=O stretching
1451	CH_2 deformation
1248, 1178	C-O stretching coupled with O-H in-plane bending
1112	C-CH_2 stretching
902	O-H out-of-plane bending
804	CH_2 twisting and C-COOH stretching

Table 2. The assignments of the FTIR bands for ppAA NPs deposited at different powers in CW and pulsed modes.

The FTIR results are in close agreement with the XPS data, suggesting that the upswing of the power and, as a consequence, the average energy dose supplied per molecule, leads to the loss of the original monomer structure as reflected in the concentration of the carboxyl groups. The IR spectra of plasma polymers are difficult to be used for quantification; however, this trend can be readily accessed qualitatively by comparing the bands at 1710 cm^{-1} (stretching vibrations of the C=O-based groups, which in our case are assigned to carboxyls) and at 2947 cm^{-1} (stretching vibrations of hydrocarbons) [129,130]. At low power, the band of carboxyls dominates the spectra for both plasma operation modes, whereas it subsides at higher average power and becomes overrun by other functionalities as it is reflected, for example, by the C-H/O-H bands becoming supreme in the spectra with the rising power.

3.1.2. Physical and chemical mechanisms underlying the NP formation and growth

A complementary study of the NP size, flux and the mass flux was performed in dependence on the pulsing parameters to get the insight into the mechanism of the ppAA NPs nucleation and growth. The concentration of the carboxyl groups was studied as well. Here, a mechanistic approach was opted to describe the experimental findings and to compare them with those obtained for thin film deposition from the literature sources.

The AA/Ar gas mixture, average power and total pressure inside the polymerization chamber were set to their optimal values (30/70 Pa, 40 W and 100 Pa) found at previous experiments with plasma polymerization of AA. The experiments were carried out at different duty cycles. It is important to note that the power delivered to the discharge during the time on (the time when the plasma is on) is inversely proportional to the duty cycle due to the fixed average power value (Table 3). The average energy supplied per monomer molecule was calculated by equation:

$$E_{mean} = P_{on} V_m / F N_A \quad (7)$$

where P_{on} is the power delivered to the discharge during t_{on}, V_m is the molar volume of an ideal gas, F is the flow rate, N_A is the Avogadro constant.

Duty Cycle, % (PRF 20 kHz, P_{av} 40 W)	T, µs	t_{on}, µs	t_{off}, µs	P_{on}, W	E_{mean}, eV/mol.
100	-	-	-	40	36
80	50	40	10	50	45
70	50	35	15	57	51
60	50	30	20	67	60
50	50	25	25	80	72
40	50	20	30	100	90
32	50	16	34	125	112
PRF, kHz (DC 32%, P_{av} 25 W)					
30	33	11	22	78	70
20	50	16	34	78	70
10	100	32	68	78	70

Table 3. The parameters of pulsed plasma used for the synthesis of ppAA NPs.

The SEM images of the ppAA NPs deposited on Si substrates at different duty cycles, as well as the corresponding size histograms, are shown in Figure 22. Overall, the plasma polymerization of AA driven by continuously run plasma resulted in the formation of larger NPs with small flux, while discharge operated at pulsed mode yielded a larger amount of small NPs. This phenomenon is consistent with the enhancement of the monomer fragmentation due to the increase of average energy dose supplied to the monomer molecule E_{mean} caused by a ramp of P_{on} at a constant monomer feed rate (Table 3) [131]. Earlier, a similar effect was also observed for the plasma polymerization of heptadecafluorodecyl acrylate [18] and RF-plasma driven magnetron sputtering of nylon [83].

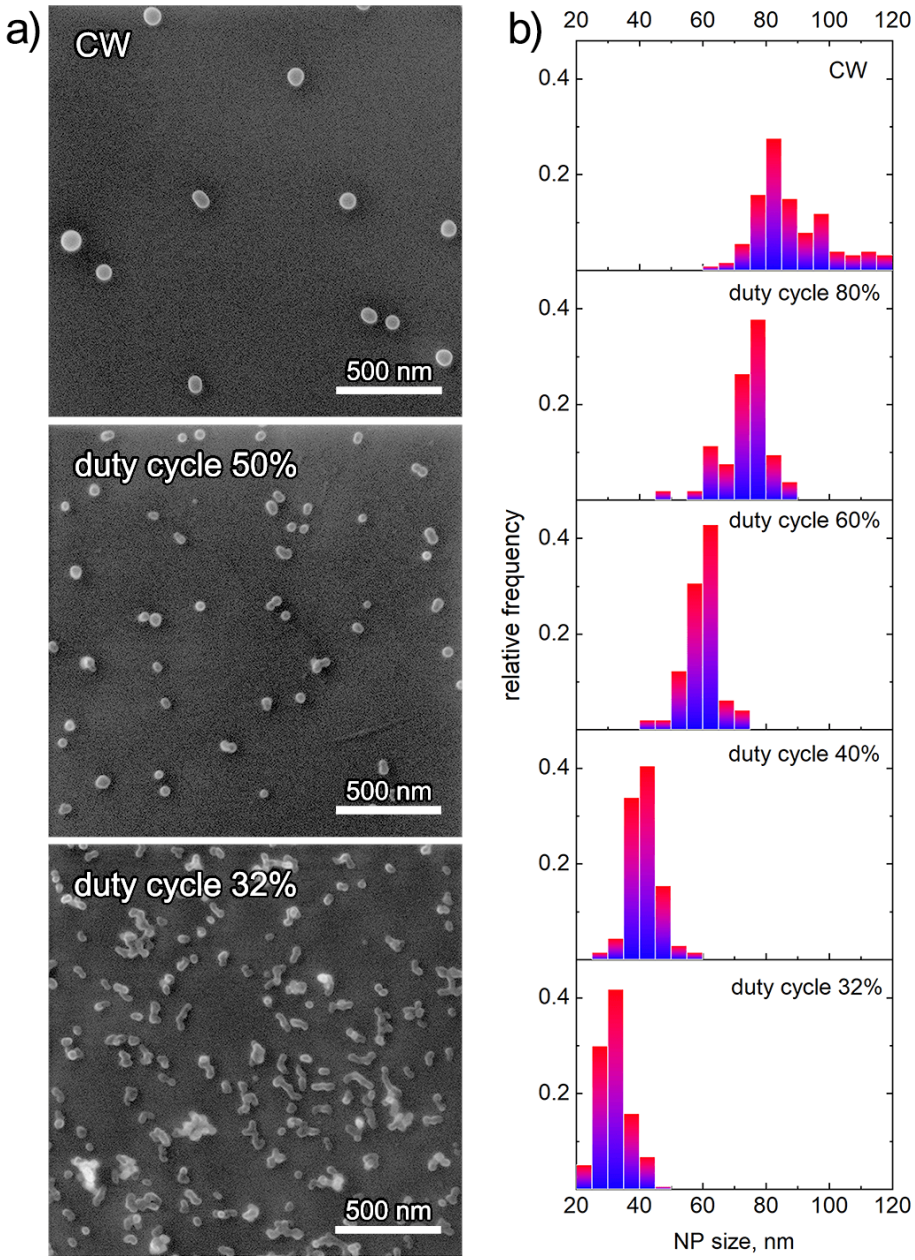

Figure 22. a) SEM images and b) normalized size histograms of ppAA NPs deposited in the pulsed plasma at different duty cycles. P_{av} 40 W, PRF 20 kHz, deposition time is 5 seconds. At small duty cycles, the NPs that constitute to agglomerates are treated as individual NPs.

Although the values of E_{mean} in Table 3 are overestimated because only a fraction of energy that is coupled to the discharge facilitates the monomer bond cleavage, they are worth comparing with the dissociation energy of all existing bonds in a molecule of AA, E_D = 43 eV [132]. Such comparison suggests that for the most of the experiments, the plasma polymerization process proceeds under highly energetic

conditions ($E_{mean} > E_D$), except for the CW mode (duty cycle = 100 %), where the $E_{mean} < E_D$, which implies that a certain amount of the monomer molecules remain intact.

When the discharge is operated in the pulsed mode, the intensive fragmentation of the monomer molecules occurs during the time on (monomer deficient regime). Under the constant monomer flow, this triggers the formation of a higher concentration of nucleation centers, such as radicals and ions. They are mainly responsible for the appearance of a high amount of the ppAA NPs of smaller size. The continuous plasma provides, on the contrary, a lower number of nucleation centers resulting in the opposite effect.

A more detailed analysis of the SEM images taken at different duty cycles also points to the coagulation of the NPs already observed at the early stages of the study (section 3.1.1). The coagulation is more probable to happen at smaller duty cycles (longer t_{off}) and results in the formation of larger agglomerates. To get a better insight into the NP morphology, which can point to the probable origins of the agglomeration, the AFM analysis on single NPs and the agglomerates was run using high aspect ratio cantilevers. High-resolution AFM images taken on the two samples prepared at different duty cycles are shown in Figure 23.

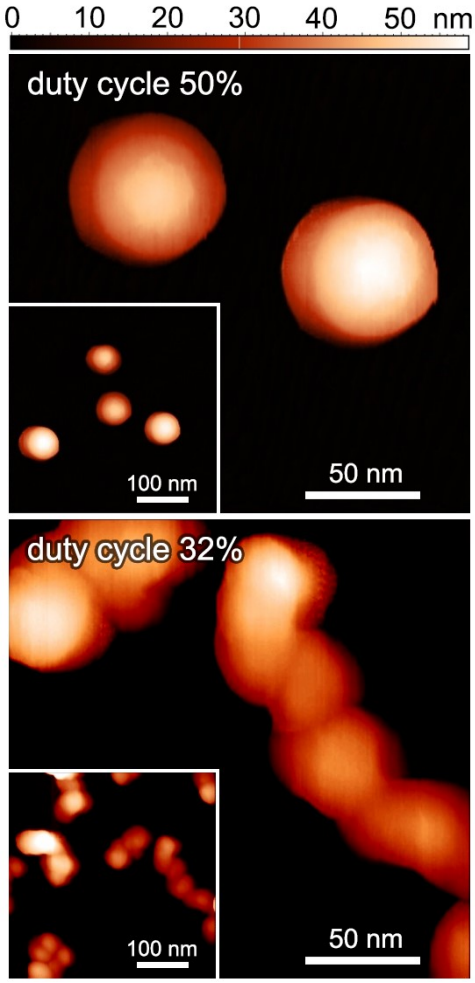

Figure 23. AFM images of ppAA NPs deposited at duty cycle of 50% and 32%. The average power is 40 W, PRF 20 kHz, deposition time is 5 seconds. The inset images show the same areas, though scanned at lower magnification.

Individual NPs produced at the duty cycle of 50% were found to have a spherical shape, which implies an isotropic nature of their growth and an absence of any preferential direction for incoming polymer-forming species. A high-resolution AFM probe here resolves a featureless and smooth structure of the NP surface at the limit of tip curvature radius and its thermal fluctuations. Therefore, the material arriving on the surface becomes redistributed as the NP grows, which can be seen as an opposite scenario to that of fractal structures with highly developed morphology formation when the sticking coefficient of incoming species either equals to 1 or is very close to it [45,133]. Despite the NP surface texture remaining unchanged as the duty cycle is reduced to 32%, the NPs become aggregated into larger agglomerates. The agglomeration evidences the existence of an additional mechanism at smaller duty cycles that bunches the NPs together.

At this stage, the two approaches were tested during the analysis of the NP flux and mean size. The first strategy was to treat all the NPs as individual entities, intentionally ignoring the fact that part of them (and in some cases nearly all of them) were constituting agglomerates. The second approach considered the agglomerates as individual NPs, but much bigger. The latter was calculated as the diameter of an imaginary spherical particle with a similar surface area occupied. The results for both methods are summarized in Figure 24.

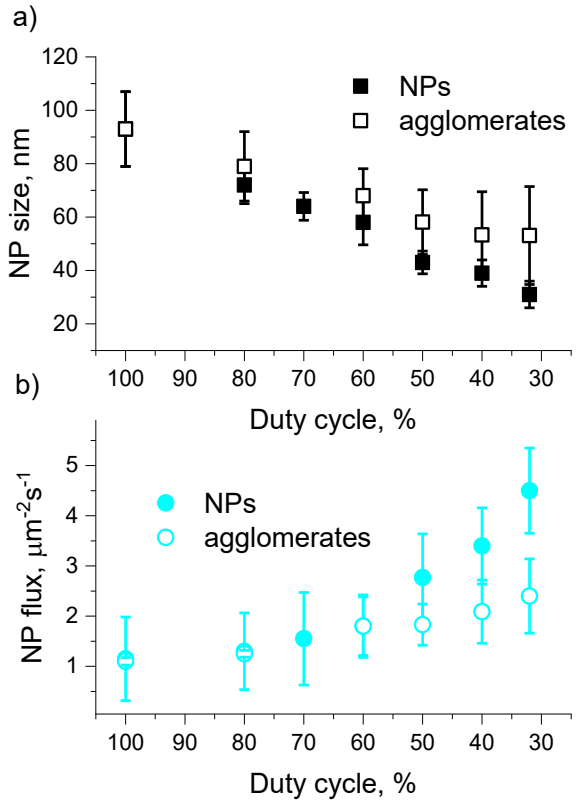

Figure 24. Dependence of the NP size and flux on the duty cycle; average power 40 W, PRF 20 kHz. Solid symbols correspond to the parameters calculated by treating all NPs separately. Open symbols correspond to the parameters calculated by taking into an account the agglomerates as bigger particles; the characteristic size of the agglomerate is taken as $= \sqrt{4A/\pi}$, where A is the area occupied by this agglomerate.

Both strategies employed in data processing produced similar trends. At constant average power, as the duty cycle is shortened, the NP size notably decreases

from 93±14 nm at the CW mode to 31±5 nm at 32% duty cycle when we consider agglomerates as a cluster of several separate NPs of various size. On the other hand, the particle flux varies inversely to the duty cycle. The changes were found to be less prominent when agglomerates are thought of as imaginary particles with specific "characteristic size".

Taking into consideration that the NP agglomeration prevails at low duty cycles, the phenomenon has electrostatic nature and can be related to the charging of the NPs during t_{on} and to the loss of the charge during t_{off}.

The residence time t_{res} of the NPs inside the polymerization chamber of GAS can be calculated with an assumption that the NPs travel along the chamber in a viscous regime with the drift velocity of the carrier gas mixture:

$$t_{res} = L/v \tag{8}$$

where L = 8 cm is the length of the aggregation chamber. The agglomeration of individual NPs is not taken into account.

The drift velocity of the gas mixture v is calculated as follows:

$$v = P_0 Q_0 / P A_{GAS} \tag{9}$$

The P_0 is the standard pressure, Q_0 is the gas mixture flow at the standard pressure, P is the total pressure inside the polymerization chamber of the GAS, A_{GAS} is the cross-sectional area of the polymerization chamber.

The timescale of plasma pulsing period T = 50 μs is extremely short when compared to the residence time (the time that the NPs spend in the polymerization chamber of GAS) t_{res} of 1 s, what implies that the NPs experience many plasma cycling events on their way along and out of the polymerization chamber. More specifically, the NPs are able to acquire a floating potential, which is negative with respect to the plasma potential. In a close analogy with the charge-driven agglomeration of NPs in solutions, negatively charged particles should then experience the Coulomb repulsion, which prevents them from coming in contact with each other, therefore, suppressing the agglomeration.

When operating in pulsed mode, the NP charge balance is determined by how fast the floating potential is built up during t_{on} and how fast it is lost during t_{off}. According to work [134] dealing with pulsed capacitively-coupled discharges operated at several Pa pressure in Ar and in AA gas mixture, electrons become lost within 150 μs from the beginning of t_{off}. Although large ions may survive at these conditions for

much longer times. Because of the higher pressure used in this thesis, the time scale of electron losses should be even shorter. For example, the Bohm velocity can be calculated for the mean electron energy by the following formula:

$$v_B = \sqrt{\frac{kT_e}{M_i}} \cong 10^4 \text{ m/s} \tag{10}$$

where kT_e = 1 eV measured in this type of the GAS [135], and M_i = 72 amu is the mass of acrylic acid molecular ion. If v_B is related to the characteristic size of the polymerization chamber (inner ∅ of 62 mm), then the characteristic time of several μs is obtained. The characteristic time determines the time scale required for the ions to become lost on the walls and for the plasma to collapse. Small duty cycles less than 60% (with the corresponding t_{on} less than 30 μs and t_{off} more than 20 μs as shown in Table 3), seemingly provide sufficient t_{off} period for the ppAA NPs to start losing accumulated charge, which then triggers the onset of their agglomeration. At larger duty cycles, t_{off} expires before the plasma completely collapses, and, in this case, the electrostatic repulsion between the NPs subdues the agglomeration. The principal scheme of this process is indicated in Figure 25.

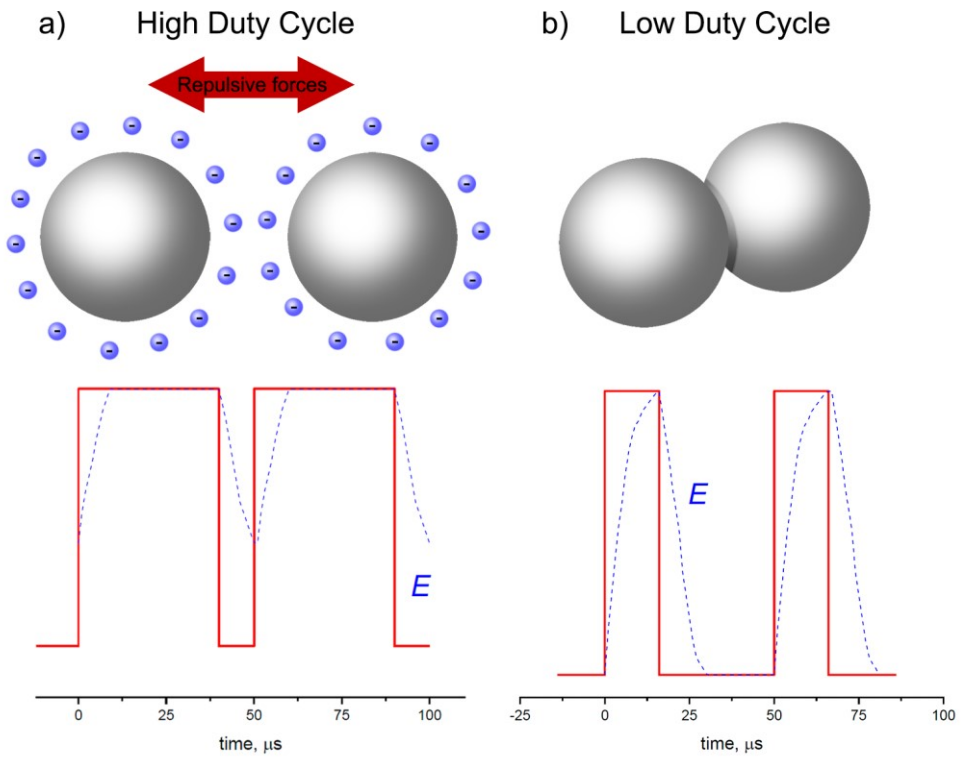

Figure 25. Schematic illustration of electrostatic interactions between the NPs and an imaginary time-resolved signal from the power supply at a) high and b) low duty cycles; *E* denotes the electric field.

To confirm the hypothesis, complementary experiments with constant average power and duty cycle but with various pulse repetition frequencies were carried out to provide direct control over t_{off} (Figure 26, Table 3). It is important to note that the plasma run at the average power of 40 W was not able to maintain the stable and reliable NP deposition rate and, therefore, it was set to 25 W as the most suitable for these experiments.

At PRF of 30 kHz (t_{off} equals to 22 μs), the agglomeration is just about to start. The deposit itself is represented by a mixture of both single NPs as well as their agglomerates; however, the individual NPs still prevail for these conditions. Reducing the PRF to 20 kHz prolongs t_{off} to 34 μs for the charge dissipation after the plasma collapse, which in turn increases the probability of the agglomeration. Finally, at PRF = 10 kHz with the longest t_{off} of 68 μs, an interconnected maze of the agglomerates is formed with a minimal contribution from individual NPs.

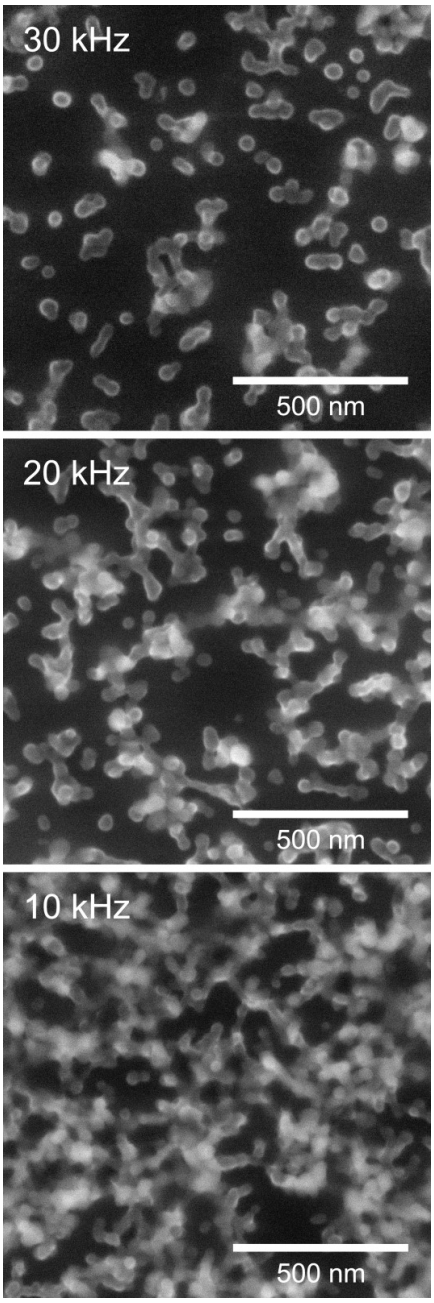

Figure 26. SEM images of ppAA NPs deposited on Si substrates in the pulsed mode at different PRF, P_{av} 25 W, duty cycle 32%, deposition time is 10 seconds.

The NP chemical composition was also subject to XPS analysis in dependence on the duty cycle to access the possible mechanism responsible for the ppAA NP formation. The spectra in Figure 27 demonstrate that the concentration of the O-C=O groups is inversely proportional to the duty cycle, although the difference is not large: the concentration of 9.0 at. % and 12.0 at. % is detected for the continuous and the pulsed modes with 32% of the duty cycle, respectively.

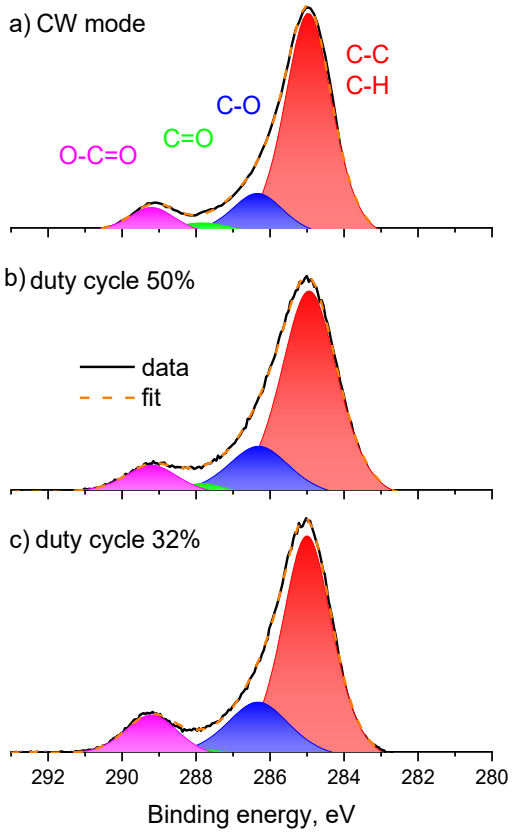

Figure 27. Core-level C 1s high-resolution XPS spectra recorded on the ppAA NPs prepared at a) CW mode, b) 50% duty cycle and c) 32% duty cycle. The average power and PRF are kept constant at 40 W and 20 kHz, respectively.

However, the concentration of the O-C=O groups versus duty cycle plotted for all conditions studied (Figure 28a) reveals two distinct regimes of NP formation with the imaginary border at the duty cycle of about 60%. In the region beyond that value, the increase of time off is accompanied by a growth of peak power. Such an increase results in the significant fragmentation of initial monomers as witnessed by the reduction of the O-C=O concentration to 4.0 at.%. Markedly, in the region of low duty cycles, the O-C=O concentration starts to increase, restores to 9.0 at.%. and reaches beyond it at the smallest duty cycle of 32%. Besides, the dependence of the NP mass flux on the duty cycle closely replicates the one for the O-C=O group concertation (Figure 28b). In close analogy with chemical composition changes discussed above, two distinct regimes were identified here as well. Overall, the efficiency of the NP

formation is either decreasing or increasing at high and low duty cycle regions, respectively.

Both these findings indicate that there exists a shift in the original mechanism responsible for the NP formation and that different plasma polymerization processes dominate this mechanism at the duty cycle of less than 60%.

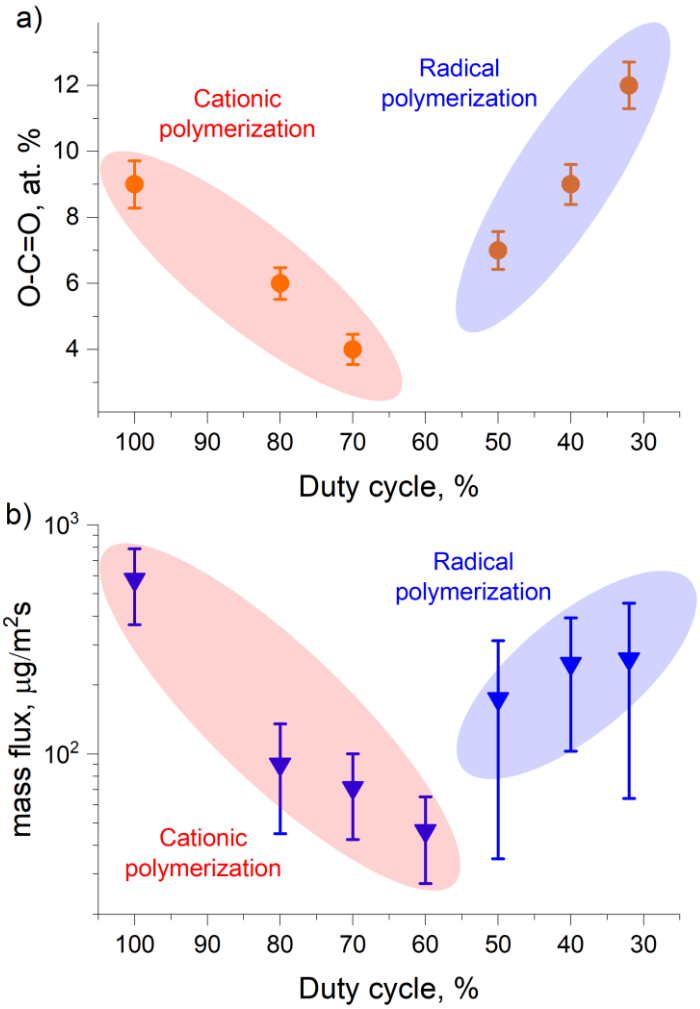

Figure 28. a) The concentration of the O-C=O functional groups detected by XPS; b) NP mass flux onto substrates in dependence on duty cycle. The average power is 40 W and PRF is 20 kHz.

In general, compounds with vinyl groups, such as acrylic acid, may polymerize in low-temperature plasma via conventional chemical reactions. These include the opening of double bonds under electron impact followed by the propagation of the polymeric chain via the attachment of intact monomeric units. In pulsed discharges

with a millisecond period, this polymerization pathway benefits from long t_{off} when plasma collapses, leaving the chain propagation process to proceed unperturbed. Thus, the original monomer structure is better preserved and become incorporated in the resulting plasma polymer framework during the t_{off} period when its mass accumulation proceeds.

The mean electron energy for a low-temperature plasma is comparable to a characteristic 3-4 eV bond dissociation energy of organic compounds, and the plasma is enriched with radicals originating from the molecular bond cleavage. Usually, the overall ionization degree is low because organic compounds ionization potential is significantly higher than the mean electron energy. Thus, the thin film community has agreed on the radical-induced chain propagation as a primary chemical route of polymerization during t_{off} (Figure 29a) [66,134,136,137]. The increase of the mass flux and atomic concentration of the carboxyl-entities with the expansion of t_{off} at small duty cycles can be explained by the parity of reasoning previously devised. Although P_{on} approaches here relatively high values, the decrease of t_{on} may impose temporal constraints on the kinetics of plasma chemistry. Multiple studies dealing with diagnostics of plasma operating in AA/Ar gas mixture demonstrated that the plasma enters a steady-state regime in the time scale ranging from a few μs up to 20 μs from the beginning of t_{on} [138,139]. The t_{on} at small duty cycles (< 60%) in the current work does not exceed 25 μs, which means that the equilibrium conditions of the plasma may not be reached. Thus, the monomer molecules are able to remain sustained and participate in radical-induced chain propagation reactions regardless of the high power delivered to the discharge.

In high duty cycle (> 60%), both the NP mass flux and O-C=O concentration decay, which may originate from the deteriorative influence of ionic species. It was shown that ions of both charge polarities play an essential role in carboxylic acids plasmas operating at low [124,134,136,139–142] and high [143,144] pressures. Heavy ionic oligomers can be formed by the attachment of the intact monomer molecules either via proton transfer (cationic polymerization, Figure 29b) or via dissociative electron attachment (anionic polymerization, Figure 29c).

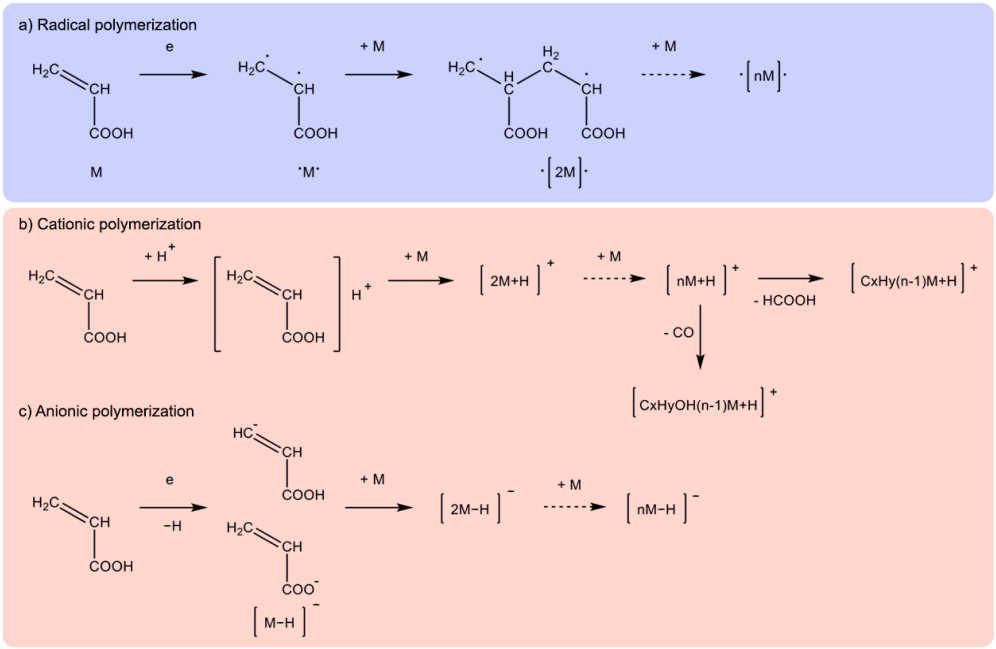

Figure 29. Scheme of the potential chemical pathways occurring in the formation of NPs by plasma polymerization of acrylic acid: a) radical-induced chain propagation; b) proton attachment followed by H+ transfer chain propagation and accompanied by the loss of the HCOOH and CO species; c) dissociative electron attachment followed by anionic chain propagation. M is the monomer molecule, $[M\text{-}H]^-$ and $[M+H]^+$ are dehydrogenated negative and protonated positive molecular ions.

However, because the majority of ppAA NPs are negatively charged, Coulomb repulsion would prevent anionic species (Figure 29c) from attaching to them. Besides, such reactions require much longer time scales (~2 ms of t_{off}) to proceed as witnessed by time-resolved measurements showing no ionic oligomers presence at the shorter afterglow time [141,142]. The ion-molecule oligomerization routes should lead to better retention of the carboxyl entities in the ppAA NPs, which is opposite to the observations at the high duty cycle region. On the contrary, the collisions between monomer molecules and cationic species can result in condensation reactions. Especially at high energies, such reactions lead to subsequent extinction of molecules with low molar mass such as HCOOH and CO [144] and the formation of carboxyl-deficient intermediate products (Figure 29b). The incomplete collapse of the plasma during short t_{off} at large duty cycles is expected to result in the deterioration of the O-C=O functionalities and the NP mass flux by positively charged ions. The mechanism becomes dominating as P_{on} increases and contributes until the moment when t_{off} is long

enough to ensure the complete plasma collapse, whereas t_{on} is sufficiently short. This is the point where the shift in polymerization mechanism occurs and radical-driven polymerization overrides other polymerization pathways.

3.1.3. Segmental dynamics and thermally-driven physical transformations of ppAA NPs

The glass transition phenomenon in plasma polymers is of high importance because it provides insight into the physical properties of the material. Understanding of those is crucial for manufacturing heterogeneous composites aimed to be used in biomedicine. SHS, THz-Raman, XPS and AFM were brought into use to study the segmental dynamics of the ppAA NPs and characterize their thermal evolution.

First of all, the ppAA NPs were deposited onto commercially available chip sensors and the dependence of the complex heat capacity, expressed by the complex differential voltage, on temperature was measured at a fixed frequency of 160 Hz. Figure 30a shows the real part of the complex differential voltage U_R (which is taken as a measure of the real part of the heat capacity) acquired on the NPs deposited at 80 W (CW mode). These NPs have a mean diameter of 15 ± 6 nm and the corresponding O-C=O functional group concentration of 1 at. %. Usually, the glass transition is represented by a step-like change in U_R. By taking the first derivative of U_R with respect to temperature (Figure 30b) the T_g can be more precisely determined as the maximum of the first derivative curve [104,145]. After the first heating run, two maxima for the dU_R/dT curve were detected at 47 °C and 150 °C. The first maximum of the derivative can be assigned to the dynamic glass transition of the plasma polymer. Typically, the glass transition temperature of conventional polyacrylic acid is reported to be above 100 °C [146], which is associated with strong intramolecular hydrogen bonding characteristic of the polymer. The lower values of T_g observed for plasma polymerized acrylic acid originate from the deficiency of oxygen in the resulting plasma polymer structure (14 at. %, see Table 1) when compared to conventional polyacrylic acid (40 at. %), and, as a result, from less abundant hydrogen bonds.

The second maximum of dU_R/dT at 150 °C manifests the onset of the irreversible thermal degradation of the polymer structure: scission of intramolecular bonds, recombination of thus-induced radicals and an overall increase in the cross-link

density. The measurement repeated after several heating-cooling cycles supports this assumption even further by exhibiting the dynamic glass transition maxima shift from 47 °C towards 100 °C. Such a shift implies a dramatic decrease of the average length for the macromolecular sections between cross-link junctions, and, as a result, significantly constrained segmental dynamics.

Next, SHS measurements were performed for NPs deposited at 40 W (CW mode) characterized by a mean diameter of 93 ± 27 nm and carboxyl group concentration of 10 at. % (Figure 30c and 30d). Apparently, the concentration of O-C=O functionalities does not seem to affect T_g as it was found to be at the same position on dU_R/dT curve (at 47 °C) during the initial heating half-cycle run. Thus, it can be inferred that the overall retention of oxygen is a more crucial factor, which is at comparable levels for both types of NPs (Table1). During this scan, the maximal temperature was chosen to be lower than in previous measurements, but the thermal degradation of the plasma polymer was not avoided. Again, the NP properties have witnessed a dramatic change after 8 heating-cooling cycles. Finally, a very broad maximum was observed on dU_R/dT curve throughout the 8th heating, which highlights the higher susceptibility of this less cross-linked plasma polymer towards the thermal degradation.

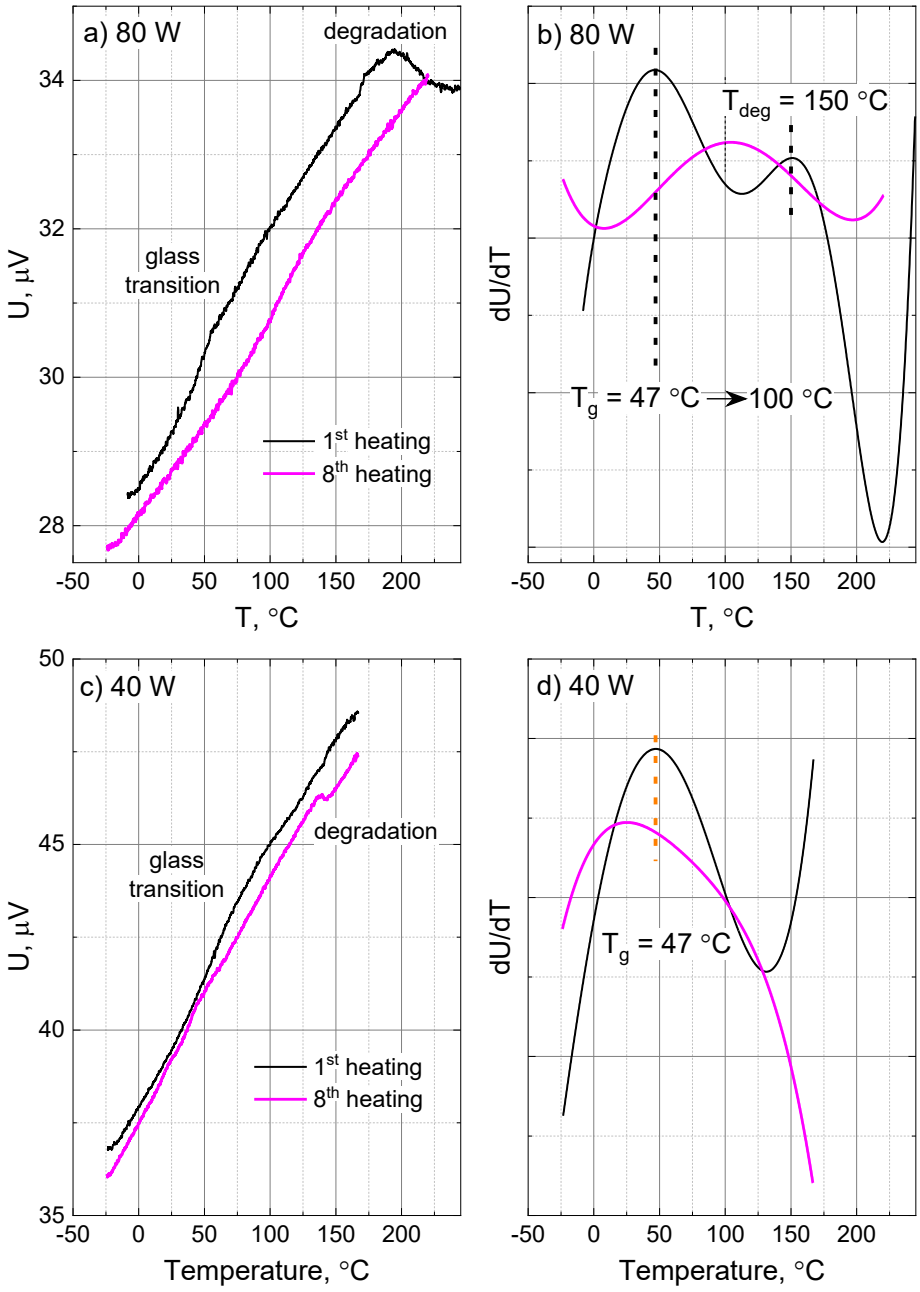

Figure 30. SHS measurements on the ppAA NPs: a) real part and b) the first derivative of the real part of the complex differential voltage versus temperature for a monolayer of ppAA NPs deposited at 80 W; c) real part and d) the first derivative of the real part of the complex differential voltage versus temperature for a monolayer of ppAA NPs deposited at 40 W. The measuring frequency is 160 Hz. The black and magenta curves represent the data acquired during the 1st and the 8th heating run, respectively.

The glass transition peak observed for both original and thermally degraded NPs covers a wide range of temperatures. This phenomenon originates from the diversity and irregularity of plasma polymer network architecture. Such a random structure is inherited from the statistically driven nature of the plasma polymer formation. In general, the glass transition in polymers is highly dependent on the mobility of intermolecularly connected segments and is associated with the length scale shorter than typical chemical bind (roughly < 1 nm). Dangling chains, entanglements, loops and other loosely bound structures occupy the characteristic length scale of 1 - 10 nm [147]. Therefore, these structures of the network topology are either absent in the ppAA NPs, or, at least, they are of secondary importance.

To extend the characterization even further, the samples of ppAA prepared at 40 W (CW mode) were also subject to temperature-dependent in situ THz-Raman spectroscopy analysis in the region of 400 cm^{-1} – 50 cm^{-1}. The results are shown in Figure 31. The initial characterization was carried out at room temperature (20 °C), which yielded an almost featureless spectrum with a low signal-to-noise ratio (SNR). No significant changes in the spectrum were detected after the increase of the temperature from 20 °C to 50 °C. The corresponding spectra look very similar, if not identical. However, after the specimen temperature reached 60 °C, which is slightly above the glass transition devised from previous SHS measurements (~ 47 °C), the SNR of the spectra improved and a set of characteristic bands began to develop at 252, 232, 201 and 166 cm^{-1}. These bands were not detected in the reference Si substrate, which makes them attributable to ppAA NPs. At the elevated temperatures (above 140 °C), the intensities of all the bands are high, while they become attenuated after the sample is cooled down back to room temperature.

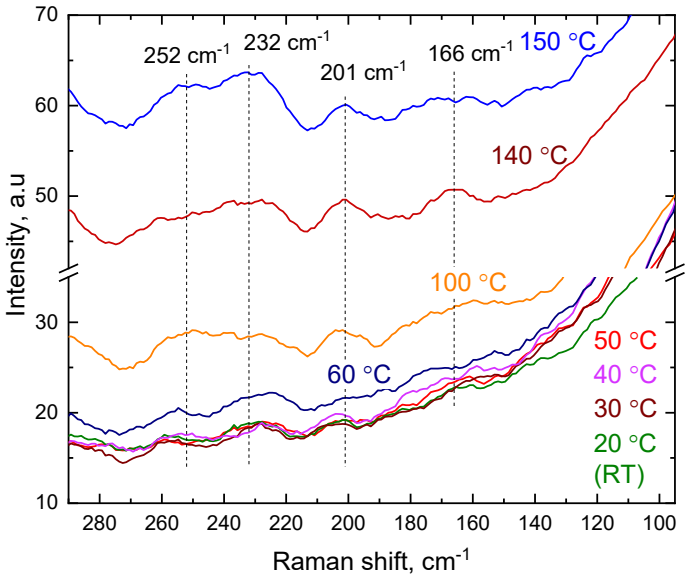

Figure 31. THz-Raman spectra for the ppAA NPs deposited at 40 W CW measured in situ at different temperatures increasing consecutively from RT to 150 °C and then back to the room temperature (RT) after cooling down.

Because the number of works dealing with the study of polyacrylic acid molecular vibrations is limited, the exact assignment of the THz-Raman bands detected for the ppAA NPs in the corresponding spectral range is ambiguous. However, the enhancement of the spectral intensity of these four bands after exceeding dynamic glass transition temperature points to the enhanced cooperative segmental mobility. The rotational movement of interconnected molecular segments is of interest here because the rotation is hampered in the glassy state and becomes relaxed upon the transition to the rubbery state. For instance, a band positioned at 143 cm^{-1} matches the internal rotation about the C-C bond (also known as torsion vibrations τC-) for the solidified acrylic acid monomer, according to calculations in [148]. The shift in the position from 172 cm^{-1} to 202 cm^{-1} was reported in [149] as corresponding to the transition from the liquid to the solid state. Thus, the set of the bands observed for the ppAA NPs at elevated temperatures can be attributed to rotational relaxation of different molecular segments spread across the plasma polymer network.

Markedly, the original envelope of the THz-Raman spectrum is restored when the specimen is allowed to cool down from 150 °C to the RT. This effect evidences a persistence of the ppAA NP elemental composition regardless of thermal degradation

of the NP structure. This hypothesis was confirmed by complementary XPS and AFM study of the additional set of specimens prepared at similar conditions and annealed afterwards. The results are summarized in Table 4. It can be seen that the NP mean size (measured by AFM) dramatically drops down from 130 nm to 16 nm when the NPs are heated above 150 °C. On the contrary, the concentration of carboxyl groups (detected by XPS, Figure 32) remains at comparable levels.

Annealing temperature, °C	20	150	250
(AFM) NP mean size, nm	130±30	52±15	16±3
(XPS) O-C=O, at. %	8.4	7.5	8.2

Table 4. The dependence of the NP mean size and the carboxyl groups' overall content in ppAANPs (prepared at 40 W, CW mode) on the annealing temperature.

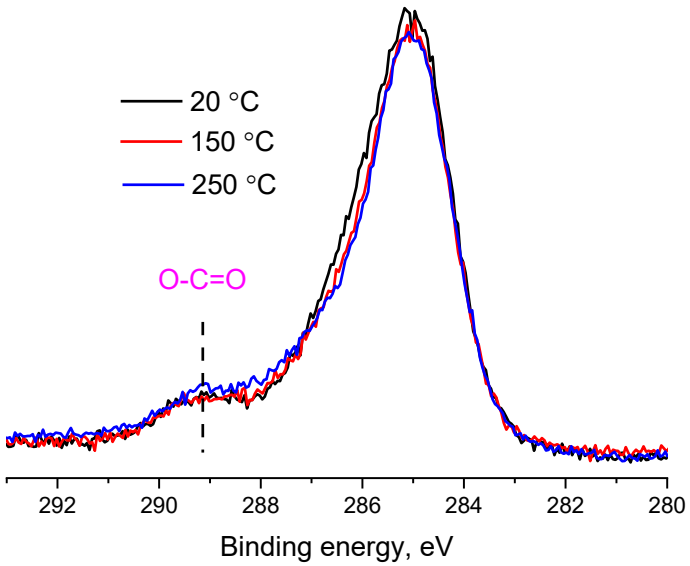

Figure 32. Core-level C 1s high-resolution XPS spectra acquired on the ppAA NPs before and after annealing at 150 °C and 250 °C. The NPs were prepared at 40 W, CW mode.

Early studies [146,150] associated the loss of material that occurs in polyacrylic acid upon thermal degradation with dehydration and decarboxylation as well as chain

scission. The intra- and intermolecular reactions between neighboring carboxyl functionalities were reported to be triggered at 150 °C. Such reactions often lead to the formation of anhydrides and the release of H_2O. When the temperature exceeds 200 °C, anhydrides decompose into cyclic ketones and CO_2 is released as a by-product. Backbone scission typically occurs either close to or above 450 °C.

Although the transformation of carboxyls to anhydrides is unlikely to be detected by XPS, it is still able to point to the transformation of the latter to cyclic ketones, that should be manifested by an increase of the carbonyl-based peak at 288.0 eV at the expense of the carboxyl shoulder at 289.1 eV, which is not the case here (Figure 32). This can be explained by the limited amount of carboxyl groups incorporated into the ppAA NPs. It significantly decreases the probability of carboxyls being neighbors to each other, thus preventing them from mutual interactions that are considered beneficial for the material chemical stability often crucial in biomedical applications.

3.1.4. Stability of ppAA NPs in aqueous media studied by in situ Fluid Cell AFM

Polymerized acrylic acid in the form of thin films is routinely employed in the covalent binding of biomolecules via a dehydration reaction between the carboxyl groups and primary amines of proteins and/or DNA. Nevertheless, the stability of such coatings when exposed to an aqueous environment has always been an issue of serious concern. As shown in Section 3.1.3, plasma polymerization yields the NPs, which are in a glassy state at room temperature. The restricted mobility of the molecular segments makes the ppAA NPs remarkably stable under aqueous media. To demonstrate this point, a sample with a sub-monolayer of the ppAA NPs (40 W, CW mode) deposited onto Si substrate was installed into a fluid cell for in situ FC-AFM measurements.

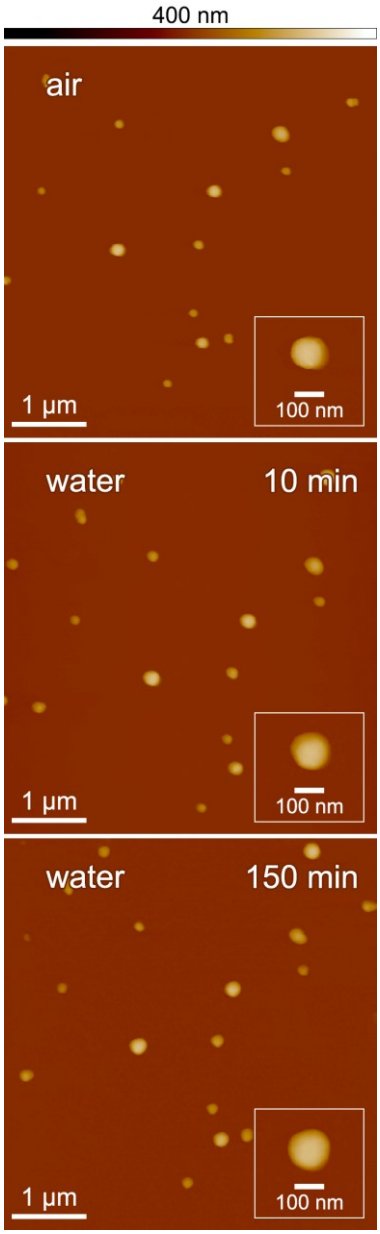

Figure 33. AFM images of ppAA NPs measured in air, then in contact with water for 10 and 150 min after immersion. Insets show a single NP measured in a similar manner (height-scale is 400 nm).

An initial scan of the surface morphology was acquired in an ambient atmosphere (Figure 33). Then, the AFM probe was withdrawn and the cell was filled with ultrapure Milli-Q water (18.2 MΩ cm). A subsequent scan over the identical area was carried out immediately after the water was introduced, and then repeated following 10 min, 1 hour, 1.5 hours and 2 hours of exposure time. One can see from the insets of Figure 33 that the NP size remains unchanged over the timespan. Therefore, neither dissolution nor swelling is effective for ppAA NPs.

3.2. Nano-phase separated plasma polymer composites for spatially-localized attachment of biomolecules

3.2.1. Preparation of ppAA NPs/PEO hybrid composite

The nanocomposite samples were prepared following the experimental protocol (Section 2.1.3): first, 50 nm of ppPEO were deposited onto Si substrates, which was followed by the deposition of sub-monolayers of ppAA NPs and by the final overcoating with a 3 nm thick capping layer of ppPEO. Throughout the chapter, it will be demonstrated that the combination of biorepellent ppPEO thin films and bioadhesive ppAA NPs in one nanophase-separated coating is feasible for the controlled and spatially localized attachment of biomolecules.

3.2.2. Characterization of ppAA NPs/PEO hybrid composite

Segmental dynamics of ppPEO versus ppAA NPs: a key to nanophase separated architecture

The SHS analysis of the ppAA NPs in Section 3.1.3 demonstrated that, at room temperature, the NPs are in glassy sate which is beneficial for their stability in aqueous media. The physical properties of ppPEO films were analyzed in terms of their glass transition temperature and compared with those of ppAA NPs. For this purpose, the samples of ppPEO films were deposited separately onto the AC chips and the SHS measurements were performed.

The dynamic glass transition temperature of the plasma polymerized PEO film was found at T_g = 240 K (-33 °C). According to [102], the melting point of the ppPEO thin films was detected at 298 K (+25 °C). Both these values are in close agreement with the thermal range the phase transitions of conventional PEO typically observed at. Hence, the ppPEO thin films prepared by PAVD are confirmed to have enhanced molecular dynamics at room temperature, i.e., to be in the rubbery state.

Comparing the values of T_g for ppPEO with those obtained for ppAA NPs (Figure 34), one can notice that the glass transition temperature of the ppAA NPs is much higher T_g = 320 K (+47 °C), while its melting point cannot be verified. Although

the T_g for ppAA NPs was found to be lower than for conventionally polymerized AA because of the lack of strong intramolecular hydrogen bonds of carboxyls [146], it is still above RT and, hence, the ppAA NPs are in the glassy state. It is also worth noting that the dU_R/dT maximum is much broader for the ppAA NPs compared to the ppPEO thin film. The broadness of the differential curve maximum points to a high extent of irregularity in the nanoscale architecture of ppAA originating from the randomly-driven nature of the radical and/or ion attachment events (Section 3.1.2). By contrast, ppPEO seems to retain the structure of the original PEO much better due to the milder conditions for plasma polymerization of long oligomer molecules. Good retention of the PEO structure results in the ability of these films to absorb water, swell, and withstand the adsorption of proteins.

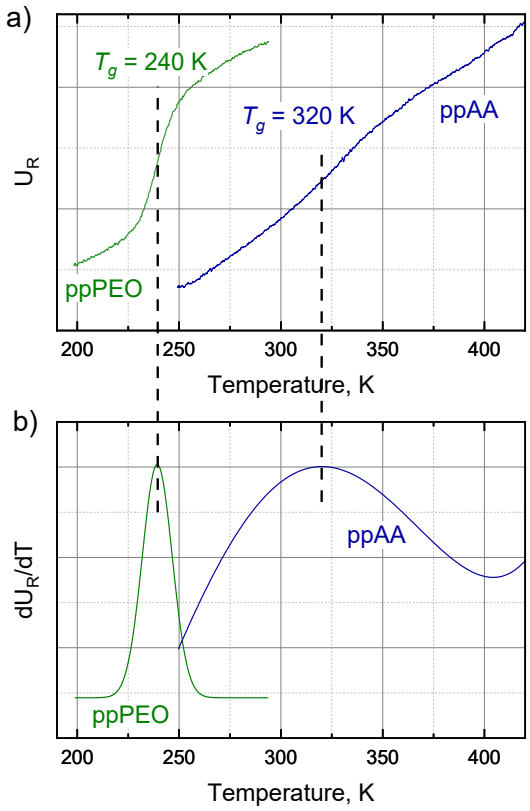

Figure 34. SHS nanocalorimetry of ppPEO film and ppAA NPs measured at a frequency of 160 Hz: a) real part of the complex differential voltage taken as a measure of heat capacity; b) Gaussian fit to the first derivative of a).

Topography and chemical composition of ppAA NPs/ppPEO coatings

AFM operating in intermittent contact mode was utilized to study the resultant topography. The top view AFM images of the composite surface are shown in Figure 35. Herein, the surface of one sample was scanned at various magnifications (Figures a1, a2, a3) to confirm that spherically-shaped ppAA NPs are produced by the plasma polymerization process and that the ppPEO layer surface in between is exceptionally smooth, replicating the minimal roughness of the underlying silicon substrate. The AFM scans of three samples having different amounts of the nanoparticles deposited (b, c and d) empathize the possibility to control the morphology of the composite surface simply by the deposition time of the NPs, ranging from zero to a monolayer coverage. Thus, nanophase-separated plasma polymer composite coatings are produced where two co-existing components exhibit substantially different properties.

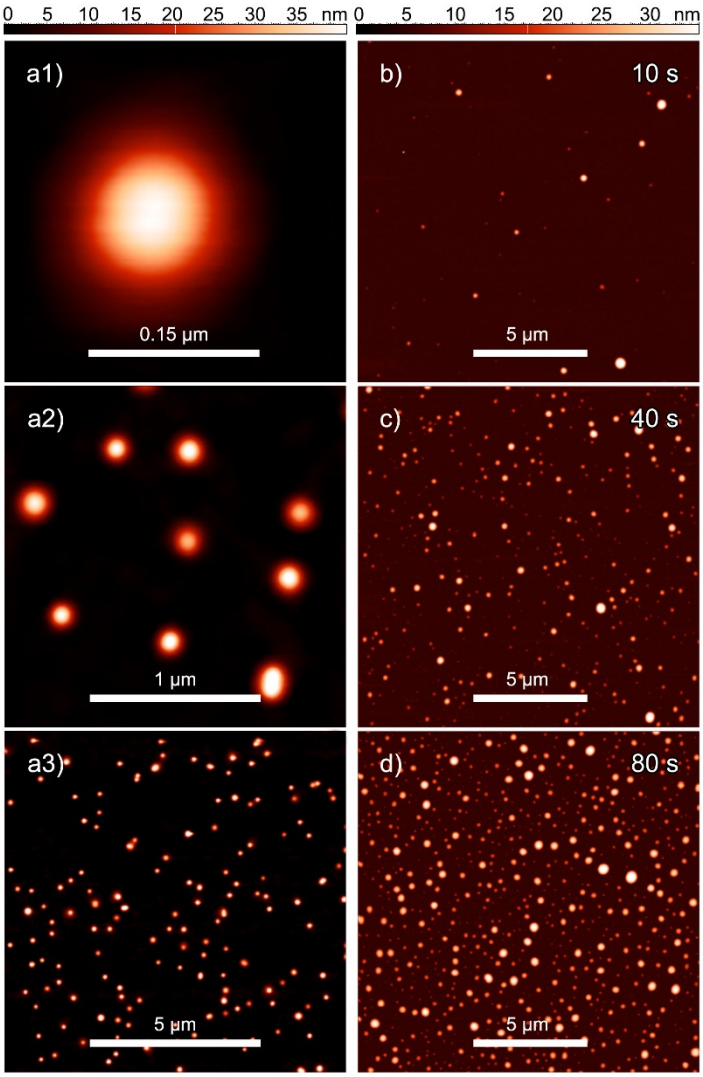

Figure 35. AFM top view images of the ppAA NPs deposited for 20 s onto 50 nm thick ppPEO and overcoated by 3 nm ppPEO with view field of: a1) 0.3 µm × 0.3 µm, a2) 2 µm × 2 µm, a3) 10 µm x 10 µm; and different amounts of ppAA NPs (in terms of their deposition time): b) 10 s; c) 40 s; d) 80 s.

The chemical composition of the ppPEO films and ppAA NPs was verified by XPS (Figure 36, Table 5). Similar to the earlier reports [82,109,151], plasma polymerized PEO is characterized by good retention of the ether groups, which reaches 78 at. % for the experimental conditions (Figure 36a). Smaller contribution from the C-C and the C=O-based groups is related to the formation of cross-links and insignificant chemical transformations occurring during the plasma polymerization. The C/O ratio of the resulting film is also very close to that of the conventional PEO. For ppAA NPs, the deposition parameters were adjusted to ensure the maximum concentration of carboxyl groups. The elemental composition of the ppAA NPs is

represented by a hydrocarbon matrix which incorporates 15 at. % of the O-C=O functionalities (Figure 36b).

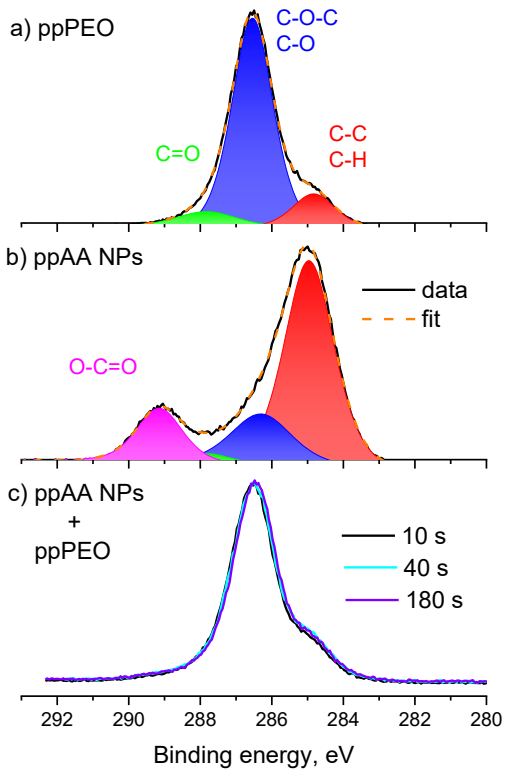

Figure 36. Core-level C 1s XPS spectra of: a) 50 nm thick ppPEO film on Si; b) multilayers of ppAA NPs on Si; c) different amounts of ppAA NPs (in terms of their deposition time) deposited onto 50 nm ppPEO and overcoated by 3 nm ppPEO.

Material	Elemental content, at. %		Chemical bond, at. %			
	C	O	C-C	C-O-C	C=O	O-C=O
PEO	67	33	–	100	–	–
ppPEO	63	37	12	78	10	–
AA	60	40	67	–	–	33
ppAA	80	20	63	19	3	15

Table 5. The chemical composition of ppPEO films and ppAA NPs as witnessed by XPS compared to their conventional counterparts.

Finally, the ppAA NPs/ppPEO nanocomposite samples with different amounts of the NPs were subject to XPS analysis. Figure 36c shows the core-level C 1s XPS spectra recorded for the three nanocomposite samples (50 nm ppPEO/sub-monolayers of ppAA NPs/3 nm capping layer of ppPEO) containing a different number of the ppAA NPs (corresponding top view AFM images shown in Figure 35). Despite a noticeable change in resultant surface morphology induced by the different amounts of the NPs embedded, the spectra show no noticeable difference and seem to look identical to that of ppPEO. Therefore, the capping 3 nm thick layer of ppPEO deposited over the ppAA NPs is sufficient to screen the XPS signal from the NPs. As a consequence, the suggested approach produces the surfaces with substantially different roughness, yet with the nearly identical chemical composition.

Nevertheless, plasma polymerized PEO coating is characterized by the fast dynamics of molecular segments, which makes them permeable for water molecules. The carboxyls dissociate with the appearance of a negative charge on the NP because of the $-COO^-$ ions. Zeta-potential measurements were brought into use to verify this theoretical assumption, as described in the following sub-section.

Presence of electrostatic charges due to dissociation of carboxyl groups in aqueous media by Zeta-potential

The ζ-potential measurements on ppAA NPs/ppPEO coatings unveil exciting peculiarities. Even though the XPS chemical composition of the composite surface corresponds to ppPEO, the ζ-potential does depend on the amount of the incorporated ppAA NPs. Figure 37 shows the dependence of ζ-potential on pH and the number of ppAA NPs (in terms of their deposition time).

Under neutral pH, the ζ-potential decreases from -19 mV for pure ppPEO to -25 mV for a composite with a sub-monolayer of the NPs and further to -40 mV for a monolayer of ppAA NPs, both coated with the 3 nm ppPEO capping layer. Besides, one can notice that the isoelectric point (IEP) of the surface decreases with the amount of the embedded NPs as well.

These phenomena evidence the penetration of water molecules into the hydrophilic ppPEO film, followed by the dissociation of the carboxyl groups on the surface of the NPs. The process is accompanied by a release of protons with the

development of the negative charge due to the $-COO^-$ ions. The negative potential manifests itself through the ppPEO capping layer, causing an overall decrease of the ζ-potential above the ppAA NPs/ppPEO composite surface.

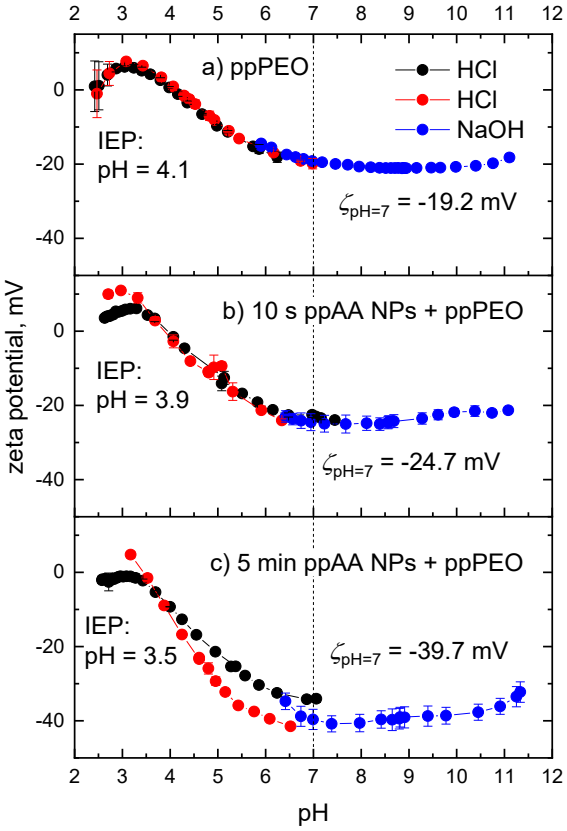

Figure 37. ζ-potential in dependence on pH: a) ppPEO film without ppAA NPs; b) 40±15 nm ppAA NPs deposited for 10 s (sub-monolayer) and overcoated by 3 nm ppPEO; c) the same ppAA NPs deposited for 5 min (monolayer) and overcoated by 3 nm ppPEO.

Although the capping layer implemented to prevent the ppAA NPs from escaping into a biological media becomes a barrier for direct chemical covalent binding of biomolecules, the discovered phenomenon can be used for the spatially-controlled attachment of biomolecules that carry net positive charge when in solution at neutral pH.

3.2.3. Selective binding of biomolecules by the ppAA NPs/PEO hybrid composite

In situ FC-AFM monitoring of electrostatic spatial binding of lysozyme

Lysozymes (LSZ) are widespread enzymes with specific hydrolytic activity against bacterial peptoglycan of cell walls aiming to protect one from the ever-present danger of bacterial infection. Besides its important biological role, Lysozyme has often served as a positively net-charged model protein in recent studies [109,152–155], which makes it a prospective candidate for the electrostatic immobilization tests. The FC-AFM was used to in situ monitoring LSZ adsorption onto the nanocomposite samples with the following architecture: 50 nm pPEO/sub-monolayer of ppAA NPs/3 nm capping layer of ppPEO.

Figure 38 (a1) shows the AFM image of the sample surface acquired under ambient air, whereas the image (a2) is a higher magnification image obtained by scanning over the area designated by a white box. Both these images are in close agreement with previous AFM measurements. The ppAA NPs produced as a result of plasma polymerization are randomly distributed over the specimen and overcoated by the ppPEO capping layer with minimal roughness in between.

After the first scan in air, the AFM tip was withdrawn and the fluid cell was filled with PBS solution, yet containing no LSZ. Then, the probe was engaged again to study the same chosen areas (Figure 38 b1 and b2). The surface morphology had changed rapidly over a couple of minutes that are typically required to position the probe correctly and bring it back into the operation to acquire the first scan. Remarkably, the specimen morphology became smooth and all the NP disappeared. The scans recorded after 60 min and 90 min of the incubation were nearly identical, indicating that the surface relaxation occurs immediately after the PBS is introduced and the morphology remains stable over the long-time span.

Finally, the AFM probe was withdrawn once again and then the lysozyme solution was injected into the liquid cell. The specimen morphology recovers back to the state before the addition of PBS, as witnessed by the subsequent measurements over the area of interest (Figure 38 c1 and c2). The same pattern formed by the NPs can be identified, although slightly shifted because of the AFM drift.

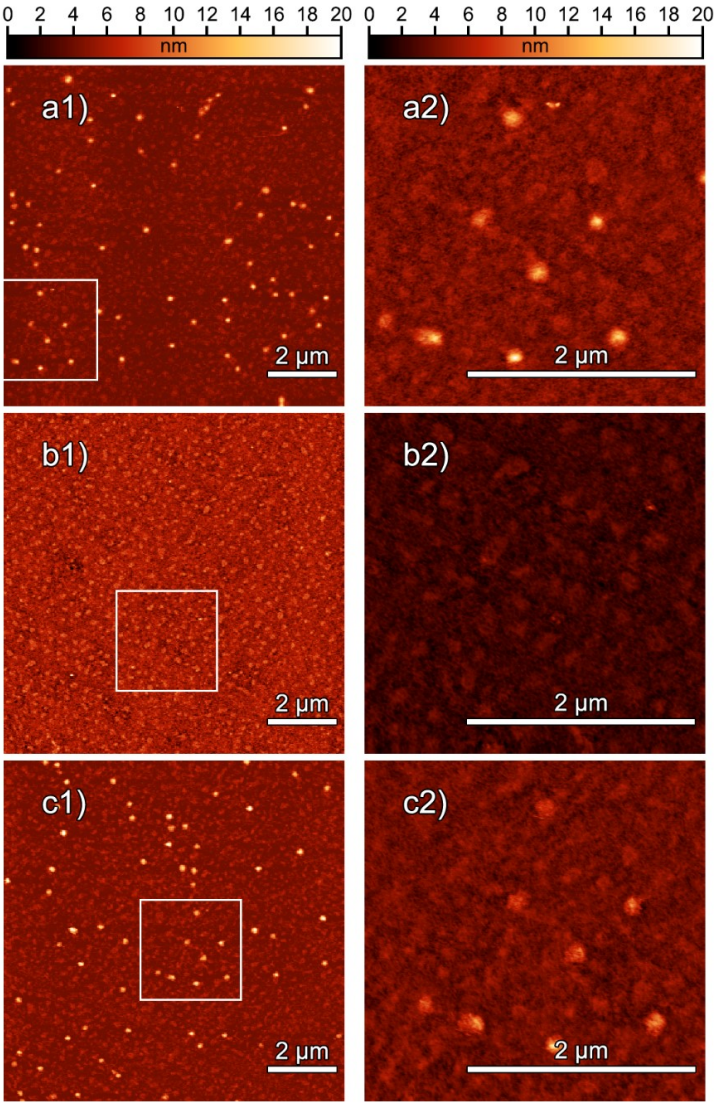

Figure 38. The FC-AFM top view scans of the ppAA NPs deposited onto 50 nm PEO and overcoated by 3 nm PEO layer under: a) under ambient air; b) in contact with PBS solution without LSZ after 30 min of the incubation; c) in contact with PBS solution with added LSZ in 10 min after the addition of the protein. White boxes of a1-c1 correspond to the view field of a2-c2 images.

The interpretation of the FC-AFM can be based on swelling phenomena that the ppPEO thin films exhibit when in contact with aqueous media. Earlier, similar ppPEO films were reported to swell in PBS by about 20 % as compared to the initial dry thickness [151]. Swelling proceeds with the unfolding of macromolecular segments of the polymer network and results in the expansion of the polymer-free volume. Typical time scales reported for swelling are within several minutes.

Conducted SHS nanocalorimetry measurements on ppPEO (Section 3.2.2) confirmed that ppPEO thin films used in the composites are in the rubbery state, which implies fast molecular dynamics in the plasma polymer network and the existence of flexible macromolecular chains.

On the contrary, preliminary FC-AFM measurements performed on ppAA NPs deposited onto Si substrate (Section 3.1.4) showed that the NP size and shape remain intact after their immersion into PBS solution. Such remarkable stability of the ppAA NPs correlates well with the glassy state in which those NPs persist. The glassy state is characterized by restrained segmental dynamics, the smaller free volume inside the plasma polymer, and its inability to absorb water. For this particular application, these results can be considered as positive because, among numerous reports, it was recognized that thin films of plasma polymerized AA develop instabilities due to delamination and/or swelling [156–159].

Combined in a nanocomposite coating, ppAA NPs and ppPEO behave differently when immersed into PBS. The underlying ppPEO film absorbs water, swells and expands so that the NPs become entirely submerged in its outermost layers. Nevertheless, the NPs do not go too deep into the ppPEO matrix because their exact positions are manifested as the lysozyme is injected into the fluid cell. The protein molecules are repelled back from the surface of the non-fouling ppPEO unoccupied by the NPs; however, they identify the locations where the NPs are submerged and attach to them, thus closely replicating the NP pattern.

Ex situ XPS analysis of biomolecule attachment to the plasma polymer nanocomposites

XPS analysis was used to support the hypothesis of LSZ being spatially adsorbed onto the surface sites where the ppAA NPs reside. The idea behind is to use N 1s XPS signal for the semi-quantitative estimation of the amount of lysozyme adsorbed on the specimen after the incubation because neither ppPEO nor ppAA contain nitrogen whereas LSZ does. Figure 39 shows the dependence of the atomic concentration of nitrogen witnessed by XPS on the number of the embedded ppAA NPs for three different types of specimens. The study conducted on the samples where ppAA NPs were deposited directly onto 50 nm ppPEO film without being overcoated

by a ppPEO capping layer revealed that the NPs are washed away from the surface by PBS solution (or aqueous media). Here, the XPS did not detect any nitrogen on this type of surface after the incubation. It should be noted that albeit such configuration was rejected in this work, it still might be of use to transfer the NPs for the covalent binding of biomolecules in the solution.

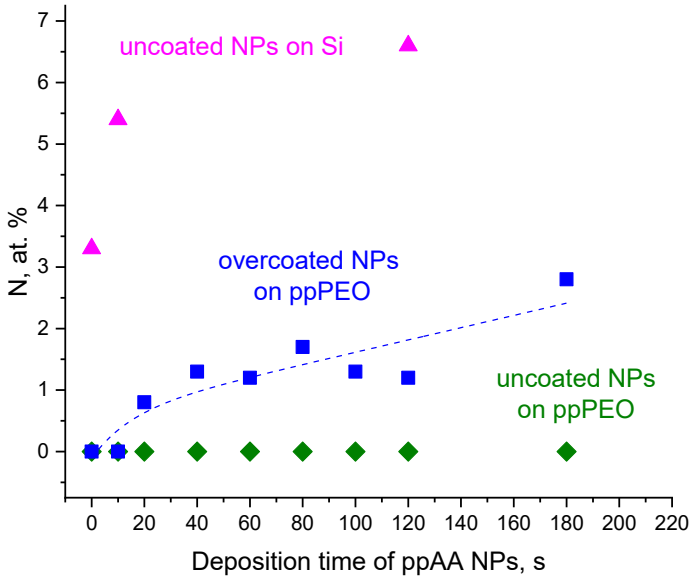

Figure 39. The XPS concentration of nitrogen on the specimens with different amounts of ppAA NPs after their incubation in LSZ solution. Solid circles correspond to the NPs deposited onto Si, open rectangles - to the uncoated NPs on 50 nm ppPEO and solid rectangles - to the NPs deposited onto 50 nm ppPEO and overcoated by 3 nm ppPEO capping layer.

If the ppAA NPs are deposited onto a bare Si substrate (with native Si oxide layer present) with no capping layer, the adhesion between the NPs and Si is sufficient to keep the particles on the surface even after immersion into solution (protein, PBS and ultrapure water were tested). According to the XPS, the nitrogen content increases up to approximately 7 at. % as the number of the ppAA NPs deposited onto the surface grow up. On the contrast, for reference silicon substrate without any deposited NPs, the nitrogen content reaches only about 3 at. %, which corresponds to a monolayer coverage of the substrate by the LSZ molecules. Thus, the observed increase in N 1s signal in the case of ppAA NPs on Si manifests an increased specific area available for the protein adsorption. However, the spatially-specific character of the adsorption

cannot be reached because LSZ tends to adhere both to the ppAA NPs and the Si substrate. Finally, the nanocomposite coatings showed a similar trend to ppAA NPs on Si; however, the increase of nitrogen was moderate. In addition, the 50 nm thick ppPEO film deposited onto Si was tested. Without NPs embedded, it does not adsorb lysozyme as the N 1s XPS signal is zero in this case. The nitrogen content increases with the number of the incorporated ppAA NPs but reaches four times smaller level compared to the same amount of the NPs deposited on Si. This finding confirms that the ppPEO film is characterized by good non-fouling properties and is resistant to the accumulation of the protein whereas the LSZ molecules adhere specifically to the spots with the underlying ppAA NPs as shown previously on the FC-AFM.

Taking into account that segmental dynamics of ppPEO becomes significantly constrained in the vicinity of rigid NPs on the scale of a few nanometers [145], it may be argued that the mechanism of the protein adsorption in our case is related to the restrained mobility of molecular segments in a 3 nm thick capping layer of ppPEO adhering to a glassy ppAA NPs. Nonetheless, such an increase is probably still insufficient to deteriorate the non-fouling properties. To confirm this hypothesis, a complementary experiment was carried out in which the same number of the embedded ppAA NPs was overcoated by ppPEO capping layers of different thickness and then tested against the LSZ adsorption. The results of XPS analysis of these samples are summarized in Table 6.

sample	N, at. %	
	50 nm ppPEO + NPs + capping layer	Si + capping layer
capping 1 nm	4.1	0.6
capping 3 nm	2.8	0.0
capping 5 nm	2.2	0.0

Table 6. The XPS concentration of nitrogen on the ppPEO samples with or without the ppAA NPs after their incubation in lysozyme solution.

Post-incubation XPS measurements evidence that ultra-thin films of ppPEO deposited onto Si remains non-fouling above critical thinness of 3 nm. Below that threshold, for example, at 1 nm thick capping layer, the first indication of the protein

adsorption was observed. On the other hand, the nanocomposite samples do show the adsorption of lysozyme, with the amount of the adsorbed protein increasing with the decreasing thickness of the ppPEO capping layer. Thus, it can be pointed out that electrostatic interaction between the submerged and negatively charged ppAA NPs and positively charged lysozyme molecules is mainly responsible for the phenomena observed for the samples with the 3 nm thick ppPEO capping layer.

3.3. Impact of spatial confinement and glassy dynamics on pattern formation in bi-component plasma polymers

Phase transition and segmental dynamics in polymer thin films are keys to control the resulting coating morphology and architecture at the nanometer scale. They are of high importance not only from the viewpoint of fundamental research but also in many applied fields where the knowledge of correlations between the segmental mobility and the resultant structure of a polymeric film may explain or predict the performance of a polymer-based device. In the previous two Paragraphs 3.1 and 3.2, the research was focused, primarily, on the concept of hybrid plasma polymer-based coatings for spatially-resolved biomolecules adhesion. Throughout the pathway towards this goal, the importance of plasma polymer spatial confinement and segmental dynamics was explicitly demonstrated through the development of plasma polymer composites with phase separation at the nanometer scale and its overall performance driven by the different behavior of ppAA and ppPEO upon contact with aqueous media.

The current part of the thesis aims to be more focused on mechanisms of the macromolecular surface diffusion, providing the reader with a more in-depth insight into the nanoconfinement effects and the aggregation kinetics of nanometer-scale PE islands growing on PEO. Unveiling such mechanisms may help in designing advanced devices that take advantage of unusual properties of polymers at the nanoscale. Herein, a solvent-free plasma-based approach was applied to decorate the surface of PEO thin films with two-dimensional PE nano-islands.

3.3.1. Plasma-assisted growth of PE fractal-like nano-islands on PEO films

Deposits of PEO and PE prepared by vaporization were shown to inherit their chemical structure from the precursor polymers, corresponding either to $(CH_2\text{-}CH_2\text{-}O)_{25}$ or to $(CH_2)_{100}$ oligomers as reported in [109,160] after NMR, XPS and FTIR analysis. The GPC was conducted on the specimen with both PEO and PE prepared either with or without plasma to characterize molar mass distributions. The results are summarized in Figure 40. The GPC analysis reveals that the molar mass distribution is characterized by $M_n=1.1\times10^3$ g/mol with dispersity D_M = 1.36 for PEO and $M_n=1.4\times10^3$ g/mol with D_M = 1.10 for PE, both deposited without plasma. If the plasma is employed, the released molecular fragments become activated with the formation of radicals that can participate in the recombination reactions upon reaching the surface. The radical recombination causes the oligomers to partially re-polymerize and, thus, to grow to larger macromolecular chains. Figure 40 demonstrates that broad molar mass shoulders develop for both PEO and PE films deposited with plasma assistance. In this case, the molar mass distributions are characterized by the bimodal character.

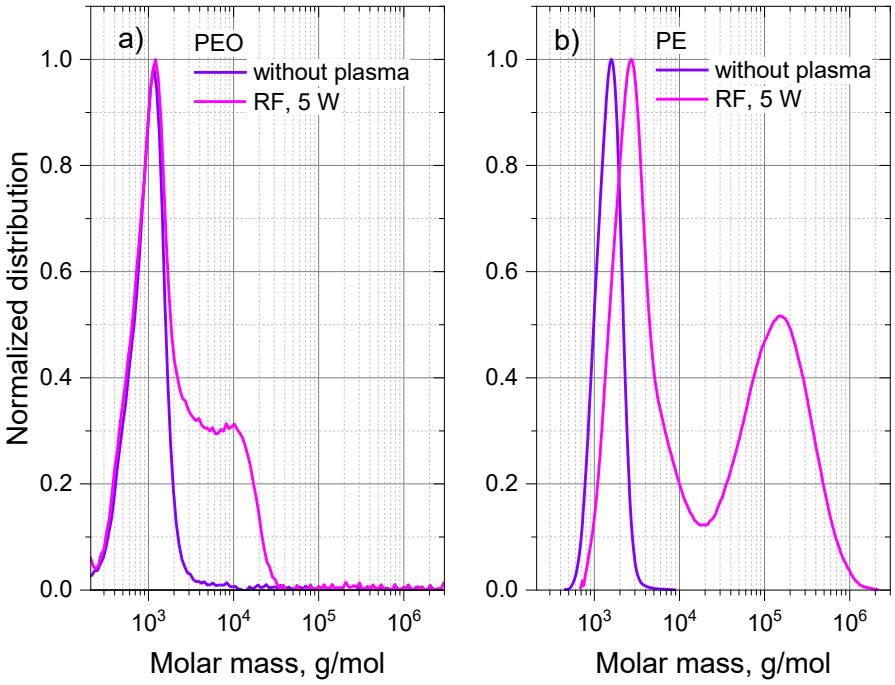

Figure 40. Molar mass distribution determined by GPC and normalized to maximum: a) PEO and b) PE films deposited with and without plasma.

The PEO films deposited via PAVD on Si substrates are characterized by smooth and continuous morphology due to a good wetting of the hydrophilic Si surface by hydrophilic PEO [109], while the simultaneous co-deposition of PEO and PE on Si leads to the formation of microphase-separated thin polymer films due to immiscibility of hydrophilic PEO with the hydrophobic PE [82]. Herein, PE was sequentially deposited onto PEO, which resulted in aggregation of PE isolated islands on the PEO surface caused by poor wetting of hydrophilic PEO surfaces by the hydrophobic PE. The PE oligomers aggregation is driven by the tendency to minimize the system surface free energy via the reduction of the contact area with the PEO surface.

The samples were subjected to AFM analysis (Figure 41), which confirmed the formation of fractal PE nano-islands on PEO. This will also be demonstrated by AFM-IR analysis showing the attenuation of the IR signal from the ether groups of PEO in the areas covered by the PE islands (Section 3.3.3). Complementary XPS analysis (Figure 42) further supports this finding by showing a noticeable drop in the concentration of the ether groups for the sample with the PE nano-islands compared to the reference specimen with PEO film. The single-phase PEO and PE thin films are represented by the retention of the ether and aliphatic hydrocarbon functionalities, respectively. The spectrum of PE islands on PEO is characterized by the comparable contributions from the C-O-C and the C-C/C-H entities.

The morphology of islands was studied in dependence on the deposition time to get insight into the island growth kinetics. The height-mode AFM images (Figure 41) demonstrate the typical fractal growth on the 100 nm PEO film (with plasma, 10 W, CW). In the beginning, pre-formed islands bear a resemblance to dendrites, which are characterized by little fractal randomness across their branches [161,162]. The dendrite structure vanishes as the island growth proceeds, and, at longer deposition time, the structure is found to be identical to fractals that typically grow under the DLA regime [45,163]. The fractal structure points to remarkable kinetics of the island growth: the macromolecular PE oligomers may randomly diffuse over the PEO surface upon reaching it. The randomness of the resulting fractal morphologies observed for all the growth stages provides evidence that the edge diffusion responsible for turning fractal-like deposits into compact islands is almost negligible, i.e., the oligomers remain immobile after attachment [164].

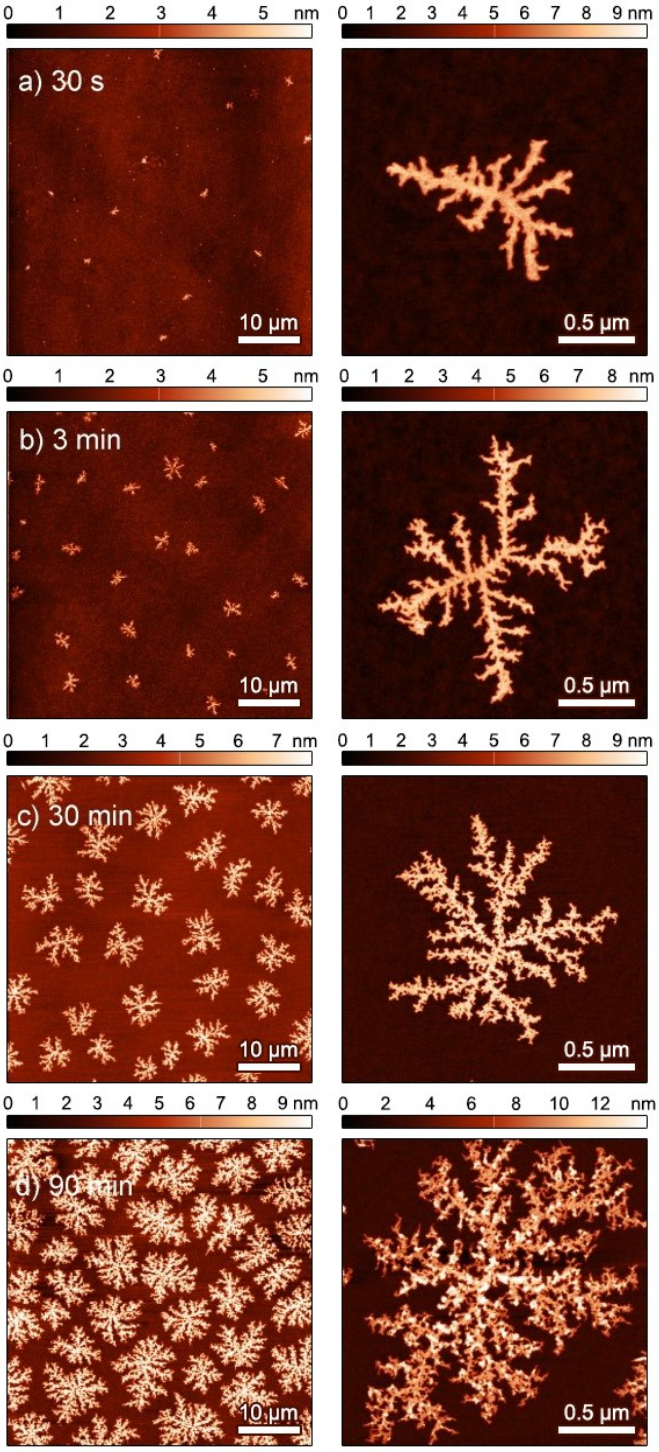

Figure 41. Top view AFM images of PE islands deposited on 100 nm thick PEO film with different deposition times: a) 30 s; b) 180 s; c) 30 min; d) 90 min. The left column corresponds to 50×50 µm scans, the right column shows individual islands at higher magnification. The deposition parameters are: for PEO - the discharge power is 10 W, the QCM deposition rate is 20 Hz/min, the deposition time is 20 min, the crucible-substrate distance is 10 cm; for PE - the discharge power is 5 W, the QCM deposition rate is 20 Hz/min, the crucible-substrate distance is 20 cm.

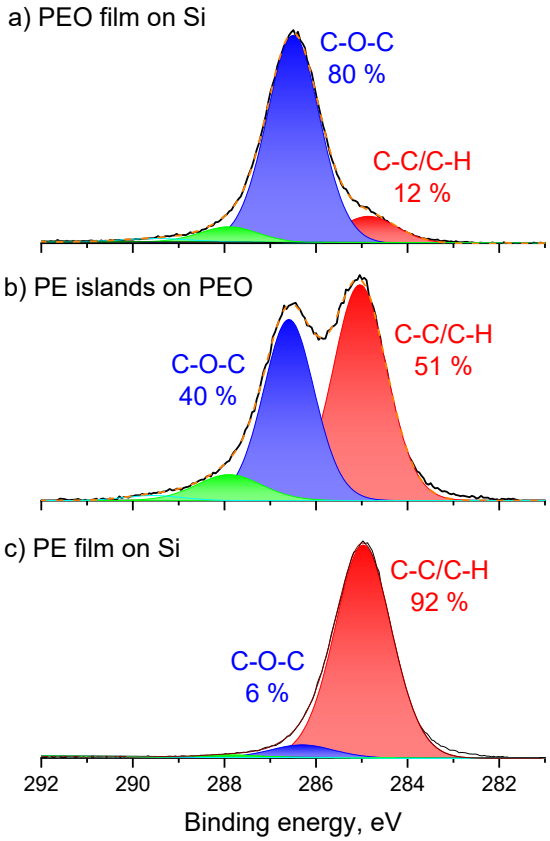

Figure 42. Core-level C 1s XPS of: a) 100 nm PEO film on Si; b) PE islands deposited on 100 nm PEO film; c) 100 nm PE film on Si.

The DLA growth manifests itself through the island areal number density remaining constant (37±5 islands per 50×50 μm area) in time. Apparently, the newly arrived species diffuse to and become a part of already existing islands, instead of forming new ones. Besides, AFM analysis reveals the islands growth in a 2-dimensional regime, i.e., their height (thickness) remains constant (about 7 nm) from the island center towards the periphery, while PE islands occupy a larger area with the deposition time (Figure 43).

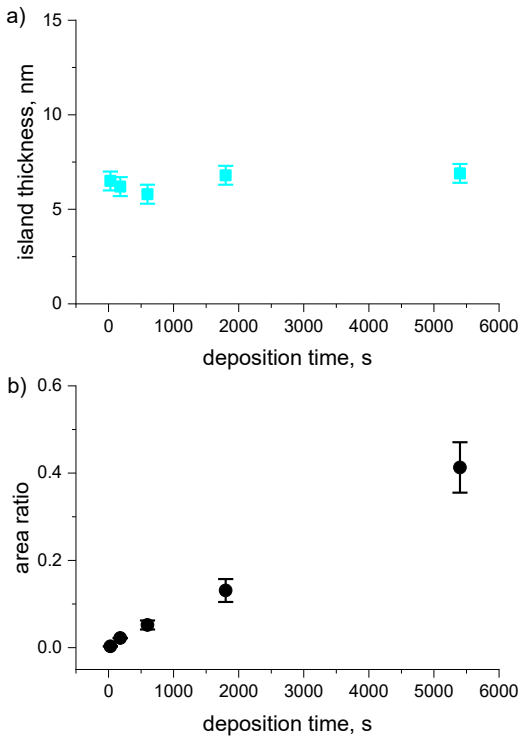

Figure 43. Time-domain evolution of PE islands on 100 nm thick PEO film in terms of: a) island thickness; b) occupied area ratio.

Thus, the oligomers arriving on top of existing islands do not contribute to the increase of the island thickness but to the expansion of islands in the lateral direction (i.e., the Ehrlich-Schwoebel step barrier [49,165] is relatively small). Although, it should be noted that local isolated points with a higher thickness are observed occasionally (this will also be addressed in Section 3.3.3).

3.3.2. DLA-dendrite crossover driven by a variable PEO film thickness

Another intriguing effect arises upon the variation of properties of the PEO underlayer. The latter has a significant impact on the resulting morphology of the islands. Figure 44 demonstrates this crossover from random DLA-like fractals, typically observed for PE on thick PEO underlayers (100 nm), to ordered star-shaped dendrites growing on thinner PEO films (tens of nm). For the reference, the sample

with a blank Si substrate was analyzed. In the following case, only branched nano-islands were observed without any traces of ramified fractal branching.

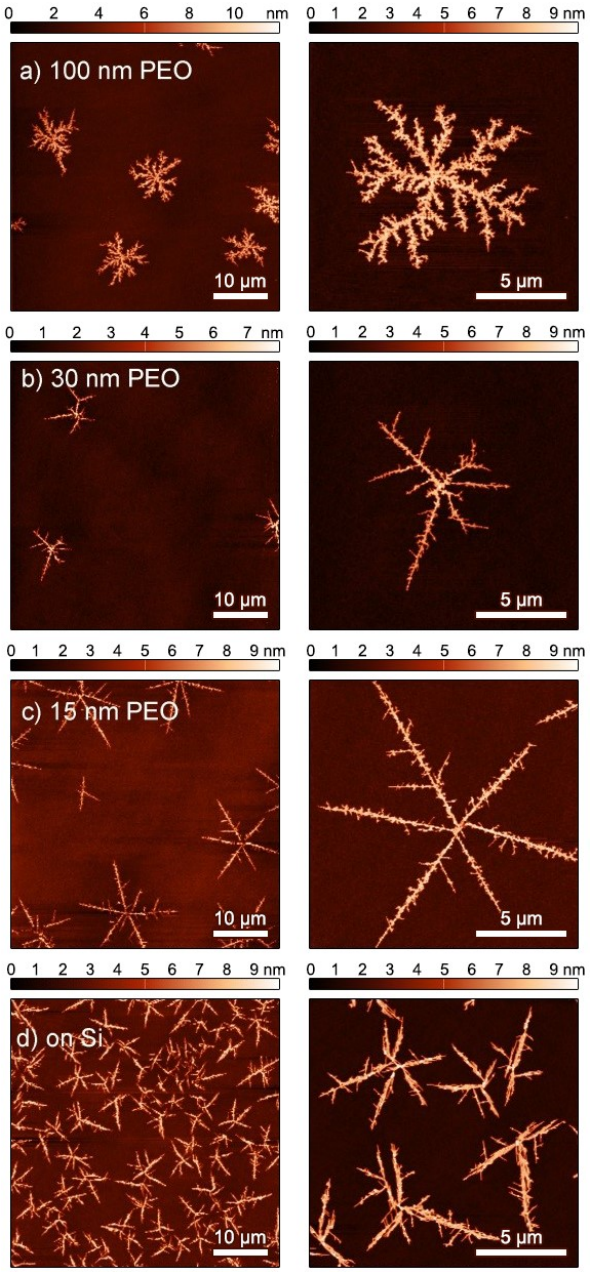

Figure 44. Top-view AFM images of PE islands formed on PEO films with different thickness: a) 100 nm; b) 30 nm; c) 15 nm; and d) on blank Si. Images on the right-hand side show individual islands at higher magnification. The deposition parameters are: for PEO - the discharge power is 10 W, the QCM deposition rate is 20 Hz/min, the deposition time is 20, 6 and 3 min, the crucible-substrate distance is 10 cm; for PE - the discharge power is 5 W, the QCM deposition rate is 20 Hz/min, the deposition time is 30 min, the crucible-substrate distance is 20 cm.

The morphological genesis from DLA fractals to dendrites by itself implies a microscopic anisotropy described in more detail in [166]. The origins of such a phenomenon lie in either symmetry of the underlying "substrate" surface or the aggregating molecules [167], [168]. However, the latter case can hardly be the reason for PE-PEO composites because the deposited PE oligomers are neither symmetric nor systematically anisotropic. Moreover, morphological transformations caused by molecular symmetry were previously reported to depend on the deposition rate [161,162,166], which is not the case in the current experiment.

Thus, it can be inferred that the probable source of the anisotropy is the Si surface. Indeed, the corresponding AFM images (Figure 44d) demonstrate branched anisotropic structures with no diffusive fractal randomness on blank silicon. Only the PE diffusion onto PEO underlayer ensures the randomness. Thin PEO films are not capable of sufficient screening of the Si surface anisotropy, whereas screening of thicker layers is strong enough to produce random fractals. In Section 3.3.4, it will be demonstrated that the screening property is related to the flexibility of the PEO coating, which is in the amorphous state.

Finally, it is worth mentioning that even 100 nm thick PEO cannot completely screen Si anisotropy, which shows up to a certain extent during the initial stages of the island growth (Figure 36a), resulting in the dendritic patterns. At longer times, however, the diffusive randomness prevails and larger islands resemble DLA-like fractals with little trace of the anisotropy.

3.3.3. AFM-IR analysis of the DLA-dendrite crossover

Properties of ultrathin films, including elemental composition, differ from that of bulk materials and their measurement is rather challenging. The AFM-IR, a modern analytical technique, was applied to study in-depth the chemical composition and different modes of segmental dynamics in the nanoscale PEO films and PE nanoislands. The acquired information provides additional insight into the DLA-dendrite transition discussed previously within Section 3.3.2. The samples were prepared as follows: the PE islands were deposited onto the 100 nm and 15 nm PEO films. Then, the samples were subject to AFM-IR scan where the topographic (height contrast, classical AFM mode) images were acquired simultaneously along with the

mapping of the IR signal at 1102 cm^{-1} to highlight the distribution of PE islands on PEO. This specific wavenumber corresponds to the stretching vibrations of the C-O-C groups, which are characteristic for PEO, but not present in PE. The results are shown in Figure 45 a) – d). Herein, the PE domains exhibit a weaker signal at 1102 cm^{-1} than the PEO matrix and, therefore, the IR scan is characterized by a strong contrast between the PE islands and the PEO film. The control measurement at 1460 cm^{-1} (bending vibrations of methylene groups present both in PE and PEO) returns images of notably less contrast, which is consistent with the presence of these vibrations both in PEO and PE (not shown).

After IR-map was constructed, the particular spots (shown schematically by red and blue circles in Figure 45a and 45c) belonging either to the PEO film or to a PE island deposited on top of the underlying PEO film were chosen. Figures 45e and 45f show the IR spectra obtained at these spots. For all the spectra, the following characteristic absorption bands were recognized: bending vibrations of the methylene CH_2 groups at ~1460 cm^{-1}, stretching vibrations of the carbonyl (C=O), and the ether (C-O-C) groups at ~1730 cm^{-1} and ~1102 cm^{-1}, respectively.

According to previous reports, both PE and PEO are characterized by the presence of the CH_2 bending vibration band [82,109,160,169–174]. Therefore, this particular band was chosen for the spectra normalization. The carbonyl species typically originate from post-deposition reactions between oxygen and the radicals incorporated in the cross-linked plasma polymer network when the samples become exposed to the ambient atmosphere [108,175–179]. The signal from carbonyl entities is also present in the core-level C 1s XPS spectra for both PE and PEO at 288.0 eV (Figure 42). The C-O-C functionalities were used as a marker to provide chemical contrast between the PE domains and the PEO because they are characteristic for PEO and absent in PE. This band becomes attenuated when measured on PE islands regardless of PEO underlayer thickness. However, the attenuation becomes more significant in the case of 15 nm PEO where the underlayer thickness is comparable to that of the PE island domain.

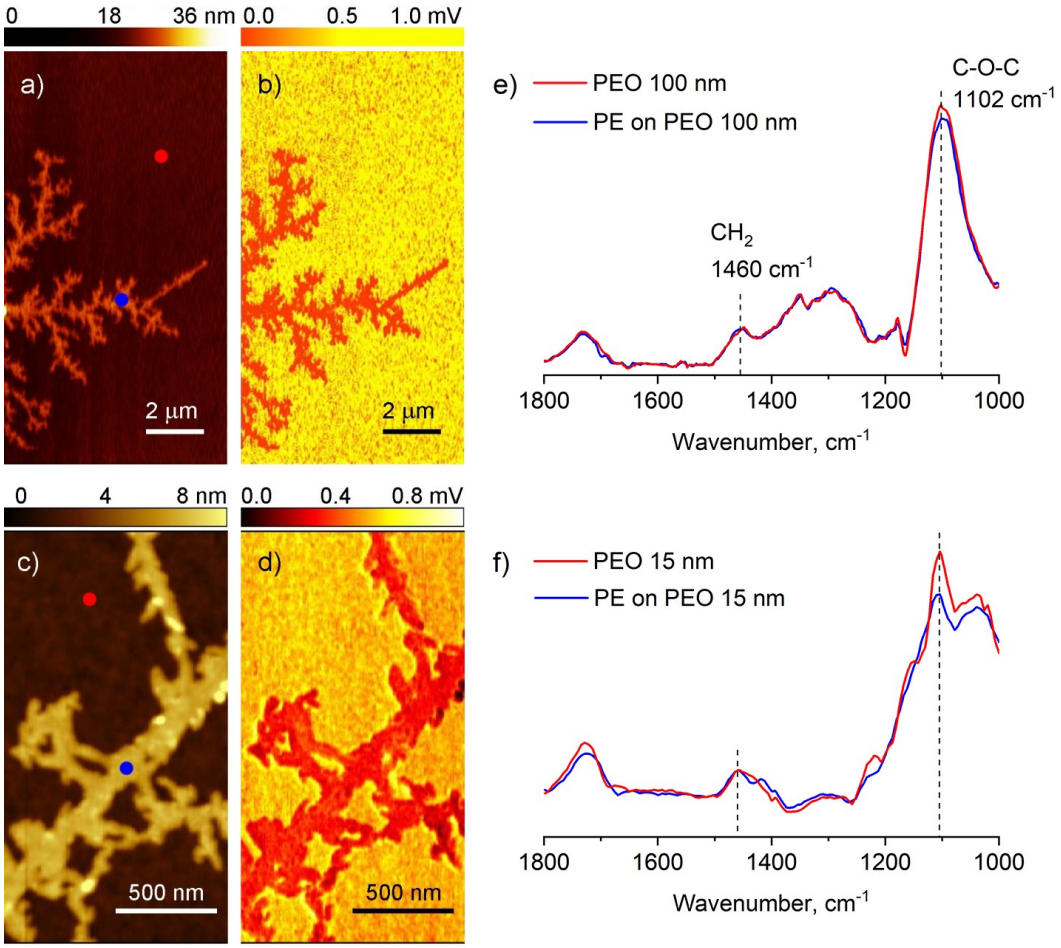

Figure 45. Top-view AFM-IR (intermittent contact mode) of PE islands on PEO films: a) height image on 100 nm PEO; b) corresponding IR image at 1102 cm^{-1} belonging to the C-O-C groups; c) height image on 15 nm PEO; d) corresponding IR image at 1102 cm^{-1}. AFM-IR spectra of PE islands on PEO and of PEO itself: e) 100 nm thickness of PEO; f) 15 nm thickness of PEO. The spectra are normalized to the intensity at 1460 cm^{-1}. The corresponding spots for acquiring the IR spectra are shown by red and blue circles in a) and c) images.

Besides the elemental mapping, it is also possible to extract some information about segmental dynamics. A close look should be paid to the IR spectra of 100 nm and 15 nm PEO samples, in particular, to the difference within 1400-1200 cm^{-1} region (twisting and wagging vibrations of the methylene groups [109,160]) and at the region with wavenumbers < 1070 cm^{-1}, also known as a fingerprint region. The latter contains the information on cooperative vibrations of sets of molecular entities, e.g., segmental dynamics of the material. The methylene bending vibrations (1460 cm^{-1}) are typically directed perpendicular to the macromolecular backbone (latitudinal motion) while the twisting and wagging vibrations of these functionalities are characterized by

longitudinal motion alongside the backbone. It can be inferred that the longitudinal vibrations are present in the 100 nm PE/PEO sample but suppressed in the 15 nm PE/PEO.

Such difference implies that thicker films exhibit more dynamical freedom due to the greater mobility of polymer segments in comparison with thinner films, which are rigid and less disordered [180,181]. Thicker PEO layers, being inherently more disordered and expressing less restrained segmental dynamics, are able to screen the local symmetries of the Si substrate beneath, thus making the growing PE islands to resemble random DLA fractals instead of star-shaped dendrites observed on thin films. On the other hand, one can notice the presence of shoulder at 1020 cm^{-1} that extends towards low frequencies for 15 nm PEO sample, whereas the 100 nm thick sample demonstrates a slope instead. The exact assignment of this band is not straightforward, yet it highlights the diversity in segmental dynamics observed for thin (15 nm) and thicker (100 nm) PEO films.

3.3.4. Fractal morphology controlled by glassy dynamics in PEO films

As was previously stated, the second type of perturbation of random DLA-like fractals originates from the screening properties of the PEO underlayer, which, in turn, can be related to the coating flexibility and, therefore, to the crosslink density in the PEO underlayer. A concept of energy dose, described in detail across earlier Sections, also holds in case of PAVD deposition of PEO thin films. Therefore, the plasma power was employed as a primary parameter to control the cross-linking density of the PEO film. By analogy with ppAA NPs, the power increase causes the following enhancement of the plasma density, which, under the constant feed of the oligomers, leads to intense fragmentation of macromolecular species and, thus, to an increase of the number of cross-links in the deposited films [164]. The statement is further supported by [182], where various rubber elasticity models were modified to account for the finite extensibility of PEO network chains as well as for the constraints induced by the film adhesion to substrate.

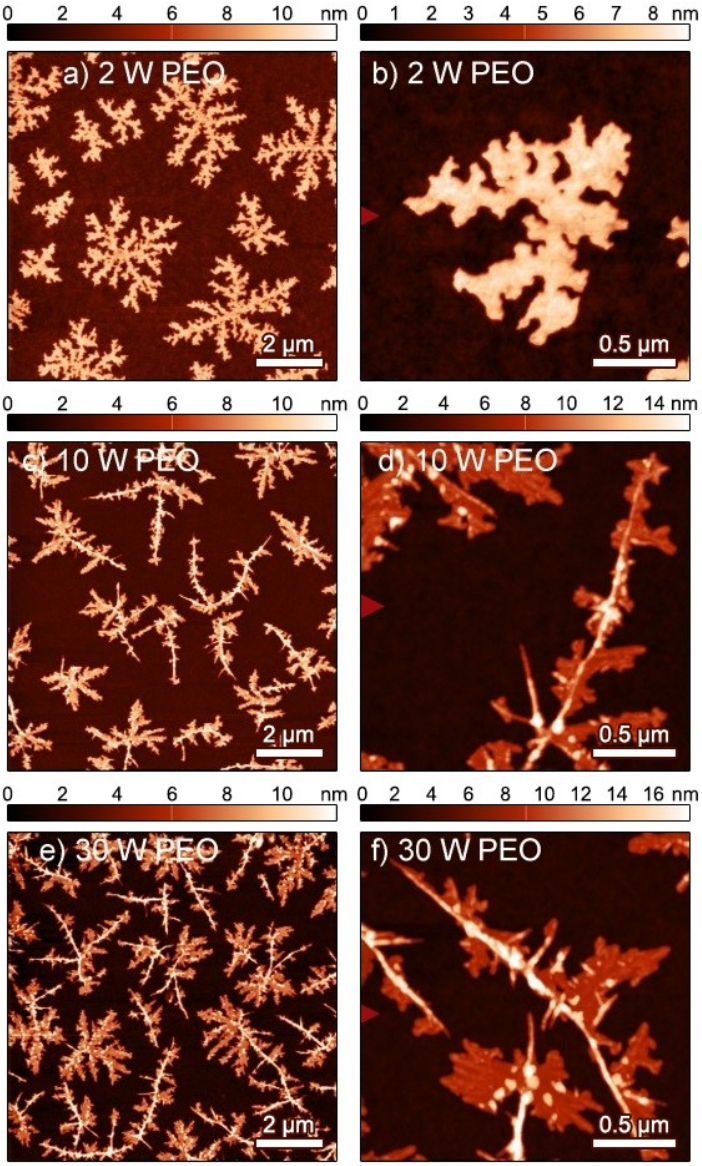

Figure 46. Top-view AFM images of PE islands deposited on 100 nm thick PEO film with different degree of crosslinking accessed via plasma power control: a) and b) 2 W PEO; c) and d) 10 W PEO; e) and f) 30 W PEO. The left column corresponds to 10 x 10 µm scans; the right column shows individual islands on 2 x 2 µm scans. The PEO and PE deposition times are 20 min and 30 s, respectively. For both polymers, the QCM deposition rate is 20 Hz/min, while the crucible-substrate distance is 10 cm. The plasma power used for PE deposition is 5 W.

The PE island shape morphs into the asymmetric stretched fractal that is characterized by a lower degree of randomness in the structure of its branches, as shown in Figure 46. The different dynamics can drive this morphological transformation in polymeric chains localized at the PE-PEO interface. The DSC measurements performed on the bulk specimens of similar amounts detected the PEO and PE melting temperatures to be located within the ranges of 270-283 K and 363-373 K, respectively (Table 7) [82,102]. Although, it is known that the properties of materials at the nanoscale may differ from the bulk phase. To study thin films, the more precise SHS analysis was carried out. The data acquired on the multiple samples prepared at various plasma power values showed that 100 nm thick PEO films exhibit a decrease of melting temperature from 307 K to 278 K as the discharge power increases [102].

Homopolymer	T_{melt}, K DSC on bulk samples	T_g, K DSC on bulk samples	T_{melt}, K SHS on 100 nm film	$T_{g,\ 10\ Hz}$, K SHS on 100 nm film
PEO 2 W	270 - 283	205 - 230	307	235
PEO 10 W			297	245
PEO 30 W			278	268
PE 5 W	363 - 373	~ 300	not measured	not measured

Table 7. T_{melt} and T_g of PEO and PE films prepared by Plasma-Assisted Vapor Phase Deposition.

A thermocouple was attached to the substrate during the PAVD deposition to characterize the temperature changes. In the beginning, the substrates were at room temperature (approximately 298 K) and the temperature increased by 5 K after 30 min of deposition run. Thus, PE island growth proceeded under the conditions where the PEO underlayer was heated above its melting temperature, i.e. the PEO film was characterized by the amorphous state. This means that all the morphological and chemical changes cannot be explained by the different crystallinity of the PEO underlayer. Nor can these changes be driven by the crystallization phenomena in PE, regardless of the PE melting point being above the measured substrate temperature. Similarly, an attempt to grow PE on bare Si substrate without plasma was made, where

the compact islands without the development of elongated arms in any preferential directions were obtained [160].

The dynamic glass transition temperature of the PEO thin films increases following the enhancement in the polymer crosslink density: SHS detects the shift from T_g of 231 K for films with no cross-linking (deposited without plasma assistance) to T_g of 268 K for highly cross-linked films (prepared by PAVD utilized 30 W plasma power) having similar thickness [102]. These temperature values indicate that the PEO films remain in the rubbery state under the conditions of the PE island growth. According to the report [180], a 10 K increase of dynamic transition glass temperature corresponds approximately to a decrease of segmental relaxation time by a factor of 1000, which means that the significantly constrained segmental mobility of polymeric chains in the PEO film, characterized by enhanced cross-link density, manifests itself throughout an almost 40 K shift of T_g. In the meantime, the more significant segmental freedom of PEO obtained at lower power can be linked to the more directional growth of the PE islands. To conclude, the PEO underlayer becomes more rigid as plasma power increases, thus, inducing the transition in island shapes from random DLA-like to asymmetric elongated fractals. There is no microscopic anisotropy present that could be responsible for such a crossover because the crosslinked PEO still remains amorphous.

As a final remark, a hypothesis can be made based upon previous thermal analysis. The larger clusters of oligomer species are capable of migrating over the surface of another polymer with the formation of less random elongated fractal structures. Although this idea seems counter-intuitive, it can be explained by close analogy with cluster-cluster aggregation, reported to produce similar elongated fractals [183–185]. Compared to the DLA, where diffusing molecules or atoms attach to an immobile seed/cluster, in the CCA larger clusters can also be formed by aggregation of smaller ones, composed of relatively small numbers of particles, and, therefore, possess more mobility. A high degree of crosslinking in the PEO underlayer results in the formation of a more rigid surface on which PE oligomers are able to diffuse more easily.

3.3.5. Fractal dimension characterization

A convenient way to quantify PE nano-island morphology is a fractal dimension coefficient D_f which was calculated to be within the range of 1.33 and up to 1.67 depending on the experimental conditions. Figure 47 summarizes the dependence of D_f on the PE deposition time, thickness of the PEO underlayer and the discharge power. The first thing to note here is that D_f gradually increases with the PE deposition time. This behavior implies that the frontline of the islands becomes more developed upon their expansion. Nevertheless, the most notable changes were observed in the dependence of D_f versus thickness of the underlying PEO film, where D_f drops from 1.62 (in the case of 100 nm thick PEO) down to 1.33 (for 15 nm thick PEO). One can also notice that the experimentally determined value $D_f = 1.62$ is close to the reference $D_f = 1.72$, usually obtained for the 2D-DLA growth unrestricted by a lattice [186], and to $D_f = 1.63$, obtained for DLA on a square lattice with the sticking coefficient of 1 [187]. Thus, the formation of the fractal-type islands (with higher D_f) occurs with the high sticking efficiency of the PE oligomers capturing by the existing islands.

This morphology is different from that of PE islands grown without plasma on Si substrates. The latter were previously reported to form islands of a compact (non-dendrite) shape [160]. The PE oligomers become re-oriented upon their first contact with an island and/or are re-distributed along the island rim without any confinement caused by radical recombination, impeding the immediate capturing of the oligomers. In the current study, the plasma was employed to induce the formation of radical-bearing oligomers. The main idea behind is that the radical recombination helps to anchor arriving species via the covalent bonds causing the islands to grow with complex shape. The formation of elongated arms with less developed frontline is manifested via D_f, which also decreases with the increase of the cross-link density of underlying PEO. In the case of ultra-thin or highly cross-linked PEO coatings, preferential directions of the island growth appear, which might be an indication of the DLA conditions violation. Apparently, various energetic barriers for the surface diffusion may exist on the PEO surface, thus forcing arriving PE molecules to self-organize into the islands with specific morphology.

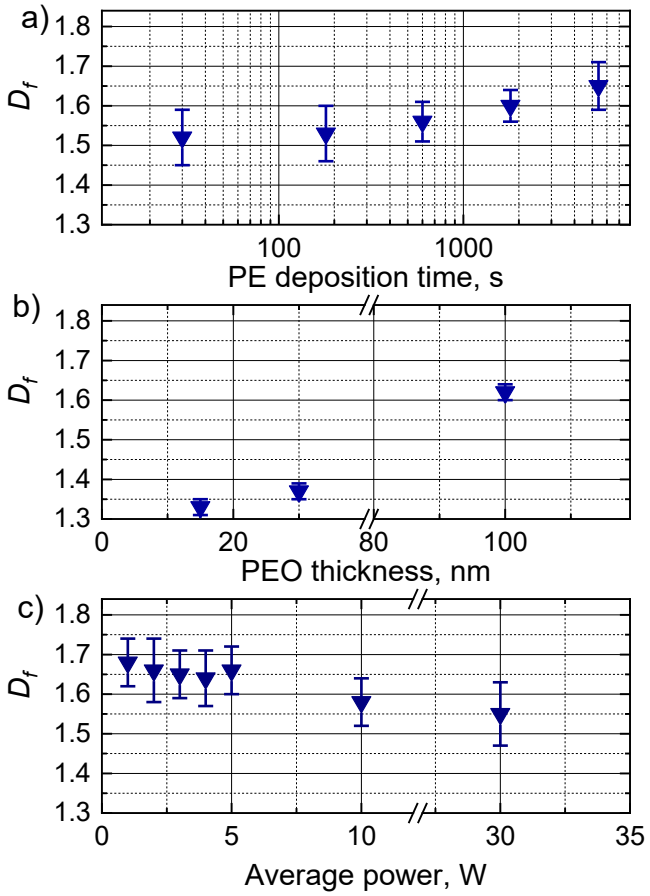

Figure 47. Dependence of D_f (fractal dimension) of PE islands deposited onto PEO underlayer film on: a) the deposition time of PE (on 100 nm thick PEO), b) the PEO thickness and c) the average plasma power used during the deposition of PEO (100 nm thick PEO underlayer). Error bars are calculated as a standard deviation from the mean value of D_f obtained by the processing of at least 30 individual nano-islands.

Conclusions

The objectives of the thesis were successfully solved as follows.

1. For the synthesis and characterization of carboxyl-functionalized plasma polymer nanoparticles:
   1.1. Carboxyl-functionalized plasma polymer nanoparticles (ppAA NPs) with controlled properties and elemental composition can be synthesized via gas aggregation using acrylic acid as a precursor. Both continuous wave and pulsed plasmas are capable of producing such NPs providing high feasibility of the chosen approach.
   1.2. Physical and chemical mechanisms underlying the ppAA NP formation and growth were studied. Two regimes of the NP growth were identified. When the plasma runs at the low duty cycle regime, radical-induced chain propagation through the addition of intact monomer molecules prevails. In the high duty cycle region, collisions of positively charged ions with the growing NPs cause the detachment of low mass components and, therefore, less O-C=O groups become incorporated into the plasma polymer network.
   1.3. The ppAA NPs were found to be in a glassy state at room temperature, i.e., having their segmental dynamics suppressed substantially. Neither dissolution nor swelling phenomena were observed upon 2 hours of incubation of the ppAA NPs in water. Heating the NP above 150 °C results in their thermal degradation, which proceeds with significant structural changes and with an enhancement of the cross-link density; however, the chemical motif is retained. Thus, the ppAA NPs are regarded as highly attractive for applications where stability in aqueous media is of most significant concern.

2. For the synthesis of multicomponent and nanophase-separated thin films of plasma polymers:
   2.1. An approach to the synthesis of phase-separated plasma polymer nanocomposites was developed by the conjunction of two plasma-based techniques, with both of them remaining decoupled spatially from each other: the gas aggregation and the plasma-assisted vapor phase deposition. The glassy ppAA NPs were successfully embedded into the hydrogel-like

poly(ethylene oxide) (PEO) matrix. The deposition of an ultra-thin PEO capping layer was invented to prevent NP removal during the submersion into aqueous solution.

2.2. The spatially-resolved attachment of biomolecules onto the nanocomposite surface was achieved. When immersed into the solutions of lysozymes, these composites were found to accumulate the protein molecules at the sites where ppAA NPs reside, while the adsorption elsewhere was restrained. The selectivity of this process can be explained by electrostatic attraction between negative charge of dissociated carboxyls and positively charged lysozyme molecules in conjunction with the biorepellent nature of the PEO entities. The performance of the composite can be controlled by adjusting the number of embedded NPs and/or the thickness of the capping layer.

3. For the investigation of spatial confinement and segmental dynamics in plasma polymers:

3.1. A solvent-free plasma-based approach was developed to decorate the surface of PEO thin films with two-dimensional PE nano-islands. The methods with and without plasma assistance allowed for the synthesis of thin films of micro-phase separated plasma polymers.

3.2. The fundamental mechanisms were unveiled related to the macromolecular diffusion at the surface/vacuum interface, followed by the aggregation into nanoislands. The PE islands grow in the diffusion-limited aggregation regime and develop into isotropic fractals. The realization of the dendrite or fractal shape depends on the segmental freedom of PEO chains and can be tuned by the PEO thickness (at the same cross-link density) or by the cross-link density (at the same thickness).

3.3. The existence of the cluster-cluster aggregation regime at the polymer/polymer interface is intriguing, yet more substantial evidence is still required.

Bibliography

[1] A. D. Jenkins, R. F. T. Stepto, P. Kratochvíl, U. W. Suter. Glossary of basic terms in polymer science (IUPAC Recommendations 1996). *Pure Appl. Chem.*, 1996, vol. 68, no. 12, pp. 2287.

[2] J. Friedrich. Mechanisms of Plasma Polymerization - Reviewed from a Chemical Point of View. *Plasma Process. Polym.*, 2011, vol. 8, no. 9, pp. 783.

[3] J. Goodman. The formation of thin polymer films in the gas discharge. *J. Polym. Sci.*, 1960, vol. 44, no. 144, pp. 551.

[4] H. Yasuda. Plasma Polymerization. *Academic Press: New York,*1985.

[5] H. Biederman, Y. Osada. Plasma Polymerization Processes (Plasma Technology). *Elsevier: Amsterdam, Netherlands,*1992.

[6] H. Biederman. Plasma Polymer Films. *Imperial College Press: London, United Kingdom,* 2004.

[7] T. Williams, M. W. Hayes. Formation of Thin Polymer Films in a Glow Discharge. *Nature*, 1967, vol. 216, no. 5115, pp. 614.

[8] L. F. Thompson, G. Smolinsky. A scanning electron microscope study of plasma-polymerized organosilicon films suitable for use as lightguides. A determination of the cause of signal attenuation. *J. Appl. Polym. Sci.*, 1972, vol. 16, no. 5, pp. 1179.

[9] S. V. Vladimirov, K. Ostrikov. Self-Organization and Dynamics of Nanoparticles in Chemically Active Plasmas for Low-Temperature Deposition of Silicon and Carbon-Based Nanostructured Films. *Plasmas Polym.*, 2003, vol. 8, no. 2, pp. 135.

[10] L. Boufendi, A. Bouchoule. Particle nucleation and growth in a low-pressure argon-silane discharge. *Plasma Sources Sci. Technol.*, 1994, vol. 3, no. 3, pp. 262.

[11] K. G. Melikhov, A. M. Shterenberg, V. I. Zyn. Formation of surface relief in plasma polymerized films. *J. Phys. D. Appl. Phys.*, 2006, vol. 39, no. 5, pp. 944.

[12] M. Mao, J. Benedikt, A. Consoli, A. Bogaerts. New pathways for nanoparticle formation in acetylene dusty plasmas: A modelling investigation and comparison with experiments. *J. Phys. D. Appl. Phys.*, 2008, vol. 41, no. 22.

[13] C. Deschenaux, A. Affolter, D. Magni, C. Hollenstein, P. Fayet. Investigations of CH4, C2H2 and C2H4 dusty RF plasmas by means of FTIR absorption spectroscopy and mass spectrometry. *J. Phys. D. Appl. Phys.*, 1999, vol. 32, no. 15, pp. 1876.

[14] H. Kersten, H. Deutsch, E. Stoffels, W. W. Stoffels, R. Hippler. Micro-Disperse Particles in Plasmas. *Contrib. Plasma Phys*, 2001, vol. 41, no. 6, pp. 598.

[15] K. Takahashi, K. Tachibana. Solid particle production in fluorocarbon plasmas. I. Correlation with polymer film deposition. *J. Vac. Sci. Technol. A Vacuum, Surfaces, Film.*, 2001, vol. 19, no. 5, pp. 2055.

[16] D. O. H. Teare, C. G. Spanos, P. Ridley, E. J. Kinmond, V. Roucoules, J. P. S. Badyal, S. A. Brewer, S. Coulson, C. Willis. Pulsed plasma deposition of super-hydrophobic nanospheres. *Chem. Mater.*, 2002, vol. 14, no. 11, pp. 4566.

[17] G. D. Fu, E. T. Kang, K. G. Neoh. Deposition of Nanostructured Fluoropolymer Films on Silicon Substrates via Plasma Polymerization of Allylpentafluorobenzene. *J. Phys. Chem. B*, 2003, vol. 107, no. 50, pp. 13902.

[18] J. C. Feng, W. Huang, G. D. Fu, E.-T. Kang, K.-G. Neoh. Deposition of Well-Defined Fluoropolymer Nanospheres on PET Substrate by Plasma Polymerization of Heptadecafluorodecyl Acrylate and Their Potential Application as a Protective Layer. *Plasma Process. Polym.*, 2005, vol. 2, no. 2, pp. 127.

[19] S. H. Yang, C. H. Liu, W. T. Hsu, H. Chen. Preparation of super-hydrophobic films using pulsed hexafluorobenzene plasma. *Surf. Coatings Technol.*, 2009, vol. 203, no. 10–11, pp. 1379.

[20] A. R. Denaro, P. A. Owens, A. Crawshaw. Glow discharge polymerization-styrene. *Eur. Polym. J.*, 1968, vol. 4, no. 1, pp. 93.

[21] D. D. Neiswender. The Polymerization of Benzene in a Radiofrequency Discharge. *American Chemical Society*1969.

[22] H. Kobayashi, A. T. Bell, M. Shen. Formation of an amorphous powder during the polymerization of ethylene in a radio-frequency discharge. *J. Appl. Polym. Sci.*, 1973, vol. 17, no. 3, pp. 885.

[23] L. Boufendi, M. C. Jouanny, E. Kovacevic, J. Berndt, M. Mikikian. Dusty plasma for nanotechnology. *J. Phys. D. Appl. Phys.*, 2011, vol. 44, no. 17.

[24] J. Berndt, E. Kovačević, I. Stefanović, O. Stepanović, S. H. Hong, L. Boufendi, J. Winter. Some Aspects of Reactive Complex Plasmas. *Contrib. to Plasma Phys.*, 2009, vol. 49, no. 3, pp. 107.

[25] C. S. Diercks, O. M. Yaghi. The atom, the molecule, and the covalent organic framework. *Science (80-.).*, 2017, vol. 355, no. 6328.

[26] Y. Gu, J. Zhao, J. A. Johnson. A (Macro)Molecular-Level Understanding of Polymer Network Topology. *Trends Chem.*, 2019, vol. 1, no. 3, pp. 318.

[27] J. Bastide, L. Leibler. Large-Scale Heterogeneities in Randomly Cross-Linked Networks. *Macromolecules*, 1988, vol. 21, no. 8, pp. 2647.

[28] M. Shibayama. Small-angle neutron scattering on polymer gels: Phase behavior, inhomogeneities and deformation mechanisms. *Polym. J.*, 2011, vol. 43, no. 1, pp. 18.

[29] F. Di Lorenzo, S. Seiffert. Nanostructural heterogeneity in polymer networks and gels. *Polym. Chem.*, 2015, vol. 6, no. 31, pp. 5515.

[30] A. Fridman. Plasma Chemistry. *Cambridge University Press*, *Cambridge*, 2008.

[31] F. Paschen. Ueber die zum Funkenübergang in Luft, Wasserstoff und Kohlensäure bei verschiedenen Drucken erforderliche Potentialdifferenz. *Ann. Phys.*, 1889, vol. 273, no. 5, pp. 69.

[32] H. S. Butler, G. S. Kino. Plasma sheath formation by radio-frequency fields. *Phys. Fluids*, 1963, vol. 6, no. 9, pp. 1346.

[33] A. R. Denaro, P. A. Owens, A. Crawshaw. Glow discharge polymerization-III. Allyl alcohol and crotyl alcohol. *Eur. Polym. J.*, 1970, vol. 6, no. 3, pp. 487.

[34] A. R. Denaro, P. A. Owens, A. Crawshaw. Glow discharge polymerization-II α-methylstyrene, ω-methylstyrene and allylbenzene. *Eur. Polym. J.*, 1969, vol. 5, no. 4, pp. 471.

[35] A. R. Westwood. Glow discharge polymerization—I. Rates and mechanisms of polymer formation. *Eur. Polym. J.*, 1971, vol. 7, no. 4, pp. 363.

[36] H. U. Poll, M. Arzt, K. H. Wickleder. Reaction kinetics in the polymerization of thin films on the electrodes of a glow-discharge gap. *Eur. Polym. J.*, 1976, vol. 12, no. 8, pp. 505.

[37] D. K. Lam, R. F. Baddour, A. F. Stancell. A Mechanisms and Kinetics Study of Polymeric Thin-Film Deposition in Glow Discharge. *J. Macromol. Sci. Part A - Chem.*, 1976, vol. 10, no. 3, pp. 421.

[38] J. M. Tibbitt, R. Jensen, A. T. Bell, M. Shen. A Model for the Kinetics of Plasma Polymerization. *Macromolecules*, 1977, vol. 10, no. 3, pp. 647.

[39] H. Yasuda, T. Hsu. Plasma polymerization investigated by the comparison of hydrocarbons and perfluorocarbons. *Surf. Sci.*, 1978, vol. 76, no. 1, pp. 232.

[40] R. d'Agostino, F. Cramarossa, V. Colaprico, R. D'Ettole. Mechanisms of etching and polymerization in radiofrequency discharges of CF4–H2, CF4–C2F4, C2F6–H2, C3F8–H2. *J. Appl. Phys.*, 1983, vol. 54, no. 3, pp. 1284.

[41] A. Michelmore, D. A. Steele, J. D. Whittle, J. W. Bradley, R. D. Short. Nanoscale deposition of chemically functionalised films via plasma polymerisation. *RSC Adv.*, 2013, vol. 3, no. 33, pp. 13540.

[42] D. Barton, A. G. Shard, R. D. Short, J. W. Bradley. The effect of positive ion energy on plasma polymerization: A comparison between acrylic and propionic acids. *J. Phys. Chem. B*, 2005, vol. 109, no. 8, pp. 3207.

[43] A. Michelmore, J. D. Whittle, J. W. Bradley, R. D. Short. Where physics meets chemistry: Thin film deposition from reactive plasmas. *Front. Chem. Sci. Eng.*, 2016, vol. 10, no. 4, pp. 441.

[44] M. Ohring. The Materials Science of Thin Films. *Academic Press*1992.

[45] T. A. Witten, L. M. Sander. Diffusion-limited aggregation, a kinetic critical phenomenon. *Phys. Rev. Lett.*, 1981, vol. 47, no. 19, pp. 1400.

[46] D. Kandel. Initial Stages of Thin Film Growth in the Presence of Island-Edge Barriers. *Phys. Rev. Lett.*, 1997, vol. 78, no. 3, pp. 499.

[47] J. A. Venables, H. Brune. Capture numbers in the presence of repulsive adsorbate interactions. *Phys. Rev. B - Condens. Matter Mater. Phys.*, 2002, vol. 66, no. 19, pp. 1.

[48] D. Kandel, E. Kaxiras. Surfactant Mediated Crystal Growth of Semiconductors. *Phys. Rev. Lett.*, 1995, vol. 75, no. 14, pp. 2742.

[49] G. Hlawacek, P. Puschnig, P. Frank, A. Winkler, C. Ambrosch-Draxl, C. Teichert. Characterization of Step-Edge Barriers in Organic Thin-Film Growth. *Science (80-.).*, 2008, vol. 321, no. 5885, pp. 108.

[50] L. Tumbek, A. Winkler. Attachment limited versus diffusion limited nucleation of organic molecules: Hexaphenyl on sputter-modified mica. *Surf. Sci.*, 2012, vol. 606, no. 15–16, pp. L55.

[51] P. Meakin. Structure of the active zone in diffusion-limited aggregation, cluster-cluster aggregation, and the screened-growth model. *Phys. Rev. A*,

1985, vol. 32, no. 1, pp. 453.

[52] R. Jullien, M. Kolb, R. Botet. Aggregation by kinetic clustering of clusters in dimensions d > 2. *J. Phys. Lett.*, 1984, vol. 45, no. 5, pp. 211.

[53] J. Májek. Fractal Growth of Polyethylene Nanoislands on Polyethylene Oxide Thin Films. Bachelor's Thesis, 2019.

[54] J. B. Clarke, J. W. Hastie, L. H. E. Kihlborg, R. Metselaar, M. M. Thackeray. Definitions of terms relating to phase transitions of the solid state (IUPAC Recommendations 1994). *Pure Appl. Chem.*, 1994, vol. 66, no. 3, pp. 577.

[55] J. E. Mark. Physical Properties of Polymers Handbook. *American Institute Of Physics: New York*1996.

[56] I. S. Gutzow, O. V Mazurin, J. W. P. Schmelzer, S. V Todorova, B. B. Petroff, A. I. Priven. Glasses and the Glass Transition. *Wiley,*2011.

[57] I. M. Kalogeras. Glass-Transition Phenomena in Polymer Blends in Encycl. Polym. Blends, *John Wiley & Sons, Ltd*, 2016, pp. 1–134.

[58] E. Brener, H. Müller-Krumbhaar, D. Temkin. Kinetic Phase Diagram and Scaling Relations for Stationary Diffusional Growth. *Europhys. Lett.*, 1992, vol. 17, no. 6, pp. 535.

[59] O. Kylián, A. Choukourov, H. Biederman. Nanostructured plasma polymers. *Thin Solid Films*, 2013, vol. 548, , pp. 1.

[60] A. Choukourov, P. Pleskunov, D. Nikitin, V. Titov, A. Shelemin, M. Vaidulych, A. Kuzminova, P. Solar, J. Hanuš, J. Kousal, O. Kylián, D. Slavínská, H. Biederman. Advances and challenges in the field of plasma polymer nanoparticles. *Beilstein J. Nanotechnol.*, 2017, vol. 8, no. 1, pp. 2002.

[61] C. Stewart, B. Akhavan, S. G. Wise, M. M. M. Bilek. A review of biomimetic surface functionalization for bone-integrating orthopedic implants: Mechanisms, current approaches, and future directions. *Prog. Mater. Sci.*, 2019, vol. 106, no. July, pp. 100588.

[62] J. D. Whittle, R. D. Short, D. A. Steele, J. W. Bradley, P. M. Bryant, F. Jan, H. Biederman, A. A. Serov, A. Choukurov, A. L. Hook, W. A. Ciridon, G. Ceccone, D. Hegemann, E. Körner, A. Michelmore. Variability in Plasma Polymerization Processes - An International Round-Robin Study. *Plasma Process. Polym.*, 2013, vol. 10, no. 9, pp. 767.

[63] A. Valsesia, P. Colpo, M. Manso Silvan, T. Meziani, G. Ceccone, F. Rossi. Fabrication of Nanostructured Polymeric Surfaces for Biosensing Devices.

Nano Lett., 2004, vol. 4, no. 6, pp. 1047.

[64] K. S. Siow, L. Britcher, S. Kumar, H. J. Griesser. Plasma methods for the generation of chemically reactive surfaces for biomolecule immobilization and cell colonization - A review. *Plasma Process. Polym.*, 2006, vol. 3, no. 6–7, pp. 392.

[65] M. Donegan, D. P. Dowling. Protein adhesion on water stable atmospheric plasma deposited acrylic acid coatings. *Surf. Coatings Technol.*, 2013, vol. 234, , pp. 53.

[66] L. Detomaso, R. Gristina, G. S. Senesi, R. D'Agostino, P. Favia. Stable plasma-deposited acrylic acid surfaces for cell culture applications. *Biomaterials*, 2005, vol. 26, no. 18, pp. 3831.

[67] O. Carton, D. Ben Salem, S. Bhatt, J. Pulpytel, F. Arefi-Khonsari. Plasma polymerization of acrylic acid by atmospheric pressure nitrogen plasma jet for biomedical applications. *Plasma Process. Polym.*, 2012, vol. 9, no. 10, pp. 984.

[68] H. Zhang, K. D. Brown, S. P. Lowe, G.-S. Liu, D. Steele, K. Abberton, M. Daniell. Acrylic Acid Surface-Modified Contact Lens for the Culture of Limbal Stem Cells. *Tissue Eng. Part A*, 2014, vol. 20, no. 11–12, pp. 1593.

[69] R. Jafari, M. Tatoulian, W. Morscheidt, F. Arefi-Khonsari. Stable plasma polymerized acrylic acid coating deposited on polyethylene (PE) films in a low frequency discharge (70 kHz). *React. Funct. Polym.*, 2006, vol. 66, no. 12, pp. 1757.

[70] D. Hegemann, E. Körner, S. Guimond. Plasma polymerization of acrylic acid revisited. *Plasma Process. Polym.*, 2009, vol. 6, no. 4, pp. 246.

[71] J. E. L. Buddy D. Ratner, Allan S. Hoffman, Frederick J. Schoen. Biomaterials Science: An Introduction to Materials in Medicine. *Academic Press*2004.

[72] B. Finke, K. Schröder, A. Ohl. Structure retention and water stability of microwave plasma polymerized films from allylamine and acrylic acid. *Plasma Process. Polym.*, 2009, vol. 6, no. SUPPL. 1, pp. 70.

[73] A. Fahmy, R. Mix, A. Schönhals, J. Friedrich. Structure of Plasma-Deposited Copolymer Films Prepared from Acrylic Acid and Styrene: Part I Dependence on the Duty Cycle. *Plasma Process. Polym.*, 2012, vol. 9, no. 3, pp. 273.

[74] A. Fahmy, R. Mix, A. Schönhals, J. Friedrich. Structure of Plasma-Deposited Copolymer Films Prepared from Acrylic Acid and Styrene: Part II Variation

of the Comonomer Ratio. *Plasma Process. Polym.*, 2013, vol. 10, no. 9, pp. 750.

[75] S. R. Peri, H. Kim, B. Akgun, J. Enlow, H. Jiang, T. J. Bunning, X. Li, M. D. Foster. Structure of copolymer films created by plasma enhanced chemical vapor deposition. *Polymer (Guildf).*, 2010, vol. 51, no. 17, pp. 3971.

[76] Z. Li, X. Gillon, E. M. Diallo, J. Pireaux, L. Houssiau. Synthesis of Copolymer Films by RF Plasma: Correlation Between Plasma Chemistry and Film Characteristics. *IEEE Trans. Plasma Sci.*, 2013, vol. 41, no. 3, pp. 518.

[77] R. Daw, S. Candan, A. J. Beck, A. J. Devlin, I. M. Brook, S. MacNeil, R. A. Dawson, R. D. Short. Plasma copolymer surfaces of acrylic acid/1,7 octadiene: Surface characterisation and the attachment of ROS 17/2.8 osteoblast-like cells. *Biomaterials*, 1998, vol. 19, no. 19, pp. 1717.

[78] E. Sardella, P. Favia, E. Dilonardo, L. Petrone, R. d'Agostino. PE-CVD of acid/base coatings from acrylic acid and allylamine vapours. *Plasma Process. Polym.*, 2007, vol. 4, no. SUPPL.1, pp. 781.

[79] D. Pesen, D. B. Haviland. Modulation of Cell Adhesion Complexes by Surface Protein Patterns. *ACS Appl. Mater. Interfaces*, 2009, vol. 1, no. 3, pp. 543.

[80] G. Mishra, C. D. Easton, S. L. McArthur. Physical vs Photolithographic Patterning of Plasma Polymers: An Investigation by ToF−SSIMS and Multivariate Analysis. *Langmuir*, 2010, vol. 26, no. 5, pp. 3720.

[81] E. Sardella, P. Favia, R. Gristina, M. Nardulli, R. D'Agostino. Plasma-Aided Micro- and Nanopatterning Processes for Biomedical Applications. *Plasma Process. Polym.*, 2006, vol. 3, no. 6-7, pp. 456.

[82] A. Choukourov, I. Gordeev, J. Ponti, C. Uboldi, I. Melnichuk, M. Vaidulych, J. Kousal, D. Nikitin, L. Hanyková, I. Krakovský, D. Slavínská, H. Biederman. Microphase-Separated PE/PEO Thin Films Prepared by Plasma-Assisted Vapor Phase Deposition. *ACS Appl. Mater. Interfaces*, 2016, vol. 8, no. 12, pp. 8201.

[83] O. Polonskyi, O. Kylián, P. Solař, A. Artemenko, J. Kousal, D. Slavínská, A. Choukourov, H. Biederman. Nylon-sputtered nanoparticles: fabrication and basic properties. *J. Phys. D. Appl. Phys.*, 2012, vol. 45, no. 49, pp. 495301.

[84] M. Santos, P. L. Michael, E. C. Filipe, A. H. P. Chan, J. Hung, R. P. Tan, B. S. L. Lee, M. Huynh, C. Hawkins, A. Waterhouse, M. M. M. Bilek, S. G.

Wise. Plasma Synthesis of Carbon-Based Nanocarriers for Linker-Free Immobilization of Bioactive Cargo. *ACS Appl. Nano Mater.*, 2018, pp. acsanm.7b00086.

[85] A. H. Pfund. Bismuth black and its applications. *Rev. Sci. Instrum.*, 1930, vol. 1, no. 7, pp. 397.

[86] H. Haberland, M. Karrais, M. Mall. A new type of cluster and cluster ion source. *Zeitschrift für Phys. D Atoms, Mol. Clust.*, 1991, vol. 20, no. 1, pp. 413.

[87] Y. Huttel, Ed. . Gas-Phase Synthesis of Nanoparticles. *Wiley-VCH*, *Weinheim*, 2017.

[88] J. Kousal, A. Shelemin, M. Schwartzkopf, O. Polonskyi, J. Hanuš, P. Solař, M. Vaidulych, D. Nikitin, P. Pleskunov, Z. Krtouš, T. Strunskus, F. Faupel, S. V. Roth, H. Biederman, A. Choukourov. Magnetron-sputtered copper nanoparticles: lost in gas aggregation and found by in situ X-ray scattering. *Nanoscale*, 2018, vol. 10, no. 38, pp. 18275.

[89] A. Shelemin, P. Pleskunov, J. Kousal, J. Drewes, J. Hanuš, S. Ali-Ogly, D. Nikitin, P. Solař, J. Kratochvíl, M. Vaidulych, M. Schwartzkopf, O. Kylián, O. Polonskyi, T. Strunskus, F. Faupel, S. V. Roth, H. Biederman, A. Choukourov. Nucleation and Growth of Magnetron-Sputtered Ag Nanoparticles as Witnessed by Time-Resolved Small Angle X-Ray Scattering. *Part. Part. Syst. Charact.*, 2020, vol. 37, no. 2, pp. 1.

[90] J. Zhao, E. Baibuz, J. Vernieres, P. Grammatikopoulos, V. Jansson, M. Nagel, S. Steinhauer, M. Sowwan, A. Kuronen, K. Nordlund, F. Djurabekova. Formation Mechanism of Fe Nanocubes by Magnetron Sputtering Inert Gas Condensation. *ACS Nano*, 2016, vol. 10, no. 4, pp. 4684.

[91] F. R. Negreiros, A. Halder, C. Yin, A. Singh, G. Barcaro, L. Sementa, E. C. Tyo, M. J. Pellin, S. Bartling, K.-H. Meiwes-Broer, S. Seifert, P. Sen, S. Nigam, C. Majumder, N. Fukui, H. Yasumatsu, S. Vajda, A. Fortunelli. Bimetallic Ag-Pt Sub-nanometer Supported Clusters as Highly Efficient and Robust Oxidation Catalysts. *Angew. Chemie Int. Ed.*, 2018, vol. 57, no. 5, pp. 1209.

[92] Y.-H. Xu, J.-P. Wang. Direct Gas-Phase Synthesis of Heterostructured Nanoparticles through Phase Separation and Surface Segregation. *Adv. Mater.*, 2008, vol. 20, no. 5, pp. 994.

[93] R. Bitar, P. Cools, N. De Geyter, R. Morent. Acrylic acid plasma polymerization for biomedical use. *Appl. Surf. Sci.*, 2018, vol. 448, , pp. 168.

[94] V. L. Mironov. Fundamentals of scanning probe microscopy. 2004, pp. 97.

[95] I. Khalakhan, A. Choukourov, M. Vorokhta, P. Kúš, I. Matolínová, V. Matolín. In situ electrochemical AFM monitoring of the potential-dependent deterioration of platinum catalyst during potentiodynamic cycling. *Ultramicroscopy*, 2018, vol. 187, , pp. 64.

[96] D. Briggs, J. T. Grant, S. Limited. Surface Analysis by Auger and X-Ray Photoelectron Spectroscopy. *SurfaceSpectra*2003.

[97] J. W. Cooley, J. W. Tukey. An Algorithm for the Machine Calculation of Complex Fourier Series. *Math. Comput.*, 1965, vol. 19, no. 90, pp. 297.

[98] A. Dazzi, C. B. Prater. AFM-IR: Technology and applications in nanoscale infrared spectroscopy and chemical imaging. *Chem. Rev.*, 2017, vol. 117, no. 7, pp. 5146.

[99] J. B. Baxter, G. W. Guglietta. Terahertz spectroscopy. *Anal. Chem.*, 2011, vol. 83, no. 12, pp. 4342.

[100] E. P. J. Parrott, J. A. Zeitler. Terahertz time-domain and low-frequency Raman spectroscopy of organic materials. *Appl. Spectrosc.*, 2015, vol. 69, no. 1, pp. 1.

[101] "Xensor Integration BV," https://xensor.nl/, accessed 18.07.2020.

[102] S. Madkou, I. Melnichu, A. Choukourov, I. Krakovsky, H. Biederman, A. Schönhals. In Situ Nanocalorimetric Investigations of Plasma Assisted Deposited Poly(ethylene oxide)-like Films by Specific Heat Spectroscopy. *J. Phys. Chem. B*, 2016, vol. 120, no. 16, pp. 3954.

[103] C. S. H. Huth, A. A. Minakov. Differential AC-Chip Calorimeter for Glass Transition Measurements in Ultrathin Films. *J. Polym. Sci. Part B Polym. Phys.*, 2006, vol. 44, , pp. 2996.

[104] S. Madkour, H. Yin, M. Füllbrandt, A. Schönhals. Calorimetric evidence for a mobile surface layer in ultrathin polymeric films: poly(2-vinyl pyridine). *Soft Matter*, 2015, vol. 11, no. 40, pp. 7942.

[105] H. Fujiwara. Spectroscopic Ellipsometry: Principles and Applications. 2007.

[106] B. J. Kirby, E. F. Hasselbrink. Zeta potential of microfluidic substrates: 1. Theory, experimental techniques, and effects on separations. *Electrophoresis*, 2004, vol. 25, no. 2, pp. 187.

[107] A. Sze, D. Erickson, L. Ren, D. Li. Zeta-potential measurement using the Smoluchowski equation and the slope of the current-time relationship in electroosmotic flow. *J. Colloid Interface Sci.*, 2003, vol. 261, no. 2, pp. 402.

[108] Y. Pihosh, H. Biederman, D. Slavinska, J. Kousal, A. Choukourov, M. Trchova, A. Mackova, A. Boldyreva. Composite SiOx/hydrocarbon plasma polymer films prepared by RF magnetron sputtering of SiO2 and polyethylene or polypropylene. *Vacuum*, 2006, vol. 81, no. 1, pp. 32.

[109] A. Choukouro, I. Gordeev, O. Polonskyi, A. Artemenko, L. Hanyková, I. Krakovský, O. Kylián, D. Slavínská, H. Biederman. Polyethylene (ethylene oxide)-like plasma polymers produced by plasma-assisted vacuum evaporation. *Plasma Process. Polym.*, 2010, vol. 7, no. 6, pp. 445.

[110] K. Takahashi, K. Tachibana. Solid particle production in fluorocarbon plasmas. I. Correlation with polymer film deposition. *J. Vac. Sci. Technol. A Vacuum, Surfaces, Film.*, 2001, vol. 19, no. 5, pp. 2055.

[111] P. Solař, O. Polonskyi, A. Choukourov, A. Artemenko, J. Hanuš, H. Biederman, D. Slavínská. Nanostructured thin films prepared from cluster beams. *Surf. Coatings Technol.*, 2011, vol. 205, , pp. S42.

[112] V. Massereau-Guilbaud, I. Geraud-Grenier, J. Lagrange, H. Tawidian, M. Mikikian. Electron Temperature Evolution in a Low-Pressure Dusty RF Nitrogen-Rich Methane Plasma. *IEEE Trans. Plasma Sci.*, 2013, vol. 41, no. 4, pp. 816.

[113] M. Hundt, P. Sadler, I. Levchenko, M. Wolter, H. Kersten, K. (Ken) Ostrikov. Real-time monitoring of nucleation-growth cycle of carbon nanoparticles in acetylene plasmas. *J. Appl. Phys.*, 2011, vol. 109, no. 12, pp. 123305.

[114] A. Garscadden. Nucleation, growth, and morphology of dust in plasmas. *Pure Appl. Chem.*, 1994, vol. 66, no. 6, pp. 1319.

[115] A. Choukourov, A. Shelemin, P. Pleskunov, D. Nikitin, I. Khalakhan, J. Hanuš. Nanoscale morphogenesis of nylon-sputtered plasma polymer particles. *J. Phys. D. Appl. Phys.*, 2018, vol. 51, no. 21, pp. 215304.

[116] E. Kovacevic, J. Berndt, T. Strunskus, L. Boufendi. Size dependent characteristics of plasma synthesized carbonaceous nanoparticles. *J. Appl. Phys.*, 2012, vol. 112, no. 1, pp. 013303.

[117] A. M. Hinz, E. von Wahl, F. Faupel, T. Strunskus, H. Kersten. Versatile particle collection concept for correlation of particle growth and discharge

parameters in dusty plasmas. *J. Phys. D. Appl. Phys.*, 2015, vol. 48, no. 5, pp. 055203.

[118] A. Shelemin, D. Nikitin, A. Choukourov, O. Kylián, J. Kousal, I. Khalakhan, I. Melnichuk, D. Slavínská, H. Biederman. Preparation of biomimetic nano-structured films with multi-scale roughness. *J. Phys. D. Appl. Phys.*, 2016, vol. 49, no. 25, pp. 254001.

[119] M. G. Olayo, R. Zúñiga, F. González-Salgado, L. M. Gómez, M. González-Torres, R. Basurto, G. J. Cruz. Structure and morphology of plasma polyfuran particles. *Polym. Bull.*, 2017, vol. 74, no. 2, pp. 571.

[120] C. Pattyn, E. Kovacevic, S. Hussain, A. Dias, T. Lecas, J. Berndt. Nanoparticle formation in a low pressure argon/aniline RF plasma. *Appl. Phys. Lett.*, 2018, vol. 112, no. 1, pp. 013102.

[121] A. Fahmy, T. a. Mohamed, A. Schönhals. Structure of Plasma Poly(Acrylic Acid): Influence of Pressure and Dielectric Properties. *Plasma Chem. Plasma Process.*, 2015, vol. 35, no. 2, pp. 303.

[122] P. Cools, E. Sainz-García, N. De Geyter, A. Nikiforov, M. Blajan, K. Shimizu, F. Alba-Elías, C. Leys, R. Morent. Influence of DBD Inlet Geometry on the Homogeneity of Plasma-Polymerized Acrylic Acid Films: The Use of a Microplasma-Electrode Inlet Configuration. *Plasma Process. Polym.*, 2015, vol. 12, no. 10, pp. 1153.

[123] L. O'Toole, A. J. Beck, R. D. Short. Characterization of plasma polymers of acrylic acid and propanoic acid. *Macromolecules*, 1996, vol. 29, no. 15, pp. 5172.

[124] L. O'Toole, A. J. Beck, A. P. Ameen, F. R. Jones, R. D. Short. Radiofrequency-induced plasma polymerisation of propenoic acid and propanoic acid. *J. Chem. Soc. Faraday Trans.*, 1995, vol. 91, no. 21, pp. 3907.

[125] M. R. Alexander, T. M. Duc. The chemistry of deposits formed from acrylic acid plasmas. *J. Mater. Chem.*, 1998, vol. 8, no. 4, pp. 937.

[126] D. Lin-Vien, N. B. Colthup, W. G. Fateley, J. G. (Professor) Grasselli. The Handbook of Infrared and Raman Characteristic Frequencies of Organic Molecules. *Academic Press,* 1991.

[127] J. C. Leyte, L. H. Zuiderweg, H. J. Vledder. An i.r. investigation of polyion-counterion interactions. *Spectrochim. Acta Part A Mol. Spectrosc.*, 1967, vol. 23, no. 5, pp. 1397.

[128] L. Bardet, G. Cassanas-Fabre, M. Alain. Étude de la transition conformationnelle de l'acide polyacrylique syndiotactique en solution aqueuse par spectroscopie de vibration. *J. Mol. Struct.*, 1975, vol. 24, no. 1, pp. 153.

[129] S. Zanini, R. Ziano, C. Riccardi. Stable poly(Acrylic Acid) films from acrylic acid/argon plasmas: Influence of the mixture composition and the reactor geometry on the thin films chemical structures. *Plasma Chem. Plasma Process.*, 2009, vol. 29, no. 6, pp. 535.

[130] R. Morent, N. De Geyter, M. Trentesaux, L. Gengembre, P. Dubruel, C. Leys, E. Payen. Stability study of polyacrylic acid films plasma-polymerized on polypropylene substrates at medium pressure. *Appl. Surf. Sci.*, 2010, vol. 257, no. 2, pp. 372.

[131] M. Bauer, T. Schwarz-Selinger, H. Kang, A. Von Keudell. Control of the plasma chemistry of a pulsed inductively coupled methane plasma. *Plasma Sources Sci. Technol.*, 2005, vol. 14, no. 3, pp. 543.

[132] Y.-R. Luo. Handbook of Bond Dissociation Energies in Organic Compounds. *CRC Press*2003.

[133] M. Pelliccione, T.-M. Lu. Evolution of Thin Film Morphology. *Springer New York*, *New York, NY*, 2008.

[134] S. A. Voronin, M. Zelzer, C. Fotea, M. R. Alexander, J. W. Bradley. Pulsed and continuous wave acrylic acid radio frequency plasma deposits: Plasma and surface chemistry. *J. Phys. Chem. B*, 2007, vol. 111, no. 13, pp. 3419.

[135] J. Kousal, A. Kolpaková, A. Shelemin, P. Kudrna, M. Tichý, O. Kylián, J. Hanuš, A. Choukourov, H. Biederman. Monitoring of conditions inside gas aggregation cluster source during production of Ti/TiO x nanoparticles. *Plasma Sources Sci. Technol.*, 2017, vol. 26, no. 10, pp. 105003.

[136] S. Fraser, R. D. Short, D. Barton, J. W. Bradley. A multi-technique investigation of the pulsed plasma and plasma polymers of acrylic acid: Millisecond pulse regime. *J. Phys. Chem. B*, 2002, vol. 106, no. 22, pp. 5596.

[137] R. D. Short, D. A. Steele. Testing the Hypothesis: Comments on Plasma Polymerisation of Acrylic Acid Revisited. *Plasma Process. Polym.*, 2010, vol. 7, no. 5, pp. 366.

[138] J. P. Booth, G. Cunge, N. Sadeghi, R. W. Boswell. The transition from symmetric to asymmetric discharges in pulsed 13.56 MHz capacitively coupled plasmas. *J. Appl. Phys.*, 1997, vol. 82, no. 2, pp. 552.

[139] S. A. Voronin, M. R. Alexander, J. W. Bradley. Time-resolved mass and energy spectral investigation of a pulsed polymerising plasma struck in acrylic acid. *Surf. Coatings Technol.*, 2006, vol. 201, no. 3–4, pp. 768.

[140] D. Barton, A. G. Shard, R. D. Short, J. W. Bradley. The effect of positive ion energy on plasma polymerization: A comparison between acrylic and propionic acids. *J. Phys. Chem. B*, 2005, vol. 109, no. 8, pp. 3207.

[141] I. Swindells, S. A. Voronin, C. Fotea, M. R. Alexander, J. W. Bradley. Detection of Negative Molecular Ions in Acrylic Acid Plasma: Some Implications for Polymerization Mechanisms. *J. Phys. Chem. B*, 2007, vol. 111, no. 30, pp. 8720.

[142] I. Swindells, S. A. Voronin, P. M. Bryant, M. R. Alexander, J. W. Bradley. Temporal Evolution of an Electron-Free Afterglow in the Pulsed Plasma Polymerisation of Acrylic Acid. *J. Phys. Chem. B*, 2008, vol. 112, no. 13, pp. 3938.

[143] E. Marotta, C. Paradisi. Positive ion chemistry of esters of carboxylic acids in air plasma at atmospheric pressure. *J. Mass Spectrom.*, 2005, vol. 40, no. 12, pp. 1583.

[144] F. Moix, K. McKay, J. L. Walsh, J. W. Bradley. Atmospheric-Pressure Plasma Polymerization of Acrylic Acid: Gas-Phase Ion Chemistry. *Plasma Process. Polym.*, 2016, vol. 13, no. 2, pp. 236.

[145] D. Nikitin, S. Madkour, P. Pleskunov, R. Tafiichuk, A. Shelemin, J. Hanuš, I. Gordeev, E. Sysolyatina, A. Lavrikova, S. Ermolaeva, V. Titov, A. Schönhals, A. Choukourov. Cu nanoparticles constrain segmental dynamics of cross-linked polyethers: a trade-off between non-fouling and antibacterial properties. *Soft Matter*, 2019, vol. 15, no. 13, pp. 2884.

[146] Y. Park, S. Lee, S. S. Ha, B. Alunda, D. Y. Noh, Y. J. Lee, S. Kim, J. H. Seol. Crosslinking Effect on Thermal Conductivity of Electrospun Poly(acrylic acid) Nanofibers. *Polymers (Basel).*, 2019, vol. 11, no. 5, pp. 858.

[147] K. Saalwächter, S. Seiffert. Dynamics-based assessment of nanoscopic polymer-network mesh structures and their defects. *Soft Matter*, 2018, vol. 14, no. 11, pp. 1976.

[148] A. Kulbida, M. N. Ramos, M. Rasanen, J. Nieminen, O. Schrems, R. Fausto. Rotational isomerism in acrylic acid. A combined matrix-isolated IR, Raman and ab initio molecular orbital study. *J. Chem. Soc. Faraday Trans.*, 1995, vol.

91, no. 11, pp. 1571.

[149] C. Murli, Y. Song. Pressure-Induced polymerization of acrylic acid: A raman spectroscopic study. *J. Phys. Chem. B*, 2010, vol. 114, no. 30, pp. 9744.

[150] S. van Herwaaden. Application Note for Xsensor's Calorimtere Chips of XEN-39390 Series. n.d.

[151] A. Choukourov, I. Gordeev, D. Arzhakov, A. Artemenko, J. Kousal, O. Kylián, D. Slavínská, H. Biederman. Does cross-link density of PEO-like plasma polymers influence their resistance to adsorption of fibrinogen?. *Plasma Process. Polym.*, 2012, vol. 9, no. 1, pp. 48.

[152] S. Bhatt, J. Pulpytel, G. Ceccone, P. Lisboa, F. Rossi, V. Kumar, F. Arefi-Khonsari. Nanostructure Protein Repellant Amphiphilic Copolymer Coatings with Optimized Surface Energy by Inductively Excited Low Pressure Plasma. *Langmuir*, 2011, vol. 27, no. 23, pp. 14570.

[153] S. Bhatt, J. Pulpytel, F. Arefi-Khonsari. Low and atmospheric plasma polymerisation of nanocoatings for bio-applications. *Surf. Innov.*, 2015, vol. 3, no. 2, pp. 63.

[154] I. Muzammil, Y. Li, M. Lei. Tunable wettability and pH-responsiveness of plasma copolymers of acrylic acid and octafluorocyclobutane. *Plasma Process. Polym.*, 2017, vol. 14, no. 10, pp. 1700053.

[155] I. Muzammil, Y. P. Li, X. Y. Li, M. K. Lei. Duty cycle dependent chemical structure and wettability of RF pulsed plasma copolymers of acrylic acid and octafluorocyclobutane. *Appl. Surf. Sci.*, 2018, vol. 436, , pp. 411.

[156] O. Carton, D. Ben Salem, J. Pulpytel, F. Arefi-Khonsari. Improvement of the Water Stability of Plasma Polymerized Acrylic Acid/MBA Coatings Deposited by Atmospheric Pressure Air Plasma Jet. *Plasma Chem. Plasma Process.*, 2015, vol. 35, no. 5, pp. 819.

[157] J. J. Knobloch, H. J. Askew, K. L. Jarvis, R. Jones, J. G. Shapter, S. L. McArthur, I. Köper. In situ monitoring of the effect of ionic strength and pH on plasma polymer thin films. *Plasma Process. Polym.*, 2017, vol. 14, no. 11, pp. 1700084.

[158] P. Cools, H. Declercq, N. De Geyter, R. Morent. A stability study of plasma polymerized acrylic acid films. *Appl. Surf. Sci.*, 2018, vol. 432, , pp. 214.

[159] P. Rivolo, R. Nisticò, F. Barone, M. G. Faga, D. Duraccio, S. Martorana, S. Ricciardi, G. Magnacca. Study of the adhesive properties versus

stability/aging of hernia repair meshes after deposition of RF activated plasma polymerized acrylic acid coating. *Mater. Sci. Eng. C*, 2016, vol. 65, , pp. 287.

[160] A. Choukourov, I. Melnichuk, I. Gordeev, O. Kylián, J. Hanuš, J. Kousal, P. Solař, L. Hanyková, J. Brus, D. Slavínská, H. Biederman. Dynamic scaling and kinetic roughening of poly(ethylene) islands grown by vapor phase deposition. *Thin Solid Films*, 2014, vol. 565, , pp. 249.

[161] Y. Sawada, A. Dougherty, J. P. Gollub. Dendritic and Fractal Patterns in Electrolytic Metal Deposits. *Phys. Rev. Lett.*, 1986, vol. 56, no. 12, pp. 1260.

[162] D. Grier, E. Ben-Jacob, R. Clarke, L. M. Sander. Morphology and Microstructure in Electrochemical Deposition of Zinc. *Phys. Rev. Lett.*, 1986, vol. 56, no. 12, pp. 1264.

[163] T. A. Witten, L. M. Sander. Diffusion-limited aggregation. *Phys. Rev. B*, 1983, vol. 27, no. 9, pp. 5686.

[164] S. Ogura, K. Fukutani, M. Matsumoto, T. Okano, M. Okada, T. Kawamura. Dendritic to non-dendritic transitions in Au islands investigated by scanning tunneling microscopy and Monte Carlo simulations. *Phys. Rev. B - Condens. Matter Mater. Phys.*, 2006, vol. 73, no. 12, pp. 4.

[165] G. Ehrlich, F. G. Hudda. Atomic View of Surface Self-Diffusion: Tungsten on Tungsten. *J. Chem. Phys.*, 1966, vol. 44, no. 3, pp. 1039.

[166] H. Brune, C. Romainczyk, H. Röder, K. Kern. Mechanism of the transition from fractal to dendritic growth of surface aggregates. *Nature*, 1994, vol. 369, no. 6480, pp. 469.

[167] H. Brune. Microscopic view of epitaxial metal growth: nucleation and aggregation. *Surf. Sci. Rep.*, 1998, vol. 31, no. 4–6, pp. 125.

[168] J. Nittmann, H. E. Stanley. Tip splitting without interfacial tension and dendritic growth patterns arising from molecular anisotropy. *Nature*, 1986, vol. 321, no. 6071, pp. 663.

[169] J. R. Felts, K. Kjoller, M. Lo, C. B. Prater, W. P. King. Nanometer-scale infrared spectroscopy of heterogeneous polymer nanostructures fabricated by tip-based nanofabrication. *ACS Nano*, 2012, vol. 6, no. 9, pp. 8015.

[170] M. Kelchtermans, M. Lo, E. Dillon, K. Kjoller, C. Marcott. Characterization of a polyethylene-polyamide multilayer film using nanoscale infrared spectroscopy and imaging. *Vib. Spectrosc.*, 2016, vol. 82, , pp. 10.

[171] M. Sajid, G. U. Siddiqui, S. W. Kim, K. H. Na, Y. S. Choi, K. H. Choi.

Thermally modified amorphous polyethylene oxide thin films as highly sensitive linear humidity sensors. *Sensors Actuators, A Phys.*, 2017, vol. 265, , pp. 102.

[172] M. A. Rickard, G. F. Meyers, B. M. Habersberger, C. W. Reinhardt, J. J. Stanley. Nanoscale chemical imaging of a deuterium-labeled polyolefin copolymer in a polyolefin blend by atomic force microscopy-infrared spectroscopy. *Polymer (Guildf).*, 2017, vol. 129, , pp. 247.

[173] F. Tang, P. Bao, A. Roy, Y. Wang, Z. Su. In-situ spectroscopic and thermal analyses of phase domains in high-impact polypropylene. *Polymer (Guildf).*, 2018, vol. 142, , pp. 155.

[174] P. N. Tri, R. E. Prud'Homme. Nanoscale Lamellar Assembly and Segregation Mechanism of Poly(3-hydroxybutyrate)/Poly(ethylene glycol) Blends. *Macromolecules*, 2018, vol. 51, no. 1, pp. 181.

[175] T. R. Gengenbach, R. C. Chatelier, H. J. Griesser. Characterization of the Ageing of Plasmadeposited Polymer Films: Global Analysis of Xray Photoelectron Spectroscopy Data. *Surf. Interface Anal.*, 1996, vol. 24, no. 4, pp. 271.

[176] T. R. Gengenbach, R. C. Chatelier, H. J. Griesser. Correlation of the Nitrogen 1s and Oxygen 1s XPS Binding Energies with Compositional Changes During Oxidation of Ethylene Diamine Plasma Polymers. *Surf. Interface Anal.*, 1996, vol. 24, no. 9, pp. 611.

[177] T. R. Gengenbach, H. J. Griesser. Aging of 1,3-diaminopropane plasma-deposited polymer films: Mechanisms and reaction pathways. *J. Polym. Sci. Part A Polym. Chem.*, 1999, vol. 37, no. 13, pp. 2191.

[178] I. Kholodkov, H. Biederman, D. Slavínská, A. Choukourov, M. Trchova. Plasma polymers prepared by RF sputtering of polyethylene. *Vacuum*, 2003, vol. 70, no. 4, pp. 505.

[179] A. Choukourov, J. Hanuš, J. Kousal, A. Grinevich, Y. Pihosh, D. Slavínská, H. Biederman. Thin polymer films from polyimide vacuum thermal degradation with and without a glow discharge. *Vacuum*, 2006, vol. 80, no. 8, pp. 923.

[180] M. D. Ediger, J. A. Forrest. Dynamics near Free Surfaces and the Glass Transition in Thin Polymer Films: A View to the Future. *Macromolecules*, 2014, vol. 47, no. 2, pp. 471.

[181] S. Napolitano, M. Wübbenhorst. The lifetime of the deviations from bulk behaviour in polymers confined at the nanoscale. *Nat. Commun.*, 2011, vol. 2, no. 1, DOI 10.1038/ncomms1259.

[182] K. Dušek, A. Choukourov, M. Dušková-Smrčková, H. Biederman. Constrained Swelling of Polymer Networks: Characterization of Vapor-Deposited Cross-Linked Polymer Thin Films. *Macromolecules*, 2014, vol. 47, no. 13, pp. 4417.

[183] R. Botet, R. Jullien. Intrinsic anisotropy of clusters in cluster-cluster aggregation. *J. Phys. A Gen. Phys.*, 1986, vol. 19, no. 15.

[184] R. Jullien. Aggregation phenomena and fractal aggregates. *Contemp. Phys.*, 1987, vol. 28, no. 5, pp. 477.

[185] P. Meakin. Fractal aggregates. *Adv. Colloid Interface Sci.*, 1987, vol. 28, no. C, pp. 249.

[186] X. Wang, Y. Huang. Calculation of the fractal dimension of diffusion-limited aggregation by the renormalization-group approach in an arbitrary Euclidean dimension d. *Phys. Rev. A*, 1992, vol. 46, no. 8, pp. 5038.

[187] A. Ghosh, R. Batabyal, G. P. Das, B. N. Dev. An extended fractal growth regime in the diffusion limited aggregation including edge diffusion. *AIP Adv.*, 2016, vol. 6, no. 1.

List of Tables

List of Abbreviations

AA	acrylic acid
AC	alternating current
AFM	atomic force microscopy
AFM-IR	atomic force microscope infrared-spectroscopy
ALA	attachment limited aggregation
CW	continuous wave
DC	direct current
DLA	diffusion-limited aggregation
CCA	cluster-cluster aggregation
FTIR	Fourier-transform infrared spectroscopy
FC-AFM	fluid cell atomic force microscopy
GAS	gas aggregation cluster source
GPC	gel permeation chromatography
LSZ	lysozyme
MW	microwave
NMR	nuclear magnetic resonance
NPs	nanoparticles
PAVD	plasma-assisted vapor phase deposition
PBS	phosphate-buffered saline
PE	polyethylene
PEO	poly(ethylene oxide)
ppAA	AA plasma polymer
ppPE	PE plasma polymer
ppPEO	PEO plasma polymer
PRF	pulse repetition frequency
QCM	quartz crystal microbalance
RF	radio frequency
SEM	scanning electron microscopy
SHS	specific heat spectroscopy
THz-RS	THz-Raman spectroscopy
XPS	X-ray photoelectron spectroscopy

List of Publications

Reviewed international journals

1. D. Shutov, P. Bogdanov, **P. Pleskunov**. Destruction of Organic Dyes in Aqueous Solution by Low-Temperature Plasma Jet Treatment. *High Energy Chemistry*, vol. 50, no. 1, pp. 77-81, 2016.
2. A. Choukourov, **P. Pleskunov**, D. Nikitin, V. Titov, A. Shelemin, M. Vaidulych, A. Kuzminova, P. Solař, J. Hanuš, J. Kousal, O. Kylián, D. Slavínská, H. Biederman. Advances and challenges in the field of plasma polymer nanoparticles. *Beilstein Journal of Nanotechnology*, vol. 8, pp. 2002–2014, 2017.
3. **P. Pleskunov**, D. Nikitin, R. Tafiichuk, A. Shelemin, J. Hanuš, I. Khalakhan, A. Choukourov. Carboxyl-Functionalized Nanoparticles Produced by Pulsed Plasma Polymerization of Acrylic Acid. *J. Phys. Chem. B*, vol. 122, no. 14, pp. 4187-4194, 2018.
4. A. Choukourov, A. Shelemin, **P. Pleskunov**, D. Nikitin, I. Khalakhan, J. Hanuš. Nanoscale morphogenesis of nylon-sputtered plasma polymer particles. *Journal of Physics D: Applied Physics*, vol. 51, no. 21, 2018.
5. J. Kousal, A. Shelemin, M. Schwartzkopf, O. Polonskyi, J. Hanuš, P. Solař, M. Vaidulych, D. Nikitin, **P. Pleskunov**, Z. Krtouš, T. Strunskus, F. Faupel, S.V. Roth, H. Biederman, A. Choukourov. Magnetron-sputtered copper nanoparticles: lost in gas aggregation and found by in situ X-ray scattering. *Nanoscale*, vol. 10, no. 38, pp. 18275–18281, 2018.
6. M. Vaidulych, A. Shelemin, J. Hanuš, I. Khalakhan, I. Krakovsky, P. Kočová, H. Mašková, J. Kratochvíl, **P. Pleskunov**, J. Štěrba, O. Kylián, A. Choukourov, H. Biederman. Superwettable antibacterial textiles for versatile oil/water separation. *Plasma Process Polym*., vol. 16, no. 7, 2019.
7. A. Shelemin, D. Nikitin, **P. Pleskunov**, M. Vaidulych, R. Tafiichuk, A. Choukourov, P. Kúš, P. Solař, A. Kuzminova, O. Kylián, H. Biederman. Wetting on a-C:H coatings decorated with sub-micron structures. *Surf. Coatings Technol*., vol. 367, pp. 165–172, 2019.
8. D. Nikitin, S. Madkour, **P. Pleskunov**, R. Tafiichuk, A. Shelemin, J. Hanuš, I. Gordeev, E. Sysolyatina, A. Lavrikova, S. Ermolaeva, V. Titov, A. Schönhals. A. Choukourov. Cu nanoparticles constrain segmental dynamics of cross-linked

polyethers: a trade-off between non-fouling and antibacterial properties. *Soft Matter*, vol. 15, no, 13, 2884–2896, 2019.

9. I. Velichko, I. Gordeev, A. Shelemin, D. Nikitin, J. Brinar, **P. Pleskunov**, A. Choukourov, K. Pazderů, J. Pulkrábek. Plasma Jet and Dielectric Barrier Discharge Treatment of Wheat Seeds. *Plasma Chemistry and Plasma Processing*, vol. 39, no. 4, pp. 913–928, 2019.
10. A. Choukourov, **P. Pleskunov**, D. Nikitin, R.Tafiichuk, A. Shelemin, J. Hanuš, J. Májek, M. Unger, A. Roy, A. Ryabov. Plasma-assisted growth of polyethylene fractal nano-islands on polyethylene oxide films: Impact of film confinement and glassy dynamics on fractal morphologies. *Applied Surface Science*, vol. 489, pp. 55–65, 2019.
11. O. Kylián, A. Shelemin, P. Solař, **P. Pleskunov**, D. Nikitin, A. Kuzminova, R. Štefaníková, P. Kúš, M. Cieslar, J. Hanuš, A. Choukourov, H. Biederman. Magnetron Sputtering of Polymeric Targets: From Thin Films to Heterogeneous Metal/Plasma Polymer Nanoparticles. *Materials*, vol. 12, no. 15, 2019.
12. D. Nikitin, I. Lipatova, I. Naumova, N. Sirotkin, **P. Pleskunov**, I. Krakovský, I. Khalakhan, A. Choukourov, V. Titov, A. Agafonov. Immobilization of Chitosan Onto Polypropylene Foil via Air/Solution Atmospheric Pressure Plasma Afterglow Treatment. *Plasma Chemistry and Plasma Processing*, vol. 40, pp. 207–220, 2020.
13. A. Shelemin, **P. Pleskunov**, J. Kousal, J. Drewes, J. Hanuš, S. Ali-Ogly, D. Nikitin, P. Solar, J. Kratochvíl, M. Vaidulych, M. Schwartzkopf, O. Kylián, O. Polonskyi, T. Strunskus, F. Faupel, S. V. Roth, H. Biederman, and A. Choukourov. Nucleation and Growth of Magnetron-Sputtered Ag Nanoparticles as Witnessed by Time-Resolved Small Angle X-Ray Scattering. *Part. Syst. Charact*., vol. 37, no. 2, 2020.
14. **P. Pleskunov**, D. Nikitin, R. Tafiichuk, I. Khalakhan, Z. Kolská Z, A. Choukourov. Nanophase-separated poly(acrylic acid)/poly(ethylene oxide) plasma polymers for the spatially localized attachment of biomolecules. *Plasma Process Polym.*, vol. 17, no. 5, 2020.
15. **P. Pleskunov**, D. Nikitin, R. Tafiichuk, A. Shelemin, J. Hanuš, J. Kousal, Z. Krtouš, I. Khalakhan, P. Kúš, T. Nasu, T. Nagahama, C. Funaki, H. Sato, M. Gawek, A. Schoenhals, and A. Choukourov. Plasma Polymerization of Acrylic

Acid for the Tunable Synthesis of Glassy and Carboxylated Nanoparticles. *J. Phys. Chem. B*, vol. 124, no. 4, pp. 668–678, 2020.

16. A. Choukourov, I. Melnichuk, I. Gordeev, D. Nikitin, R. Tafiichuk, **P. Pleskunov**, J. Hanuš, J. Houška, T. Kretková, M. Dopita. Self-organization of vapor-deposited polyolefins at the solid/vacuum interface. *Progress in Organic Coatings*, vol. 143, pp. 105630, 2020.
17. M. Vaidulych, **P. Pleskunov**, J. Kratochvíl, H. Mašková, P. Kočová, D. Nikitin, J Hanuš, O. Kylián, J. Štěrba, H. Biederman, A. Choukourov. Convex vs concave surface nano-curvature of Ta_2O_5 thin films for tailoring the osteoblast adhesion. *Surface & Coatings Technology*, vol. 393, pp. 125805, 2020.

List of conference contributions presented by author

1. **P. Pleskunov**, D. Nikitin, A. Choukourov, D. Shutov, P. Bogdanov, V. Rybkin, H. Biederman, "The destruction kinetics of organic dyes in aqueous solutions under the treatment by low-temperature plasma jet," International Conference on Plasmas with Liquids, Prague, Czech Republic, 5.03.2017 – 9.03.2017, *poster*.
2. **P. Pleskunov**, A. Choukourov, D. Nikitin, A. Shelemin, M. Vaidulych, J. Hanuš, I. Khalakhan, O. Kylián, D. Slavínská, and H. Biederman, "Gas-phase Synthesis of Plasma Polymer Nanoparticles with Controlled Properties," 26th Annual Conference of Doctoral Students – WDS 2017, Prague, Czech Republic, 6.06.2017 – 8.06.2017, *oral presentation*.
3. **P. Pleskunov**, A. Choukourov, D. Nikitin, J. Hanuš, A. Shelemin, I. Khalakhan, D. Slavínská, H. Biederman, "Nitrogen-containing plasma polymer nanoparticles with controlled size and chemical composition," 21th International Colloquium on Plasma processes, Nice, France, 26.06.2017 – 30.06.2017, *poster*.
4. **P. Pleskunov**, A. Choukourov, D. Nikitin, A. Shelemin, J. Hanuš, O. Kylián, I. Khalakhan, I. Gordeev, D. Slavínská and H. Biederman, "Fabrication of Plasma Polymerized Acrylic Acid Nanoparticles Exploiting a Gas Aggregation Cluster Source," 8th International Workshop on Polymer Metal Nanocomposites, Prague, Czech Republic, 12.09.2017 – 15.09.2017, *poster*.

5. **P. Pleskunov**, D. Nikitin, A. Shelemin, J. Hanuš, I. Khalakhan, A. Choukourov, "Preparation of functionalized nanoparticles with tunable properties by plasma polymerization of acrylic acid," Czech – German Workshop on Nanomaterials, České-Budějovice, Czech Republic, 10.05.2018 – 11.05.2018, *oral presentation*.
6. O. Kylián, D. Nikitin, **P. Pleskunov**, A. Shelemin, A. Kuzminova, J. Kratochvil, A. Choukourov, "Antibacterial composites of Cu nanoparticles embedded into plasma polymer matrix," 17th Joint Vacuum Conference, Olomouc, Czech Republic, 10.09.2018 – 14.09.2018, *oral presentation*.
7. **P. Pleskunov**, D. Nikitin, R. Tafiichuk, A. Shelemin, J. Hanuš, I. Khalakhan, A. Choukourov, "Pulsed Plasma Polymerization of Acrylic Acid for the Synthesis of Carboxyl-Functionalized Nanoparticles," 16th International Conference on Plasma Surface Engineering, Garmisch-Partenkirchen, Germany, 17.09.2018 – 21.09.2018, *poster*.
8. **P. Pleskunov**, A. Shelemin, D. Nikitin, Hanuš, J. Kousal, I. Khalakhan, P. Kuš, A. Choukourov, "Synthesis of COOH-functionalized plasma polymer nanoparticles," 24th International Symposium on Plasma Chemistry, Naples, Italy, 9.06.2019 – 14.06.2019, *oral presentation*.
9. **P. Pleskunov**, T. Kretková, M. Thomsen, A. Shelemin, J. Hanuš, J. Kousal, P. Kuš, M. Dopita, A. Choukourov, H. Biederman, "Synthesis of niobium nanoparticles by gas aggregation as building blocks for mesoporous coatings," 9th International Workshop on Polymer Metal Nanocomposites, Aalto, Finland, 22.08.2019 – 24.08.2019, *oral presentation*.

Author’s contribution

The author constructed the experimental setup for the production of ppAA NPs, ppPE and ppPEO thin films as well as all the plasma polymer composite materials. The author carried out the deposition of ppAA NPs, ppPE, ppPEO and composites thereof and/or characterized them by SEM, AFM, XPS, FTIR and ellipsometry. Additionally, the author conducted the protein adsorption measurements and assisted in FC-AFM, GPC and zeta-potential measurements. The author also performed processing, evaluation, formal analysis and interpretation of the results; conceptualization and composition of the manuscripts.